UNIVERSIDAD DE CHILE
FACULTAD DE CIENCIAS FÍSICAS Y MATEMÁTICAS
DEPARTAMENTO DE FÍSICA

# TWO STUDIES ON THE INTERPLAY BETWEEN TOPOLOGICAL PHASES, ROBUST EDGE STATES AND BOSONIC EXCITATIONS

TESIS PARA OPTAR AL GRADO DE
MAGÍSTER EN CIENCIAS, MENCIÓN FÍSICA

**JOAQUÍN MEDINA DUEÑAS**

PROFESORES GUÍA:
LUIS E. F. FOA TORRES
CARLA HERMANN AVIGLIANO

MIEMBROS DE LA COMISIÓN:
PABLO SOLANO
TATIANA G. RAPPOPORT

Este trabajo ha sido parcialmente financiado por : Agencia Nacional de Investigación y Desarrollo (ANID), beca CONICYT/PFCHA/MagísterNacional/2019-22200526.

SANTIAGO DE CHILE
2021

RESUMEN DE LA TESIS PARA OPTAR AL GRADO DE MAGÍSTER EN CIENCIAS, MENCIÓN FÍSICA
POR: Joaquín Eduardo Medina Dueñas
FECHA: 2021
PROF. GUÍA: Luis E. F. Foa Torres
Carla Hermann Avigliano

# TWO STUDIES ON THE INTERPLAY BETWEEN TOPOLOGICAL PHASES, ROBUST EDGE STATES AND BOSONIC EXCITATIONS

This thesis consists of two parts. In part I, we study the role of topology in the propagation of quantum light within a photonic lattice with non trivial topological order. We focus on the behavior of squeezed states of light propagating in a one-dimensional waveguide array realizing the topological Su-Schrieffer-Heeger model, employing analytic and numerical methods. Specifically, we study photon statistics, one-mode and two-mode squeezing and entanglement generation when the topologically protected localized state is excited both with single-mode and two-mode squeezed vacuum states of light, benchmarking our results with those of a topologically trivial localized state. We find that propagation of squeezed of squeezed light in a topologically protected state robustly preserves the phase of the squeezed quadrature as the system evolves, and show how this topological protection can be harnessed for quantum information protocols.

In part II, we study the electronic properties of a two-dimensional material under the effects of electron-phonon interaction with chiral phonons, which break time reversal symmetry. We consider a honeycomb lattice and include coupling between electrons and lattice vibrations employing a non perturbative Fock space solution. Electron-phonon interactions cause indirect transitions with momentum transfer between the excitations, generating a valley-selective indirect band gap, which in turn is sensitive to the chirality of the phonon mode. For a zigzag ribbon geometry, copropagating edge states which bridge the valley selective gap coexist with a continuum of bulk states of the ungapped valleys. The copropagating edge states are found to be robust against moderate amounts of disorder. Our results constitute a first step in the understanding of electron-chiral phonon interactions and their hybrid electron-phonon states of matter.

# Agradecimientos

Agradezco a todas las personas que me han acompañado en este proceso. La lista puede ser muy larga para estas páginas, muy latera para leerla, y además me da miedo dejar a alguien fuera por descuido. Sin embargo, debo mencionar el apoyo de mi familia, que a pesar de verme dibujando jeroglíficos todo el día, siempre me ha apoyado y ayudado en mi crecimiento personal, en mis estudios, y en todas las metas que me propongo la verdad. A mi familia, amigxs, pareja, compañerxs, todas las personas que trabajaron conmigo en esta tesis: Muchas gracias por el apoyo y por enseñarme tanto.

# Contents

# Introduction

This thesis covers a variety of topics from solid state physics to quantum optics; studying electrons, photons and phonons; in one and two dimensions. It is composed by two parts. The first one focuses on elucidating the interplay between symmetry protected topological phases and quantum properties of light. This is done by studying the propagation of squeezed light in a one-dimensional topological photonic lattice. The second part studies the electronic properties of a two-dimensional honeycomb lattice with time-reversal symmetry (TRS) broken due to coupling with mechanical degrees of freedom, in particular chiral phonons.

Starting from topological materials, this work was fueled by curiosity, attempting to relate areas of physics that at first may seem disconnected, and opening new questions regarding the behavior of topological systems. The study of topological phases of matter originates in solid state physics with the discovery of the integer quantum Hall effect (IQHE) [1, 2], where a two-dimensional electron gas in the presence of a strong perpendicular magnetic field exhibits a perfectly quantized Hall conductivity carried entirely by chiral states located at the boundaries of the system [3, 4]. Quantization at a microscopic scale has been a central element of physics since the first developments of quantum theory. However, the IQHE presents quantization of a macroscopic quantity in a many body system, which in turn is insensitive (up to a threshold) to the geometry, purity and other macroscopic properties of the sample, constituting a new quantum phase. It was later shown that this new phenomenology is explained by studying the topological properties of the space spanned by the electron wave functions (or by studying the equivalence classes of the hamiltonian), which might be protected by the symmetries of the system [5–8]. The topological phase of the IQHE, and its boundary states, are the most robust one can have as they do not require any preserved symmetry. Topological systems have been extensively studied since, finding topological phases in all kinds of systems; protected by broken [9–12] or preserved [13–16] TRS or by crystal symmetries [17–19]; in one [20, 21], two [9, 13, 22, 23] and three [15, 24, 25] dimensions; among many others [26–28]. Furthermore, topological physics was found to be fundamental to wave phenomena within periodic media, allowing for an extension of these ideas to photonics [29–31], spintronics [32], mechanical systems [33], circuits [34], and others [35, 36].

**Part I** of this thesis is positioned in the context of topological phases in photonic systems. Our approach is not limited to studying known topological systems from an optical framework, but we take a leap forward by considering quantum properties of light and their response to the lattices topology, searching for topological protection of quantum features. Photonic systems are positioned as a promising platform for scalable room-temperature quantum information

processing; however, quantum information remains sensitive to noise sources, losses, and other fabrication imperfections of devices [37–39]. Recently, quantum topological photonics —namely the study of quantum light in topological photonic lattices— has emerged as an alternative for protecting quantum information encoded within the electromagnetic field [40–42]. Quantum information may be described in terms of discrete or continuous variables; each of these frameworks presenting their own implementations and advantages, both from a theoretical and an experimental point of view [43–47]. Research on quantum topological photonics has been mainly directed to the behavior of Fock-like states, which constitute a discrete variable description of the field, where promising experimental results show topological protection of quantum correlations and entanglement [40–42, 48–50]. The behavior of continuous variable quantum states on the other hand, remains an open question. Our approach on this topic stems from the latter perspective, where squeezed states are of particular interest as they constitute a fundamental source for continuous variable entanglement [44]. We investigate [51] on the propagation of squeezed light in a waveguide array realizing the topological Su-Schrieffer-Heeger (SSH) model [52–54], elucidating the role of topology in the evolution and preservation of quantum features. Furthermore, we show how topological protection of squeezing can be harnessed for quantum information protocols.

Inspired by the IQHE and other broken TRS topological phases [9, 55–57], in **part II** we study [58] the behavior of a two-dimensional lattice when breaking TRS due to electron-phonon interactions with chiral phonons. Interactions between electronic and mechanical degrees of freedom have been extensively studied in solid state physics, playing a crucial role in the development of conducting polymers [20] and the theory of superconductivity [59–61], for example. Electron-phonon interactions have also been found to generate topological effects [52, 62–64]. Robust edge states induced by a linear phonon mode have been found in graphene nanoribbons [62], while a phonon driven Floquet topological insulator is obtained when considering TRS breaking phonons with zero momentum, generated by a linear superposition of degenerate, non chiral phonon modes [63]. Recently, the emergence of chiral phonons —that is, phonons with intrinsic chirality— at high-symmetry momenta in two-dimensional systems was predicted [65], and later observed in tungstene diselenide [66], bringing new ingredients to the table of electron-phonon physics [67–71]. We investigate on the effects of electron-phonon interactions in a honeycomb lattice when considering TRS breaking chiral phonons with non zero momentum. We find that the electron-phonon interactions induce a valley selective gap bridged by copropagating edge states, which coexist with a continuum of bulk states of the non gapped valleys. We perform quantum transport simulations, which exhibit non reciprocal behavior and show the robustness of the edge states.

# Part I

# Topological protection of squeezed light

What is the role of topology in the propagation of quantum light in photonic lattices? We address this question by studying the propagation of squeezed states in a topological one-dimensional waveguide array. We benchmark our results with those for a topologically trivial localized state and study their robustness against disorder in order to isolate the role of topology. Specifically, we study photon statistics, one-mode and two-mode squeezing, and entanglement generation when the topological state is excited with squeezed light. These quantum properties inherit the shape of the localized state, and thus follow its fate when disorder is introduced. But more interestingly, and unlike in the topologically trivial case, we find that propagation of squeezed light in a topologically protected state robustly preserves the phase of the squeezed quadrature as the system evolves. We show how this latter topological advantage can be harnessed for quantum information protocols, in particular, quantum teleportation.

This topic stands at the interface between topological systems and quantum optics, while also involving concepts of photonic lattices and quantum information. We intend to extend this investigation to the widest possible spectrum of the physics community. For this reason, we begin providing a broad overview on the two main areas involved, topological systems and quantum optics. Chapter 1 introduces topological band theory and symmetry protected topological phases. These concepts are developed while reviewing in detail the SSH model from a solid state physics perspective. We then explicitly adapt the framework of topological systems to photonics. In chapter 2 we develop the framework of quantum optics, focusing on the continuous variable description of the quantized electromagnetic field. We discuss in detail the emergence of quantum correlations and entanglement in squeezed states. Chapter 3 contains the bulk of the carried research, contained in reference [51]. We employ the concepts developed previously to study the interplay between topology and quantum correlations by means of the propagation of squeezed light in an SSH waveguide array.

# Chapter 1

# Topological band theory

During the XX$^{\text{th}}$ century quantum mechanics revolutionized our understanding of nature, describing elementary particles such as electrons by wave-like behavior. Under this new paradigm, band theory successfully described and predicted the electric properties of solids, labelling them as conductors or insulators according to the location of the Fermi level in their band structure. However, since the discovery of the Integer Quantum Hall Effect (IQHE) [2] in 1980, it was shown that the energy spectrum does not suffice to fully describe the behavior of electrons, but the topology of the space spanned by the electron wave functions must be considered as well [5], thus setting the kickoff for topological band theory.

The purpose of this chapter is to introduce topological band theory and symmetry protected topological phases, not only from a solid state physics framework, but porting the theory to photonic systems as well. We begin by briefly discussing the IQHE in section 1.1. In section 1.2 we develop topological band theory from an electronic approach while reviewing in detail the Su-Schrieffer-Heeger (SSH) system. We characterize its topological order in terms of a topological invariant, analyzing its connection to the symmetries of the system, and show the emergence of topologically protected boundary states which are robust against symmetry-preserving disorder. In section 1.3 we port topological band theory to photonic lattices. We begin by building a correspondence between photonic and solid state systems. We then explicitly adapt concepts of topological band theory to photonic systems, and discuss the manifestations of topology in an optic setup.

## 1.1 The integer quantum Hall effect

Our journey towards topological physics will have the same starting point as it did historically, the IQHE [2]. Realized in 1980 by von Klitzing, Dorda and Pepper, in the IQHE a two-dimensional electron gas is placed under a strong perpendicular magnetic field ($\sim 15\,T$) at low temperature ($\sim 1.5\,K$). This system presents a zero longitudinal conductivity, but a non-zero Hall conductivity quantized by $\sigma_{xy} = \nu\frac{e^2}{h}$ with $\nu \in \mathbb{Z}$ [1]. There are several remarkable aspects of this phenomenon [3, 4]: (i) The Hall conductivity depends only on fundamental constants and $\nu$, which has been measured to be an integer with precision of one part in a billion [72].

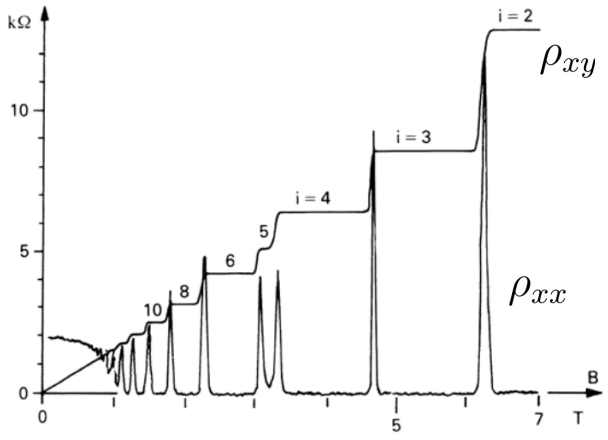


FIGURE 1.1: Longitudinal resistivity $\rho_{xx}$ and Hall resistivity $\rho_{xy}$ as a function of the magnetic field in the IQHE. Hall resistivity takes quantized values $\rho_{xy} = \frac{h}{\nu e^2}$, exhibiting plateaus as a function of the magnetic field. Longitudinal resistivity is in general zero, with peaks when the Fermi energy crosses a Landau level, and the Hall resistivity changes value.

This quantized behavior is clearly observed in Fig. 1.1, where Hall conductivity behaves as a series of plateaus when increasing the magnetic field, or equivalently, lowering the filling factor. (ii) The Hall conductivity is entirely carried by chiral edge states, that is states with antiparallel velocity exponentially localized at opposite boundaries of the sample. (iii) The Hall current is disipationless. (iv) Quantization of the Hall conductivity is a robust, universal phenomenon. It is independent of the composition, purity, geometry, and other macroscopic properties of the sample. The IQHE presents a macroscopic manifestation of quantum phenomena, robust to the details of the sample, thus it must be characterised by some quantum phase. Furthermore, the system presents a non-conducting bulk, with chiral electric current exclusively localized at the boundaries of the system, challenging the established classification of metals and insulators. As proved by Thouless, Kohmoto, Nightingale and den Nijs, the explanation of this phenomenon is a matter of topology [5].

Before diving into topology, lets look at the IQHE from a band theory point of view. Even though the electron gas is not a crystal, the system does present discrete translational invariance characterized by a magnetic unit cell [4]. As is known, the spectrum of a two-dimensional electron gas in the presence of a magnetic field takes the form of discrete, non-dispersive Landau levels, which we will consider as energy bands. Standard band theory dictates that if the Fermi energy lies in between Landau levels, then the system behaves as an insulator, which is clearly not the case due to the conducting edge states. However, the essence of the IQHE lies in the presence of an external magnetic field which breaks TRS, not in the specific geometry or other local properties at the edges of the sample [13]. Thus, the translationally invariant system must determine the quantization of the Hall conductivity and emergence of chiral edge states. Indeed, the procedure is as follows [3–5, 73]:

Let $|u_n(\mathbf{k})\rangle$ be the bloch wave function of the $n$-th band of the system, at a given $\mathbf{k}$-point defined in the magnetic Brillouin zone. The Berry phase acquired by the state when transported along

a path $\mathcal{C}$ in $\mathbf{k}$-space, $\gamma_n(\mathcal{C})$, is is the integral of the Berry connection $\mathcal{A}_n(\mathbf{k})$ along said path

$$\gamma_n(\mathcal{C}) = \int_{\mathcal{C}} \mathcal{A}_n(\mathbf{k}) \mathrm{d}\mathbf{k} \ , \tag{1.1}$$

with $\mathcal{A}_n(\mathbf{k}) = \mathrm{i}\langle u_n(\mathbf{k})|\nabla_{\mathbf{k}}|u_n(\mathbf{k})\rangle$, and $\nabla_{\mathbf{k}}$ the nabla operator in $\mathbf{k}$-space. The Chern number of the $n$-th band, $c_n$, is defined as the Berry phase acquired by the wave function $|u_n(\mathbf{k})\rangle$ when transported around the entire Brillouin zone, divided in $2\pi$,

$$c_n = \frac{1}{2\pi} \int_{\partial \mathrm{BZ}} \mathcal{A}_n(\mathbf{k}) \mathrm{d}\mathbf{k} \ . \tag{1.2}$$

Notice that the Berry connection is not gauge independent, as a gauge transformation $|u_n(\mathbf{k})\rangle \to \mathrm{e}^{\mathrm{i}\alpha(\mathbf{k})}|u_n(\mathbf{k})\rangle$ changes the Berry connection by $\mathcal{A}_n(\mathbf{k}) \to \mathcal{A}_n(\mathbf{k}) - \nabla_{\mathbf{k}}\alpha(\mathbf{k})$. Reminiscent of the electromagnetic vector potential we define the gauge independent Berry flux, $\mathcal{F}_n(\mathbf{k}) = \nabla_{\mathbf{k}} \times \mathcal{A}_n(\mathbf{k})$. By means of Stokes' theorem, the Chern number of the $n$-th band may now be calculated as the total Berry flux through the Brillouin zone

$$c_n = \frac{1}{2\pi} \int_{\mathrm{BZ}} \mathcal{F}_n(\mathbf{k}) \mathrm{d}^2 k \ , \tag{1.3}$$

which only takes integer values, in correspondence to the quantization of the Dirac monopole [6, 74]. Finally, computing the Hall conductivity using the Kubo formula, the integer $\nu$ is equal to the sum of the Chern number of all occupied bands,

$$\nu = \sum_n c_n \ . \tag{1.4}$$

This quantity —known as the TKNN invariant or Chern number— maintains its value provided there exists a finite energy gap separating all occupied and unoccupied states [6].

Now enters topology: As a branch of mathematics, topology describes the fundamental properties of spaces by sets of topological invariants, that is, quantities that are invariant to *smooth* transformations —mathematically, homeomorphisms— applied to such spaces [75]. If two spaces have the same topological invariants they can be *smoothly* transformed into one another, thus defining topological equivalence. The equivalence ceases if there is no *smooth* transformation connecting the spaces.

We have shown that in the IQHE the Hall conductivity is entirely determined by the integer $\nu$, which can only change its value when the Fermi energy lies within a band. Thus, we consider the TKNN invariant $\nu$ to be a topological invariant of the system, which characterizes the integer quantum Hall phase in terms of the topology of the space spanned by the electron wave functions. Now imagine that we adiabatically change the parameters of the system, continuously deforming the band structure. If such a deformation does not remove the Fermi energy from the current energy gap, or closes it, the system will remain in the same topological phase, defining a *smooth* transformation from a topological band theory perspective[1]. Finally, lets recall that the Hall

[1]We have introduced topological band theory focusing only in gapped topological phases. Indeed, topological phases can emerge in systems with a gapless bulk spectra, such as Weyl semimetals [25], nodal line semimetals [76], among others [29, 77]. In this scenario some concepts discussed during this chapter must be revised. We recommend references [76–78] for further information on gapless topological phases.

conductivity is carried entirely by edge states of the electron gas, whereas the TKNN invariant is defined in terms of Bloch wave functions which can only be defined in a translationally invariant system. This is our first encounter with the bulk-boundary correspondence [79]: A non-trivial topological phase which can only be defined in an infinite system, determines the emergence of edge states which manifest in a finite system.

Many more topological phases were later proposed and realized [6, 7]. It is not in the purpose of this thesis to review the full variety of known topological phases, but for completeness sake we briefly mention three important breakthroughs in the field. In 1988 Haldane [9] proposed a honeycomb lattice model exhibiting a Chern insulator phase with no need for an external macroscopic magnetic field. Instead, TRS is broken by an artificial magnetic field with the full symmetry of the lattice so zero magnetic flux crosses a unit cell. Even though an experimental realization of this system remained ellusive for decades [10], it introduced the concept of a lattice with topological order. In 2005 Kane & Mele [22] proposed a spin-full honeycomb model consisting of two conjugate copies of Haldane's spin-less model, one for each spin state, globally preserving TRS and attributing the artificial magnetic field to spin-orbit coupling. This system —known as quantum spin Hall insulator— exhibits helical edge states, that is, two sets of chiral states with opposite chirality for each spin [80]. Their work introduces the first time-reversal invariant lattice exhibiting a non-trivial topological phase, and provides a theoretical basis on which a crystal may exhibit a spin polarized quantum Hall response. The last breakthrough which we will mention is the theoretical prediction and experimental realization of the quantum spin Hall insulator in HgCdTe quantum wells, predicted by Bernevig, Hughes and Zhang in 2006 [23], and observed by König, *et. al.* in 2007 [81].

## 1.2 The SSH system

This section will review in detail concepts of topological band theory employing a system that is of particular interest to this thesis, the Su-Schrieffer-Heeger model for polyacetylene, or simply the SSH system [52, 53]. We will characterize the topological phase of the lattice in terms of the Zak phase, and show how it is protected by chiral symmetry. We will also study the emergence of topologically protected boundary states, and their robustness against disorder in the lattice.

The SSH model was originally proposed to describe the electric properties of polyacetylene, a quasi-one-dimensional chain of CH (Carbon-Hydrogen) units, as depicted in Fig. 1.2-(a). The chain presents a dimerization, with staggered C-C bond lengths due to the Peierls transition, where a pair of neighboring CH units move towards each other rendering an overall energetically favorable configuration considering electronic and mechanical degrees of freedom [82]. Upon exchanging the long and short bonds the system would clearly remain in a minimal energy configuration, thus the SSH model presents two degenerate ground states, which are at the heart of its topological ordering, as we will show during this section. The spontaneous dimerization can be incorporated into a tight-binding model by introducing electron-phonon coupling terms [20, 53]; however, we will only consider a lattice with an externally given dimerization.

Under a tight binding approximation for low energy excitations, where only the C-C $\pi$ bonds are represented, the model consists of a one-dimensional chain of identical modes with staggered hopping amplitudes, forming a unit cell of two sites, even and odd, as shown in Fig. 1.2-(b).

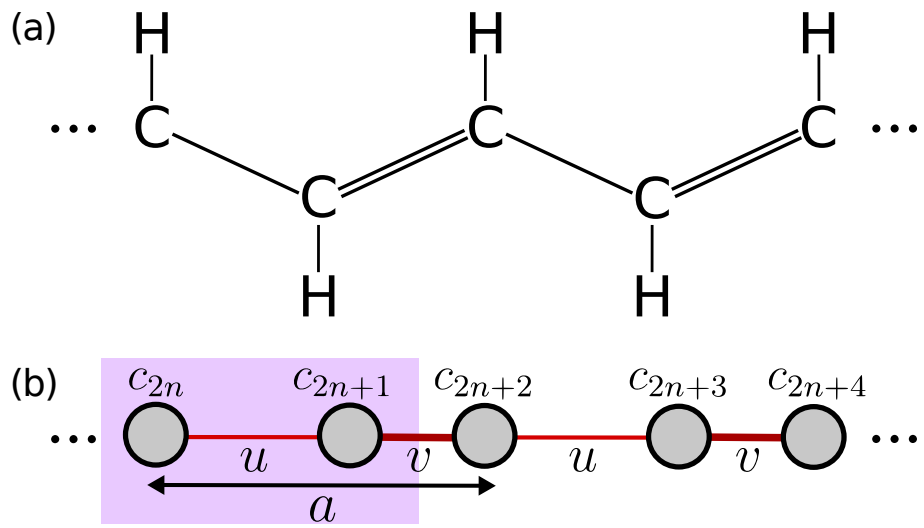


FIGURE 1.2: **(a)** Chemical scheme of polyacetylene. **(b)** Scheme of the tight binding SSH model. Sites are represented by grey circles and hoppings by red lines. The unit cell is highlighted in purple, and the lattice periodicity constant $a$ is shown over the lattice.

The hamiltonian is given by

$$\hat{H}_{\text{SSH}} = \sum_n \left[\varepsilon_{\text{even}} c_{2n}^\dagger c_{2n} + \varepsilon_{\text{odd}} c_{2n+1}^\dagger c_{2n+1}\right] + \left[u c_{2n}^\dagger c_{2n+1} + v c_{2n+1}^\dagger c_{2n+2} + \text{h.c.}\right] \tag{1.5}$$

with $c_{2n}$ ($c_{2n+1}$) the electronic annihilation operator of the even (odd) site at the $n$-th unit cell, $\varepsilon_{\text{even}}$ ($\varepsilon_{\text{odd}}$) the onsite energy of the even (odd) sublattice, $u$ and $v$ the intra- and inter-cell hoppings, and the sum is carried over all unit cells. For simplicity we will consider $u$ and $v$ of the same sign. As the two CH units per unit cell are identical $\varepsilon_{\text{even}} = \varepsilon_{\text{odd}} = \varepsilon$, and the first term in Eq. (1.5) is constant for all sites, allowing us to omit the onsite terms as they only represent a shift $\varepsilon$ in the spectrum.

For a periodic system we introduce the Fourier transforms

$$c_{2n} = \int_{-\pi/a}^{\pi/a} \mathrm{e}^{\mathrm{i}kan} c_{\text{even}}(k)\mathrm{d}k \tag{1.6a}$$

$$c_{2n+1} = \int_{-\pi/a}^{\pi/a} \mathrm{e}^{\mathrm{i}kan} c_{\text{odd}}(k)\mathrm{d}k \ , \tag{1.6b}$$

obtaining the hamiltonian

$$\hat{H}_{\text{SSH}} = \int_{-\pi/a}^{\pi/a} \psi_k^\dagger \mathcal{H}_{\text{SSH}}(k)\psi_k \mathrm{d}k \ , \tag{1.7}$$

with $\psi_k = (c_{\text{even}}(k), c_{\text{odd}}(k))^{\text{t}}$, and

$$\mathcal{H}_{\text{SSH}}(k) = \begin{pmatrix} 0 & u + v\mathrm{e}^{-\mathrm{i}ka} \\ u + v\mathrm{e}^{\mathrm{i}ka} & 0 \end{pmatrix} \ . \tag{1.8}$$

Defining $f(k) = u + v\mathrm{e}^{-\mathrm{i}ka} = |f(k)|\mathrm{e}^{\mathrm{i}\theta(k)}$, the eigenvalues $E_\pm(k)$ and eigenstates $|u_\pm(k)\rangle$ of the system are given respectively by

$$E_\pm(k) = \pm|f(k)| = \pm\sqrt{u^2 + v^2 + 2uv\cos(ka)} \ , \tag{1.9a}$$

$$|u_{\pm}(k)\rangle = \frac{1}{\sqrt{2}} \begin{pmatrix} \pm e^{i\theta(k)} \\ 1 \end{pmatrix} . \tag{1.9b}$$

It is evident from Eq. (1.9a) that the spectrum is gapped except for the case $|u| = |v|$, where the gap closes at the borders of the Brillouin zone. Furthermore, the spectrum is invariant when exchanging the values of $u$ and $v$, in accordance to the degeneracy of the ground state which stems from the Peierls transition, as Fig. 1.3 shows. This is only logical when considering an infinite lattice, as it cannot make a difference whether we take the unit cell to be composed of sites $c_{2n}$ and $c_{2n+1}$, or sites $c_{2n-1}$ and $c_{2n}$.

Interestingly, the eigenmodes are not invariant under the $u \leftrightarrow v$ exchange. A *smooth* transformation cannot be defined in order to exchange the hopping values as the gap must close at some point where $|u| = |v|$, hinting for a topological transition. In the general case, all systems with $|u| > |v|$ can be continuously transformed into one another without closing the gap, and so is the case for the $|u| < |v|$ systems, but in order to transform from the former to the latter (or vice versa), the gap must be closed at $|u| = |v|$.

At this point there might be some confusion. We have claimed that in an infinite system the exchange $u \leftrightarrow v$ merely accounts for our choice on how to build a unit cell. Nevertheless, we are anticipating that these two systems are topologically inequivalent, so how can this occur? Topological phases are determined by the eigenstates of a system, therefore even though the bands of a lattice with hoppings $u$ and $v$ are identical to those of the exchanged one, they are characterized by a different topological invariant.

Before we define a topological invariant and determine its possible values, lets study the eigenvalues and eigenmodes of a finite sample, aiming to observe any possible edge states. We choose the unit cell to be composed by sites $c_{2n}$ and $c_{2n+1}$, therefore the first and last hoppings of a pristine finite lattice must be $u$. In Fig. 1.4-(a) we show the spectrum of a finite lattice as a function of the hopping amplitudes. For $|u| < |v|$ a pair of degenerate states with zero eigenvalue appear, localized at the edges of the lattice as shown in Fig. 1.4-(b).

The topology of a one-dimensional lattice is characterized by the Zak phase, which corresponds

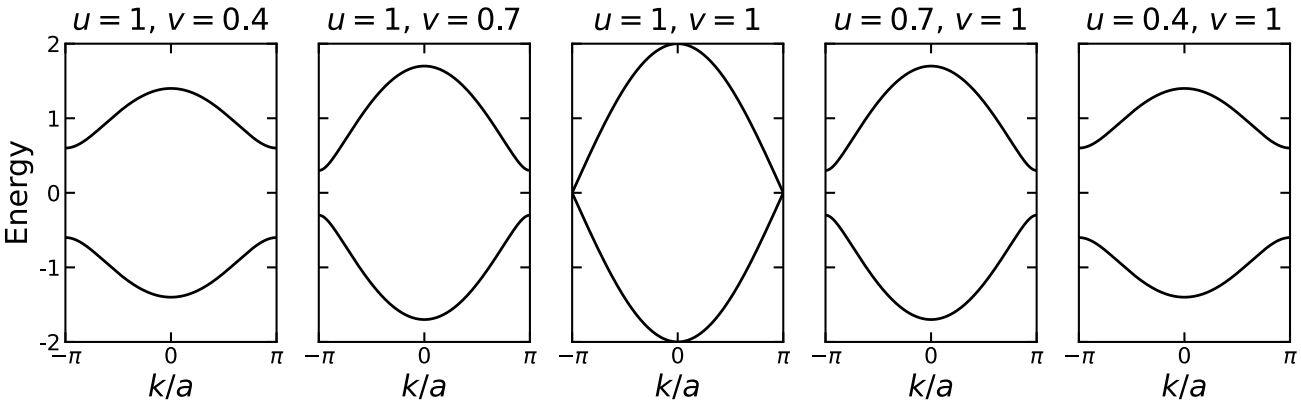


FIGURE 1.3: Energy bands of the SSH system. The hopping values $u$ and $v$ used are indicated on top of each plot. The spectrum is invariant when interchanging $u$ and $v$, and the gap only closes for $|u| = |v|$.

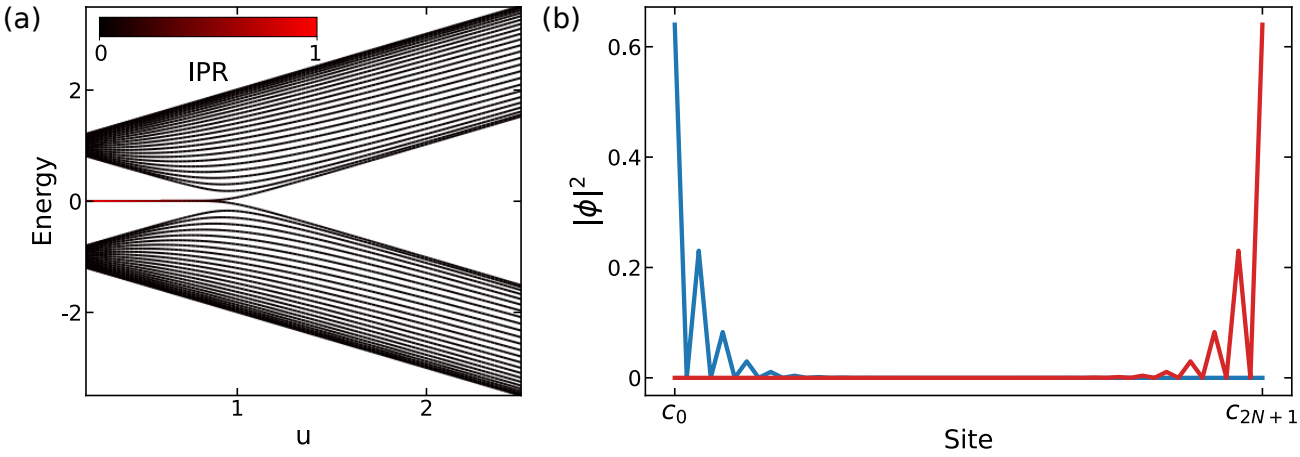


FIGURE 1.4: **(a)** Eigenvalues of a finite SSH lattice (25 unit cells) as a function of $u$, at fixed $v = 1$. Two degenerate edge states with zero energy exist when $|u| < |v|$. The color scale indicates the localization of each state measured by the inverse participation ratio (IPR). For a state given by $\phi = \sum_n \alpha_n c_n$, with $\alpha_n$ scalar coefficients, the IPR is given by $\text{IPR} = \sum_n |\alpha_n|^4$. It is equal to 1 (0) for a fully localized (extended) state. **(b)** Weight of the edge states on each lattice site, for $u = 0.6$ and $v = 1$. Each state is plotted in a different color.

to the Berry phase acquired when transporting an eigenmode across the entire one-dimensional Brillouin zone [83, 84]. The Zak phase of each band is given by

$$\mathcal{Z}_\mu = \mathrm{i} \int_{-\pi/a}^{\pi/a} \langle u_\mu(k)| \, \partial_k \, |u_\mu(k)\rangle \, \mathrm{d}k \ , \tag{1.10}$$

with $\mu = \pm$. Notice that this is a gauge dependent quantity, as for a gauge transformation $|u(k)\rangle \to \mathrm{e}^{\mathrm{i}\alpha(k)} \, |u(k)\rangle$ its value is modified by

$$\begin{aligned} \mathcal{Z} &\to \mathcal{Z} - \int_{-\pi/a}^{\pi/a} \partial_k \alpha(k) \mathrm{d}k \\ &= \mathcal{Z} - 2\pi m \ , \end{aligned} \tag{1.11}$$

with $m \in \mathbb{Z}$, and the second line is obtained due to the periodicity of $k$-space. Therefore the Zak phase can only be defined as a gauge invariant quantity modulo $2\pi$.

Using the eigenmodes in Eq. (1.9b) we obtain an identical Zak phase for both bands

$$\mathcal{Z} = -\frac{1}{2} \int_{-\pi/a}^{\pi/a} \partial_k \theta(k) \mathrm{d}k \ , \tag{1.12}$$

which corresponds to the winding number of the complex function $f(k)$ over the entire Brilluoin zone, times $-\pi$. As the phase $\theta(k)$ is a multivalued function we introduce a branch cut in the negative real axis, thus when $\theta(k)$ crosses it in anticlockwise (clockwise) direction, the winding number increases (decreases) in 1. Mathematically, $\theta(k)$ crosses the branch cut when the conditions

$$\mathrm{Im}(f) = -v \sin(ka) = 0 \qquad \wedge \qquad \mathrm{Re}(f) = u + v \cos(ka) < 0 \tag{1.13}$$

are fulfilled simultaneously. The first condition is only satisfied for $ka = 0$ , and $ka = \pi$, thus the second condition reads $u \pm v < 0$. If $|u| > |v|$, then both $u + v$ and $u - v$ have the same sign, thus the branch cut is crossed twice or not crossed at all, resulting in a trivial Zak phase. On the other hand, if $|u| < |v|$, then both alternatives $u \pm v$ have opposite signs, meaning that the branch cut is crossed only once, yielding a non trivial Zak phase of $\pi$ which reveals the topological character of the edge states. Finally, in the singular case $|u| = |v|$, $f(k)$ passes through the origin of the complex plane, thus the topological invariant is ill-defined as it suffers a transition.

### 1.2.1 The role of symmetries

Up to this point we have introduced the concept of symmetry protected topological phases which are classified according to topological invariants. However, the role of symmetries has not been fully exploited yet. We will now clarify, by means of the SSH system, the connection between the topological phases and the symmetries of the system.

Consider the SSH model with different onsite terms for each sublattice, which corresponds to the Rice-Mele model [85]. We define $\varepsilon = (\varepsilon_{\text{even}} + \varepsilon_{\text{odd}})/2$ and $\Delta = (\varepsilon_{\text{even}} - \varepsilon_{\text{odd}})/2$. The term $\varepsilon$ represents a shift in the spectrum, and only $\Delta$ is relevant to the band structure and eigenmodes. The real space hamiltonian is given by

$$\hat{H}_{\text{RM}} = \sum_n \Delta \left[ c_{2n}^\dagger c_{2n} - c_{2n+1}^\dagger c_{2n+1} \right] + \left[ u c_{2n}^\dagger c_{2n+1} + v c_{2n+1}^\dagger c_{2n+2} + \text{h.c.} \right] \ , \tag{1.14}$$

while the hamiltonian in reciprocal space is

$$\begin{aligned} \mathcal{H}_{\text{RM}} &= \begin{pmatrix} \Delta & u + v\mathrm{e}^{-\mathrm{i}ka} \\ u + v\mathrm{e}^{\mathrm{i}ka} & -\Delta \end{pmatrix} \\ &= \vec{h} \cdot \vec{\sigma} \ , \end{aligned} \tag{1.15}$$

where we defined $\vec{h} = (u + v\cos(ka), v\sin(ka), \Delta)^{\mathrm{t}}$, and $\vec{\sigma} = (\sigma_x, \sigma_y, \sigma_z)^{\mathrm{t}}$ the vector containing the Pauli matrices, which act on the sublattice degree of freedom.

The eigenvalues are $E_\pm = \pm|\vec{h}| = \pm\sqrt{\Delta^2 + u^2 + v^2 + 2uv\cos(ka)}$, and the gap is only closed for $\Delta = 0$ and $|u| = |v|$ simultaneously. The spectrum remains invariant under a $u \leftrightarrow v$ exchange, but these systems now may be connected without closing the gap, impeding us from defining a topological phase transition.

Clearly the inclusion of different onsite terms in the hamiltonian has broken the topological order of the system. For $\Delta = 0$ the Zak phase is determined by the winding number of the complex function $f(k)$, or equivalently, the winding number of the vector $\vec{h}$ in the $xy$ plane. For $\Delta \neq 0$, $\vec{h}$ is lifted from the $xy$ plane, and its winding number around the origin may not be defined. Therefore all possible systems with parameters $\Delta$, $u$, and $v$ can be *smoothly* connected, and the Zak phase, though it is still defined, ceases to be a topological invariant.

To understand the rupture of topological order we must study the symmetries of the system. An electronic system has a symmetry represented by the operator $\hat{\mathcal{U}}$, if the canonical fermionic

anti-commutation relations, and its hamiltonian are preserved under a transformation by $\hat{\mathcal{U}}$ [8]. These conditions read respectively

$$\hat{\mathcal{U}}\left[c_n, c_m\right]_+ \hat{\mathcal{U}}^{-1} = \left[c_n, c_m\right]_+ = \delta_{n,m} \ , \tag{1.16a}$$

$$\hat{\mathcal{U}}\hat{H}\hat{\mathcal{U}}^{-1} = \hat{H} \ , \tag{1.16b}$$

with $[\cdot,\cdot]_+$ the anticommutator.

The SSH system presents chiral symmetry, which is broken when including a staggered onsite term as in the Rice-Mele model. Chiral symmetry is given by the composition of particle-hole symmetry and TRS; its action on an annihilation operator is given by a linear combination of creation operators (and vice-versa), and it acts by conjugating complex numbers [8]. We define $\Psi = (\dots, \psi_n^{\mathrm{t}}, \psi_{n+1}^{\mathrm{t}}, \dots)^{\mathrm{t}}$ as the vector containing all annihilation operators of the lattice, with $\psi_n = (c_{2n}, c_{2n+1})^{\mathrm{t}}$ the vector containing the annihilation operators within the $n$-th unit cell. Let $\hat{\Gamma}$ be the chiral symmetry operator, and $\Gamma$ its block matrix representation in the $\Psi$ basis. The action of the chiral operator is given by

$$\hat{\Gamma}\Psi_n\hat{\Gamma}^{-1} = \Gamma^*_{n,m}\Psi^\dagger_m \tag{1.17a}$$

$$\hat{\Gamma}\Psi^\dagger_n\hat{\Gamma}^{-1} = \Gamma_{n,m}\Psi_m \tag{1.17b}$$

$$\hat{\Gamma}\mathrm{i}\hat{\Gamma}^{-1} = -\mathrm{i} \ , \tag{1.17c}$$

where we have used Einsteins convention of summation of repeated indexes. We represent the hamiltonian in block matrix form $\hat{H} = \Psi^\dagger_n H_{n,m}\Psi_m$, and using Eq. (1.16a), (1.16b) and (1.17) we find

$$\begin{aligned}
\hat{H} &= \hat{\Gamma}\hat{H}\hat{\Gamma}^{-1} \\
\Psi^\dagger_n H_{n,m}\Psi_m &= \left(\hat{\Gamma}\Psi^\dagger_n\hat{\Gamma}^{-1}\right)\left(\hat{\Gamma}H_{n,m}\hat{\Gamma}^{-1}\right)\left(\hat{\Gamma}\Psi_m\hat{\Gamma}^{-1}\right) \\
&= \Gamma_{n,k}\Psi_k H^*_{n,m}\Gamma^*_{m,l}\Psi^\dagger_l \\
&= \left(\Gamma^\dagger H\Gamma\right)_{l,k}\Psi_k\Psi^\dagger_l \\
&= \left(\Gamma^\dagger H\Gamma\right)_{l,k}\left(\delta_{k,l} - \Psi^\dagger_l\Psi_k\right) \\
&= \mathrm{Tr}H - \Psi^\dagger_l\left(\Gamma^\dagger H\Gamma\right)_{l,k}\Psi_k \ .
\end{aligned} \tag{1.18}$$

Therefore a hamiltonian has chiral symmetry if its matrix representation $H$ satisfies

$$\mathrm{Tr}H = 0 \qquad \wedge \qquad H = -\Gamma^\dagger H\Gamma \ . \tag{1.19}$$

Applying the second condition in Eq. (1.19) twice we conclude $\Gamma^2 = \mathrm{I}$ up to a phase factor, with I the identity matrix. As $\Gamma$ is also unitary we obtain $\Gamma = \Gamma^\dagger$. We now require the chiral operator to be local, meaning that it acts on each unit cell separately [86]. Let $\hat{\gamma_n}$ be the chiral operator which acts only on the $n$-th unit cell, and $\gamma_n$ its matrix representation in the $\psi_n$ basis, we write the chiral operator as a direct sum of the unit cell operators [86], namely

$$\hat{\Gamma} = \bigoplus_n \hat{\gamma}_n \tag{1.20a}$$

$$\Gamma = \bigoplus_n \gamma_n \ . \tag{1.20b}$$

As the system is periodic $\hat{\gamma}_n = \hat{\gamma}\,\forall n$, thus $\Psi_n^\dagger(\Gamma^\dagger H\Gamma)_{n,m}\Psi_m = \Psi_n^\dagger\gamma^\dagger H_{n,m}\gamma\Psi_m$. Using the Fourier transforms in Eq. (1.6) we find the $k$-space form of Eq. (1.19):

$$\mathrm{Tr}\mathcal{H}(k) = 0 \qquad \wedge \qquad \mathcal{H}(k) = -\gamma^\dagger\mathcal{H}(k)\gamma \ . \tag{1.21}$$

The first condition is trivial for two band systems, as any diagonal terms can be expressed as an irrelevant term shifting the spectrum and a term proportional to $\sigma_z$. From the second condition we conclude that in the basis which diagonalizes $\gamma$, $\mathcal{H}(k)$ is off-diagonal [8]. We thus obtain explicitly the matrix form of the chiral operator in the $\psi_k$ basis, given by

$$\gamma = \begin{pmatrix} 1 & 0 \\ 0 & -1 \end{pmatrix} = \sigma_z \ . \tag{1.22}$$

For a generic hamiltonian $\mathcal{H}(k) = \vec{h}(k)\cdot\vec{\sigma}$, the action of the chiral operator is

$$\begin{aligned} \gamma^\dagger\mathcal{H}\gamma &= \gamma(\vec{h}\cdot\vec{\sigma})\gamma \\ &= h_x\sigma_z\sigma_x\sigma_z + h_y\sigma_z\sigma_y\sigma_z + h_z\sigma_z\sigma_z\sigma_z \\ &= -h_x\sigma_x - h_y\sigma_y + h_z\sigma_z \ , \end{aligned} \tag{1.23}$$

revealing that the system has chiral symmetry only if $h_z = 0$, as in the SSH model.

In summary, any one-dimensional lattice presenting chiral symmetry may be topologically classified by its Zak phase. If the symmetry is broken, the Zak phase may still be defined, but it is no longer a topological invariant. We conclude that the topological order in the SSH model is protected by chiral symmetry. However, we must note that the fact that a lattice presents chiral symmetry does not mean that it is topologically non trivial, but rather that it may present a topologically non trivial phase for a range of parameters [8].

### 1.2.2 Edge States and robustness against disorder

The bulk-boundary correspondence predicts the emergence of gapless states localized at the borders of a topologically non-trivial system [6, 79]; thus the existence of edge states, and their characteristics, must be protected by the symmetries of the system. Our first encounter with topological phases was the IQHE, which is a robust phenomenon, meaning that it is insensitive to details of the sample such as purity or geometry. We expect to extend the robustness of topological phenomena to the SSH system as well. We first demonstrate that the characteristics of the SSH edge states are determined by chiral symmetry in a pristine lattice, following [86]. We then study the response of the states against disorder, concluding that that they are robust against symmetry preserving disorder.

We first rewrite the chiral operator as the difference of the projectors on each sublattice,

$$\begin{aligned} \Gamma &= \bigoplus_n \sigma_z \\ &= \sum_n |c_{2n}\rangle\langle c_{2n}| - |c_{2n+1}\rangle\langle c_{2n+1}| \\ &= P_{\mathrm{even}} - P_{\mathrm{odd}} \ , \end{aligned} \tag{1.24}$$

with $P_{\text{even}}$ and $P_{\text{odd}}$ the projector operators on even and odd sublattices respectively. Due to chiral symmetry, the spectrum of the SSH system is symmetric. Consider an arbitrary eigenstate $|\phi_n\rangle$ with eigenvalue $E_n$, then the state $\Gamma|\phi_n\rangle$ is also an eigenstate with eigenvalue $-E_n$, as follows:

$$\begin{aligned} H\Gamma|\phi_n\rangle &= -\Gamma H|\phi_n\rangle \\ &= -E_n\Gamma|\phi_n\rangle \ . \end{aligned} \tag{1.25}$$

If $E_n \neq 0$, then $|\phi_n\rangle$ and $\Gamma|\phi_n\rangle$ are orthogonal as they have different eigenvalues. We conclude that any eigenstate with non-zero eigenvalue must have an equal weight on both sublattices

$$\begin{aligned} 0 &= \langle\phi_n|\,\Gamma|\phi_n\rangle \\ &= \langle\phi_n|\,(P_{\text{even}} - P_{\text{odd}})\,|\phi_n\rangle \\ \Rightarrow \langle\phi_n|\,P_{\text{even}}\,|\phi_n\rangle &= \langle\phi_n|\,P_{\text{odd}}\,|\phi_n\rangle \ . \end{aligned} \tag{1.26}$$

If on the contrary $|\phi_n\rangle$ is a zero eigenvalue state such as the topological ones, it can be chosen to have zero weight on one sublattice,

$$\begin{aligned} HP_\mu|\phi_n\rangle &= H(I \pm \Gamma)|\phi_n\rangle \\ &= 0 \ , \end{aligned} \tag{1.27}$$

with $P_\mu = P_{\text{even}}, P_{\text{odd}}$.

We now study a semi-infinite lattice with unit cells from $n = 0$ up to infinity. The eigenvalue problem is expressed in matrix form as

$$\begin{gathered} H|\phi\rangle = E|\phi\rangle \\ \begin{pmatrix} 0 & u & 0 & 0 & \\ u & 0 & v & 0 & \\ 0 & v & 0 & u & \\ 0 & 0 & u & 0 & \\ & & & & \ddots \end{pmatrix} \begin{pmatrix} \langle c_0|\phi\rangle \\ \langle c_1|\phi\rangle \\ \langle c_2|\phi\rangle \\ \langle c_3|\phi\rangle \\ \vdots \end{pmatrix} = E \begin{pmatrix} \langle c_0|\phi\rangle \\ \langle c_1|\phi\rangle \\ \langle c_2|\phi\rangle \\ \langle c_3|\phi\rangle \\ \vdots \end{pmatrix} \ . \end{gathered} \tag{1.28}$$

Rewriting the matrix system we find the recurrent equations

$$u\,\langle c_{2n}|\phi\rangle - E\,\langle c_{2n+1}|\phi\rangle + v\,\langle c_{2n+2}|\phi\rangle = 0 \tag{1.29a}$$

$$v\,\langle c_{2n+1}|\phi\rangle - E\,\langle c_{2n+2}|\phi\rangle + u\,\langle c_{2n+3}|\phi\rangle = 0 \ , \tag{1.29b}$$

for $n \geq 0$, subject to the boundary condition

$$-E\,\langle c_0|\phi\rangle + u\,\langle c_1|\phi\rangle = 0 \ . \tag{1.30}$$

For zero eigenvalue states, $\langle c_{2n+1}|\phi\rangle = 0\,\forall n$, thus the equations reduce to

$$u\,\langle c_{2n}|\phi\rangle + v\,\langle c_{2n+2}|\phi\rangle = 0 \ . \tag{1.31}$$

Finally the state is given by

$$\begin{aligned} |\phi\rangle &= \mathcal{N}\sum_{n=0}^{\infty}\left(-\frac{u}{v}\right)^n |c_{2n}\rangle \\ &= \sqrt{1-\left(\frac{u}{v}\right)^2}\sum_{n=0}^{\infty}\left(-\frac{u}{v}\right)^n |c_{2n}\rangle \ , \end{aligned} \tag{1.32}$$

where the second line was obtained forcing normalization on $|\phi\rangle$. In agreement with the previous calculations, we have found a zero eigenvalue state exponentially localized at the edge of the system with perfect sublattice polarization, which is due to chiral symmetry.

The previous calculations assume a pristine lattice, but real systems always contain a certain amount of disorder. We will separately consider disorder which preserves pr breaks chiral symmetry, analyzing the response of the edge states.

For hopping disorder, which preserves chiral symmetry, the intra- and inter-cell hoppings cease to be equal along the lattice. We label the intra-cell hopping on cell $n$ by $u_n$, and the inter-cell between cells $n$ and $n+1$ by $v_n$. The eigenproblem is now given by equations

$$u_n \langle c_{2n}|\phi\rangle - E\langle c_{2n+1}|\phi\rangle + v_n\langle c_{2n+2}|\phi\rangle = 0 \tag{1.33a}$$

$$v_n \langle c_{2n+1}|\phi\rangle - E\langle c_{2n+2}|\phi\rangle + u_{n+1}\langle c_{2n+3}|\phi\rangle = 0 \ , \tag{1.33b}$$

for $n \geq 0$, subject to the boundary condition

$$-E\langle c_0|\phi\rangle + u\langle c_1|\phi\rangle = 0 \ . \tag{1.34}$$

This system also presents a zero eigenvalue solution given by

$$|\phi\rangle = \left[\sum_{n=0}^{\infty}\prod_{m=0}^{n}\left(\frac{u_m}{v_m}\right)^2\right]^{-1/2}\sum_{n=0}^{\infty}\prod_{m=0}^{n}\left(-\frac{u_m}{v_m}\right)|c_{2n}\rangle \ . \tag{1.35}$$

This solution exists as long as the normalization factor remains finite, which is guaranteed if $|v_n| > |u_n|\,\forall n$, and even if $|v_n| \leq |u_n|$ for a finite amount of unit cells. This shows that the topological edge states of the SSH system are robust against chiral symmetry preserving hopping disorder, maintaining their zero eigenvalue and sublattice polarization.

If on the other hand disorder is added in the onsite terms of the hamiltonian, chiral symmetry is broken. An analytical solution for the edge state is not easily found. We therefore turn to numerical methods, including as well a numerical calculation of hopping disordered lattices for comparison. A lattice with hopping (onsite) disorder $d$ is constructed by sampling each hopping (onsite) term from a uniform distribution of width $d$ centered at the pristine value of the parameter. The results reported are averaged over 300 random realizations.

Fig. 1.5 shows the eigenvalue, sublattice polarization, and localization of the edge state as disorder is introduced. We observe that even for high levels of hopping disorder the edge state maintains its zero eigenvalue and perfect sublattice polarization. In contrast, when adding onsite disorder the eigenvalue shows a near zero statistical average, but with large fluctuations

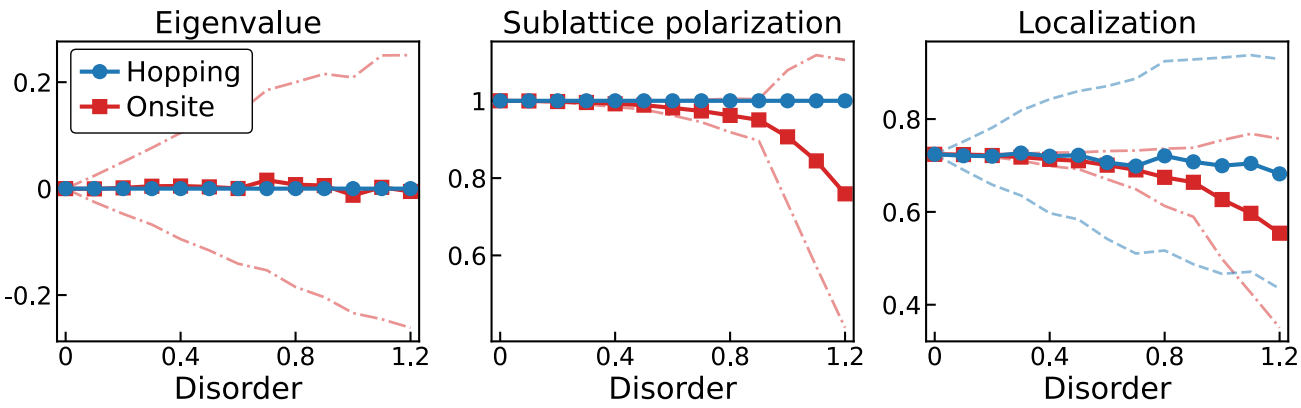


FIGURE 1.5: Eigenvalue, sublattice polarization and localization of the edge state of a semi-infinite SSH lattice in presence of random hopping and onsite disorder, for $u = 0.4$ and $v = 1$. Solid lines with marker show average value, while dashed lines show standard deviation. Sublattice polarization of state $|\phi\rangle$ is calculated by $\langle\phi|P_{\text{even}} - P_{\text{odd}}|\phi\rangle$, while localization is calculated by the IPR (see Fig. 1.4). Zero eigenvalue and perfect sublattice polarization are preserved in presence of hopping disorder, but broken for onsite disorder. The localization is more fragile against onsite disorder as well.

between the different random realizations, even for low levels of disorder. Sublattice polarization of the state is broken as well, and its localization is more sensitive to onsite disorder.

We have proven that symmetry protection grants robustness not only to the topological phase, but also to the emerging edge states and their characteristics. In particular, the topological edge states of the SSH system are strongly robust against hopping disorder which preserves chiral symmetry, maintaining their zero eigenvalue and perfect sublattice polarization. In contrast, introduction of symmetry breaking onsite disorder breaks the topological phase, and no preserved properties of the edge states are observed even for low levels of disorder.

## 1.3 Topological photonics

We have claimed that topological band theory is fundamental to wave phenomena within periodic media; however, development of the theory during the previous section was entirely carried in an electronic framework. Furthermore, in some occasions we explicitly relied on the fermionic statistics of electrons, so how can topological band theory be ported to optical systems? The purpose of this chapter is to show how topological phenomena emerge in photonic lattices. We begin by building a correspondence between solid state and photonic systems. This is done at first by formulating electromagnetism as a hermitian eigenvalue problem, but the correspondence can be pushed further deriving a Schrödinger-like behavior for the electric field within a waveguide array. Having set this basis, we explicitly adapt concepts of topological band theory to photonic lattices and discuss the manifestation of symmetry protected topological phases in optic setups.

### 1.3.1 The electromagnetic eigenvalue problem and the paraxial wave equation

We begin by writing down Maxwell's equations in the absence of sources:

$$\nabla \cdot \mathbf{D}(\mathbf{r},t) = 0 \tag{1.36a}$$

$$\nabla \cdot \mathbf{B}(\mathbf{r},t) = 0 \tag{1.36b}$$

$$\nabla \times \mathbf{E}(\mathbf{r},t) = -\partial_t \mathbf{B}(\mathbf{r},t) \tag{1.36c}$$

$$\nabla \times \mathbf{H}(\mathbf{r},t) = \partial_t \mathbf{D}(\mathbf{r},t)\ , \tag{1.36d}$$

with $\mathbf{E}$ and $\mathbf{B}$ the electric and magnetic fields; and $\mathbf{D}$ and $\mathbf{H}$ the displacement and magnetic H fields[2]. For a static linear media the fields relate as $\mathbf{D}(\mathbf{r},t) = \varepsilon(\mathbf{r})\mathbf{E}(\mathbf{r},t)$, and $\mathbf{B}(\mathbf{r},t) = \mu(\mathbf{r})\mathbf{H}(\mathbf{r},t)$, with $\varepsilon$ and $\mu$ the dielectric and magnetic tensors[3]. Writing the fields as a harmonic mode, $\mathbf{E}(\mathbf{r},t) = \mathbf{E}(\mathbf{r})\mathrm{e}^{-\mathrm{i}\omega t}$ and $\mathbf{H}(\mathbf{r},t) = \mathbf{H}(\mathbf{r})\mathrm{e}^{-\mathrm{i}\omega t}$ we rewrite the equations as

$$\nabla \cdot (\varepsilon\mathbf{E}) = 0 \tag{1.37a}$$

$$\nabla \cdot (\mu\mathbf{H}) = 0 \tag{1.37b}$$

$$\nabla \times \mathbf{E} = \mathrm{i}\omega\mu\mathbf{H} \tag{1.37c}$$

$$\nabla \times \mathbf{H} = -\mathrm{i}\omega\varepsilon\mathbf{E}\ . \tag{1.37d}$$

Decoupling Eq. (1.37c) and (1.37d) yields the generalized eigenvalue problem for the fields

$$\nabla \times \left(\mu^{-1}(\mathbf{r})\nabla \times \mathbf{E}(\mathbf{r})\right) = \omega^2\varepsilon(\mathbf{r})\mathbf{E}(\mathbf{r}) \tag{1.38a}$$

$$\nabla \times \left(\varepsilon^{-1}(\mathbf{r})\nabla \times \mathbf{H}(\mathbf{r})\right) = \omega^2\mu(\mathbf{r})\mathbf{H}(\mathbf{r})\ . \tag{1.38b}$$

For a lossless non-magnetic media, we obtain a standard hermitian eigenvalue problem for the harmonic modes of the magnetic field[4]

$$\nabla \times \left(\varepsilon^{-1}\nabla \times \mathbf{H}\right) = \omega^2\mathbf{H}\ . \tag{1.39}$$

At this point we find a correspondence between the behavior of light in photonic platforms, and that of electrons, which obey their own eigenvalue problem dictated by the time independent Schrödinger equation. We define $\Theta$ as the operator on the left hand side of Eq. (1.39), which plays the role of the hamiltonian, while the photonic eigenstates are labelled by the square of the frequency. The solutions to the electromagnetic eigenvalue problem are usually more complicated than their quantum mechanical analog for two main reasons: (i) The magnetic field is a vector —in contrast to the scalar wave function— which has to obey the divergence condition in Eq. (1.37b) as well. (ii) The electromagnetic *hamiltonian* operator $\Theta$ couples

[2]We will refer to both $\mathbf{B}$ and $\mathbf{H}$ as the magnetic field. It can be inferred from context which one is being alluded.

[3]In the general case the dielectric and magnetic tensors are frequency dependent. We can omit this dependence by considering the mean value of the tensors within a limited frequency range.

[4]For a magnetic media we obtain a generalized eigenvalue problem for the magnetic field, given by the hermitian positive semi-definite operators $\Theta$ and $\mu$. In this scenario the generalized eigenvectors of the problem show similar properties to those of a standard eigenvalue problem by introducing the scalar product $\langle \mathbf{H}_1, \mathbf{H}_2 \rangle = \int \mathrm{d}^3\mathbf{r}\mathbf{H}_1\mu\mathbf{H}_2$ [29, 87]. If the media is not lossless then $\varepsilon$ and/or $\mu$ cease to be positive semi-definite.

the different spatial coordinates, thus the solution is (almost) never separable, even for simple dielectric tensors. These additional complications however, do not limit the fundamental physics behind the analogy. For a periodic dielectric tensor the field may be written in terms of Bloch wave functions, obtaining a band structure for electromagnetic waves in photonic lattices, which dictates the frequencies that are allowed to propagate in the lattice and the direction in which they do. Remarkably, we have found that purely classical electromagnetic waves can emulate quantum phenomena [29, 87]!

Similarities between electromagnetic waves in dielectric media and quantum mechanics are not limited to the fact that both systems are characterized by a hermitian eigenvalue problem, but we may also find a correspondence in terms of the evolution of wave packets. We consider a setup where the dielectric function is modulated only within a plane and it is constant in the perpendicular direction, forming a lattice of coupled waveguides that extend along the latter direction. Under this approach the electric field evolves according to the paraxial wave equation, which is equivalent to the time dependent Schrödinger equation where the propagation axis acts as an effective time coordinate.

We begin from Eq. (1.38a) for a lossless non-magnetic media

$$\nabla \cdot (\nabla \cdot \mathbf{E}) - \nabla^2 \mathbf{E} = \omega^2 \varepsilon \mathbf{E} \ . \tag{1.40}$$

Using Eq. (1.37a) we have we have $\nabla \cdot (\nabla \cdot \mathbf{E}) = -\nabla \cdot (\mathbf{E} \cdot \frac{\nabla \varepsilon}{\varepsilon}) \approx 0$ considering the variation of the dielectric function small in comparison to that of the field. We take the refractive index $n(\mathbf{r})$ as weakly modulated around some value $n_0$, that is $n(\mathbf{r}) = n_0 + \Delta n(\mathbf{r})$ with $\Delta n \ll n_0$, in agreement with experimental conditions where $\Delta n / n_0 \lesssim 10^{-4}$ [54, 88]. The refractive index is periodic in the $xy$ plane, and continuous in the $z$ axis. Substituting the dielectric function for the refractive index $n = c\sqrt{\mu\varepsilon}$, thus $\varepsilon = (n/c)^2 \approx (n_0^2 + 2n_0 \Delta n)/c^2$, the equation now reads

$$\left[ \left( \frac{\omega}{c} n \right)^2 + \nabla^2 \right] \mathbf{E}(\mathbf{r}) = 0 \ . \tag{1.41}$$

By means of the paraxial approximation, the field propagates in a direction *very near* the $z$ axis; thus, the $z$ projection of the wave vector is much larger than the in-plane ones. The electric field takes the form $\mathbf{E}(\mathbf{r}) = \tilde{\mathbf{E}}(\mathbf{r}) \mathrm{e}^{\mathrm{i}\beta_0 z}$, with $\beta_0 = \omega n_0 / c$, for which Eq. (1.41) reads

$$\left[ \nabla_\perp^2 + \partial_z^2 + 2\mathrm{i}\beta_0 \partial_z + \beta_0^2 + \left( \frac{\omega}{c} n \right)^2 \right] \tilde{\mathbf{E}}(\mathbf{r}) = 0 \ , \tag{1.42}$$

with $\nabla_\perp$ the nabla operator acting only in the $xy$ plane. As $\tilde{\mathbf{E}}$ only contains a $z$ dependence which accounts for the small deviation of the propagation direction from the $z$ axis, we neglect the term $\partial_z^2 \tilde{\mathbf{E}}$. We finally obtain the *paraxial wave equation* for the electric field

$$\mathrm{i}\partial_z \tilde{\mathbf{E}}(\mathbf{r}) = \left[ -\frac{\nabla_\perp^2}{2\beta_0} - \beta_0 \frac{\Delta n(\mathbf{r})}{n_0} \right] \tilde{\mathbf{E}}(\mathbf{r}) \ . \tag{1.43}$$

Remarkably, it has the same form of the time dependent Schrödinger equation with the following remarks: Just as in the electromagnetic eigenvalue problem, the quantum wave function is

represented by a fully classical field. The paraxial equation dictates the evolution of a harmonic field of frequency $\omega$ along the propagation axis $z$. Thus, the steady states of this equation are labelled by a $z$ axis propagation constant, instead of energy or frequency. The role of the hamiltonian is played by the operator in the right hand side of Eq. (1.43), with the modulation of the refractive index $\Delta n$ acting as the potential. Electromagnetic waves propagate with more amplitude in regions with a higher refractive index, which act as waveguides that couple due to an evanescent overlap. In principle we considered $\Delta n$ constant along the propagation axis, however it can be a smooth function of $z$ as well, emulating time dependent hamiltonians [88]. Finally, if the dielectric function is periodically modulated within the $xy$ plane, the field is written as Bloch wave functions with reciprocal space defined only on the plane, and the waveguide array is characterized by a band structure where the eigenvalues correspond to the $z$ axis propagation constant.

### 1.3.2 Topological photonics

Having shown that photonic lattices are characterized by a band structure, in analogy with crystals, the implementation of topological band theory as discussed previously is rather straight forward. However, we must make minor adjustments accounting for fundamental differences between electrons and electromagnetic waves, which will be described during this section. We will also briefly review some implementations of topological lattices in optic platforms, and in particular discuss the realization of the SSH model in a waveguide array.

In electronic systems a topological invariant is typically defined by the sum over all occupied bands of a quantity that is calculated within each individual band, and it remains invariant as long as the Fermi energy lies within a finite gap. For optic systems this approach is no longer valid as we are no longer studying fermions. In optic systems any mode can be macroscopically excited without the need to populate the modes with lower frequency, therefore it is of no purpose to define invariants based on a sum over occupied bands. We may only define topological invariants for each band individually, and for them to remain invariant we require both gaps that limit the bandwidth to remain open [89].

We must also consider that, while electrons populate the band structure within equilibrium conditions and may remain in the material for an infinite time period, electromagnetic waves can only exist within a media for a finite time range [29, 90]. This accounts for several differences regarding the experimental observation of topology. In condensed matter systems the footprints of topology are typically observed via quantum transport setups under the effects of external electric and/or magnetic fields [6, 7]. In contrast, for optic systems the states must be excited by means of external driving. The behavior of the field can be observed continuously during a finite time range by means of dissipative processes such as radiation, and in order to study its conservative dynamics light can only be collected at the output of the lattice employing photodetectors or antennas for example [29].

The particular experimental implementations of photonic lattices does not demand for a redefinition of topological band theory as introduced in the previous chapter. From a theoretical perspective the excitation spectrum of the field is obtained in a completely analogous way as in electronic systems, therefore topological phases and invariants are defined equivalently. Never-

theless, the effects of losses and driven/dissipative dynamics in optical systems does limit the capacity to replicate solid state systems as they account for non hermitian terms in the hamiltonian [91, 92]. These effects may be included by perturbative terms over a hermitian hamiltonian in order to replicate quantum systems, which are fundamentally hermitian [87, 93][5].

It is rather short sighted on our behalf to claim that as the electromagnetic field obeys an eigenvalue problem, electronic quantum phenomena can be replicated in optics only by modulating the dielectric function of the media. Topological phenomena in electronic systems occur not only because of the geometry of the lattice, but also by means of interactions with external fields [5, 55, 56], or spin interactions [22–24], among others [6, 7, 17]. In order to obtain a wide variety of photonic topological systems all these phenomena must be replicated as well. For instance, photonic IQHE states have been reported by using gyromagnetic photonic crystals allowing electromagnetic waves to interact with an external magnetic field [95–97]. As well, photonic analogs of the quantum spin Hall insulator have been obtained in an array of optical ring resonators, with clockwise and anti-clockwise polarization of each resonator acting as a pseudospin degree of freedom [90, 98]. These are only a few examples among many others [29, 31] on how various topological phases can be replicated in optic systems. However, as this thesis focuses on the SSH system, whose topological order is due to the dimerization of the one-dimensional lattice, we may rely only on the spatial modulation of the refractive index [54, 99].

Topological order in the SSH system is due to the dimerization of the one-dimensional lattice. Thus, it is realized as a waveguide array solely by means of a one-dimensional refractive index modulation [54, 100], in contrast to the examples discussed previously. A refractive index as portrayed in Fig. 1.6 forms identical waveguides in place of the sites —given by identical peaks in $\Delta n$— with staggered couplings. If confinement within each waveguide is sufficiently strong, the tight binding approximation, also referred to as coupled mode theory in photonic contexts, may be applied, expressing the field of the system as a linear combination of the bound modes

[5] As a silver lining, even though driven/dissipative dynamics are a limitation when studying hermitian systems in optic platforms, they present a remarkable experimental advantage for the study of non-hermitian topological phases, in particular parity-time symmetric systems [27, 94].

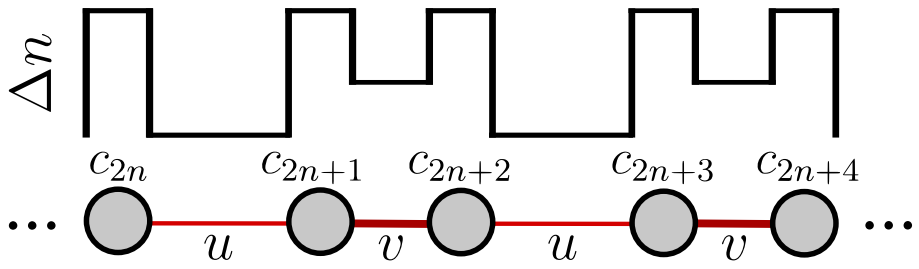


FIGURE 1.6: Refractive index modulation for an SSH waveguide array. Peaks in the refractive index form waveguides in place of the sites. The hopping amplitude may be controlled by proximity of the waveguides, or by changing the refractive index in between the waveguides.

at each waveguide [101–104]. Under this approach the *hamiltonian matrix* elements are

$$H_{n,m} = \int \mathrm{d}x \tilde{\mathbf{E}}_n^*(x) \left[ -\frac{\partial_x^2}{2\beta_0} - \beta_0 \frac{\Delta n(x)}{n_0} \right] \tilde{\mathbf{E}}_m(x) \ , \tag{1.44}$$

with $\tilde{\mathbf{E}}_n(x)$ the bound mode of the field at waveguide $n$. For a stationary state of the form $\tilde{\mathbf{E}}(x,z) = \tilde{\mathbf{E}}(x)\mathrm{e}^{-\mathrm{i}\beta z}$, with $\tilde{\mathbf{E}}(x) = \sum c_n \tilde{\mathbf{E}}_n(x)$, we obtain the *hamiltonian* eigenvalue problem

$$\beta c_n = \sum_m H_{n,m} c_m \ . \tag{1.45}$$

We conclude that the SSH model for polyacetylene can be realized in a photonic waveguide array by correctly engineering the refractive index of the optic media, obtaining the same hamiltonian representation as its condensed matter version. Therefore, the photonic SSH system has a non trivial topological phase for $|u| < |v|$, which is characterized by the Zak phase and protected by the symmetry

$$\mathcal{H}_k = -\sigma_z \mathcal{H}_k \sigma_z \ , \tag{1.46}$$

with $\mathcal{H}_k$ the *hamiltonian* matrix in reciprocal space. Lets recall however that this expression was obtained in section 1.2.1 starting form the chiral operator $\hat{\Gamma}$, whose action on the fermionic annihilation operators is given by Eq. (1.17). This approach is no longer valid, as the electric field is classical. Furthermore, if we quantize the field and describe the system by a second quantization formalism, the annihilation and creation operators would be bosonic, and Eq. (1.46) would not be obtained. Thus, referring to the photonic SSH system, we understand chiral symmetry not as the composition of particle-hole symmetry and TRS, but as the existence of a unitary local operator $\hat{\Gamma}$ such that $\hat{H} = -\hat{\Gamma}^\dagger \hat{H} \hat{\Gamma}$ [86]. This guarantees that all the diagonal terms in the hamiltonian are proportional to the identity, allowing for the Zak phase to be a well defined topological invariant.

# Chapter 2

# Quantum optics

Communication systems rely on the transmission of information by means of a physical system. From verbal communication where interlocutors exchange information through the propagation of acoustic waves, to telecommunication where information is encoded in electromagnetic waves. Encoding information within quantum systems gives birth to the area of quantum information, where enhanced communication protocols may be formulated taking advantage of quantum phenomena with no classical analog, such as entanglement. Photonic platforms stand as a promising route to achieving efficient quantum information processing, due to their non-interacting, decoherence-free nature, and the wide-variety of optical techniques to efficiently manipulate photonic states [46, 47, 105]. Quantum information may be encoded in a physical system in two forms, by discrete or continuous variables. Photonic discrete variable schemes employ photon polarization, or photon number within an optical mode as the relevant degree of freedom, while continuous variable schemes describe quantum information in terms of the quadratures of an optical mode. Our focus is on the latter, in particular squeezed states of light, which serve as the primary entanglement resource for continuous variable quantum information processing [43, 44, 106, 107].

In this chapter we introduce a framework for quantum optics, with an emphasis on single-mode and two-mode squeezed states. This will provide to the reader the necessary background on squeezing in order to later study its propagation in photonic topological lattices. We begin developing the quantization of the electromagnetic field in section 2.1, and defining a phase space representation for quantum states. In section 2.2 we focus on Gaussian states, discussing their representation, the characterization of entanglement, and introduce a numerical method to simulate their time evolution. We finally discuss in detail the behavior of squeezed states in section 2.3.

## 2.1 Quantization of the electromagnetic field

Within the classical regime, a harmonic mode of the electromagnetic field with wave vector $\mathbf{k}$ and frequency $\omega = c|\mathbf{k}|$, propagating in vacuum is given by the electric and magnetic fields

$$\mathbf{E}(\mathbf{r}, t) = \hat{\mathbf{e}} E_0 \mathrm{e}^{\mathrm{i}(\mathbf{kr} - \omega t)} + \text{c.c.} \tag{2.1a}$$

$$\mathbf{B}(\mathbf{r},t) = -\mathrm{i}\frac{\mathbf{k}\times\hat{\mathbf{e}}}{c|\mathbf{k}|}E_0\mathrm{e}^{\mathrm{i}(\mathbf{kr}-\omega t)} + \text{c.c.}\ , \tag{2.1b}$$

with $\hat{\mathbf{e}}$ the polarization unit vector. The hamiltonian of the system is

$$\begin{aligned} H &= \frac{1}{2}\int \mathrm{d}^3\mathbf{r}\,\varepsilon_0\mathbf{E}^2 + \frac{1}{\mu_0}\mathbf{B}^2 \\ &= 2\varepsilon_0 V|E_0|^2\ , \end{aligned} \tag{2.2}$$

with $V = \int \mathrm{d}^3\mathbf{r}$. Defining the variables $q$ and $p$ by $E_0 = (2\sqrt{\varepsilon_0 V})^{-1}(\omega q + \mathrm{i}p)$ the hamiltonian takes the form of a harmonic oscillator

$$H = \frac{1}{2}p^2 + \frac{\omega^2}{2}q^2\ , \tag{2.3}$$

where superpositions of the electric and magnetic fields play the role of position and momentum. The standard procedure for quantizing the harmonic oscillator may now be applied, promoting $q$ and $p$ to operators, $q \to \hat{q}$ and $p \to \hat{p}$, subject to the canonical commutation relation $[\hat{q},\hat{p}] = \mathrm{i}\hbar$. The annihilation and creation operators are defined respectively as

$$a = (2\hbar\omega)^{-1/2}(\omega\hat{q} + \mathrm{i}\hat{p}) \tag{2.4a}$$

$$a^\dagger = (2\hbar\omega)^{-1/2}(\omega\hat{q} - \mathrm{i}\hat{p})\ , \tag{2.4b}$$

which obey the commutation relation $[a, a^\dagger] = 1$. We obtain the final form of the hamiltonian

$$\hat{H} = \hbar\omega\left(a^\dagger a + \frac{1}{2}\right)\ , \tag{2.5}$$

where the $\hat{H}$ fashions a well earned hat showing its promotion to an operator. We find discrete energy levels $E_n = \hbar\omega(n + 1/2)$, where the second term corresponds to the vacuum fluctuations energy, and $n = 0, 1, \ldots$ indicates the number of photons in the field, each one with energy $\hbar\omega$. Any state of the field may be represented in the Fock basis $\{|n\rangle\}_{n=0}^{\infty}$, corresponding to states with a well defined photon number, eigenstates of the number operator $\hat{n} = a^\dagger a$. The action of the operators $a$ and $a^\dagger$ on the Fock states is given by

$$a|n\rangle = \sqrt{n}|n-1\rangle \tag{2.6a}$$

$$a^\dagger|n\rangle = \sqrt{n+1}|n+1\rangle\ , \tag{2.6b}$$

representing respectively the annihilation and creation of a photon. Note that the commutation relation defined for $a$ and $a^\dagger$ determines the bosonic character of photons.

In terms of quantum information, Fock states constitute a discrete variable description of the field, serving for numerous protocols. Unfortunately, generation of Fock states is exceptionally challenging, constituting a major limitation for the implementation of photonic discrete variable quantum information [46, 47]. Protocols for deterministic generation of Fock states, even up to $n \sim 100$, have been recently proposed [108, 109]. However, from an experimental perspective, a deterministic source of high-fidelity indistinguishable photons with correct coupling to optic platforms does not exist [47], and generation of high fidelity Fock states is currently achieved only for a low photon number [110, 111].

A continuous variable description of the field is achieved defining the hermitian quadrature operators

$$X_1 = \frac{a + a^\dagger}{2} \tag{2.7a}$$

$$X_2 = \frac{a - a^\dagger}{2\mathrm{i}} \ , \tag{2.7b}$$

which correspond to adimensional *position* and *momentum* variables. The quadratures obey the commutation relation $[X_1, X_2] = \mathrm{i}/2$, and therefore a Heisenberg-like uncertainty principle

$$\langle \Delta X_1 \rangle \langle \Delta X_2 \rangle \geq 1/4 \ . \tag{2.8}$$

We introduce the continuous set of eigenvalues and eigenstates of the quadrature operators $X_1$ and $X_2$, labelled by $q$ and $p$ respectively, which satisfy

$$X_1|q\rangle = q|q\rangle \tag{2.9a}$$

$$X_2|p\rangle = p|p\rangle \ . \tag{2.9b}$$

Each set of eigenstates, $\{|q\rangle\}$ or $\{|p\rangle\}$, constitutes a complete basis of the Hilbert space, and are related by the Fourier transform

$$|q\rangle = \pi^{-1/2} \int \mathrm{d}p \, \mathrm{e}^{-2\mathrm{i}qp} |p\rangle \tag{2.10a}$$

$$|p\rangle = \pi^{-1/2} \int \mathrm{d}q \, \mathrm{e}^{2\mathrm{i}qp} |q\rangle \ , \tag{2.10b}$$

with $q$ and $p$ ranging from $-\infty$ to $\infty$.

The fields —now as quantum operators— are written in terms of the quadratures as

$$\mathbf{E}(\mathbf{r}, t) = \hat{\mathbf{e}} \sqrt{\frac{2\hbar\omega}{\varepsilon_0 V}} \left[ X_1 \cos(\mathbf{kr} - \omega t) - X_2 \sin(\mathbf{kr} - \omega t) \right] \tag{2.11a}$$

$$\mathbf{B}(\mathbf{r}, t) = \frac{\mathbf{k} \times \hat{\mathbf{e}}}{c|\mathbf{k}|} \sqrt{\frac{2\hbar\omega}{\varepsilon_0 V}} \left[ X_1 \sin(\mathbf{kr} - \omega t) + X_2 \cos(\mathbf{kr} - \omega t) \right] \ , \tag{2.11b}$$

where we see that just as in the classical regime, the quadratures represent amplitudes of the fields oscillating with a $\pi/2$ phase difference. Any physical relevance of the phase of the fields must be in terms of an appropriate phase reference. In the general case, a $\phi$ rotated quadrature is defined as $X(\phi) = X_1 \cos(\phi) + X_2 \sin(\phi)$, from which it is evident that $X_1 = X(0)$, $X_2 = X(\pi/2)$ and the commutation relation $[X(\phi), X(\phi + \pi/2)] = \mathrm{i}/2$ holds for any rotation angle. These observables are measured by phase sensitive measurement techniques, which generally rely on interference between the mode of interest of the field and a strong local oscillator at the same frequency, which sets the phase reference [112, 113]. Note that the orthogonal quadratures $X_1$ and $X_2$ correspond to conjugate variables and thus cannot be measured simultaneously.

At this point we have discussed the quantum description of a single mode of the electromagnetic field as a discrete and continuous variable. Any more complex state can be expanded as a superposition of the involved harmonic modes $\{a_n\}_n$, which obey the commutation relations

$[a_n, a_{n'}^\dagger] = \delta_{n,n'}$ and $[a_n, a_{n'}] = 0$. The quantization formalism developed so far is well suited for the description of a photonic lattice under the tight-binding (coupled mode) approximation. For a waveguide array, a bosonic operator $a_n$ is introduced for the bound mode at the $n$-th waveguide, obtaining a hamiltonian describing the linear propagation of the field

$$\hat{H} = \sum_n \omega_n a_n^\dagger a_n + \sum_{n \neq m} H_{n,m} a_n^\dagger a_m \ , \tag{2.12}$$

where the first term represents uncoupled waveguides, and the second represents hopping processes, where a photon is annihilated at mode $m$ and created at mode $n$ with amplitude $H_{n,m}$.

### 2.1.1 Phase space representation: The Wigner function

The classical notion of phase space dictates that the state of a classical system with $N$ degrees of freedom is completely determined by a point in a $2N$-dimensional phase space, which corresponds to the space spanned by the generalized positions $\{q_n\}_{n=0}^{N-1}$ and their conjugate momenta $\{p_n\}_{n=0}^{N-1}$. The statistical average of any observable $\mathcal{O}(\vec{q}, \vec{p})$, with $\vec{q} = (q_0, \ldots, q_{N-1})$ and $\vec{p} = (p_0, \ldots, p_{N-1})$, is

$$\overline{\mathcal{O}} = \int \mathrm{d}^N q \, \mathrm{d}^N p \, \mathcal{O}(\vec{q}, \vec{p}) f(\vec{q}, \vec{p}) \ , \tag{2.13}$$

with $f(\vec{q}, \vec{p})$ the statistic probability density function for the system being in a given point of phase space, which corresponds to a $2N$-dimensional Dirac delta function for a system of which we have absolute knowledge.

We wish do adapt this concept to the quantum regime, where instead of statistical averages $\overline{\mathcal{O}}$ we focus on probabilistic averages $\langle \mathcal{O} \rangle$ due to the intrinsic quantum uncertainty of the system. Following the correspondence between the electromagnetic field and a harmonic oscillator, the quantum optics phase space is spanned by the set of conjugate quadratures of each mode of the field $\{X_1^{(n)}, X_2^{(n)}\}_{n=0}^{N-1}$, with $X_\mu^{(n)}$ the quadrature operator $\mu$ ($\mu = 1, 2$) of the $n$-th mode. We now seek for a phase space quantum distribution function of the state to take the place of $f(\vec{q}, \vec{p})$ in the quantum mechanical version of Eq. (2.13).

We introduce the Wigner function $W$ of a quantum state as the Fourier transform of the off-diagonal elements of its density matrix $\rho$ [112, 114][1]

$$W(\vec{q}, \vec{p}) = \left(\frac{2}{\pi}\right)^N \int \mathrm{d}^N u \, \mathrm{e}^{4\mathrm{i}\vec{p}\vec{u}} \langle \vec{q} + \vec{u} | \rho | \vec{q} - \vec{u} \rangle \ , \tag{2.14}$$

with $\vec{q}$ and $\vec{p}$ the set of labels for the eigenmodes of the quadratures of the $N$ modes of the field. The Wigner function is completely determined by the state of the field, and vice versa. Any observable $\mathcal{O}$ may be written in terms of the bosonic operators $\{a_n\}_{n=0}^{N-1}$ and $\{a_n^\dagger\}_{n=0}^{N-1}$, where the operator is said to be symmetrically ordered if the products of annihilation and creation operators are symmetrized. For a symmetrically ordered observable $\mathcal{O}_\mathrm{S}$, its expectation value

[1] In this work we will only study pure states of the field $|\psi\rangle$, for which $\rho = |\psi\rangle\langle\psi|$. However, we introduce this formalism in terms of an arbitrary density matrix which applies to mixed states, accounting for a statistical average as well.

is given by[2]

$$\langle \mathcal{O}_{\mathrm{S}} \rangle = \int \mathrm{d}^N q \, \mathrm{d}^N p \, \mathcal{O}_{\mathrm{S}}(\vec{q}, \vec{p}) W(\vec{q}, \vec{p}) \ , \tag{2.15}$$

where $\mathcal{O}_{\mathrm{S}}(\vec{q}, \vec{p})$ corresponds to the expansion of $\mathcal{O}_{\mathrm{S}}$ in terms of the bosonic operators, replacing $a_n \to q_n + \mathrm{i} p_n$.

The Wigner function plays the role of the probability distribution function in the quantum mechanical version of Eq. (2.13). However, it is deemed a quasi-distribution function as it may take negative values —for Fock states for example [112]—. Negativity of the Wigner function serves as a sufficient —yet not necessary— landmark for the quantum character of a given state. It satisfies the normalization condition

$$\int \mathrm{d}^N q \, \mathrm{d}^N p \, W(\vec{q}, \vec{p}) = 1 \ , \tag{2.16}$$

and its marginal distribution over each variable yields the probability distribution function of the state in the corresponding basis

$$\int \mathrm{d}^N p \, W(\vec{q}, \vec{p}) = \langle \vec{q} | \rho | \vec{q} \rangle \tag{2.17a}$$

$$\int \mathrm{d}^N q \, W(\vec{q}, \vec{p}) = \langle \vec{p} | \rho | \vec{p} \rangle \ . \tag{2.17b}$$

## 2.2 Gaussian states

Gaussian states, defined as quantum states with a Gaussian representation, are of great relevance within a photonic continuous variable framework. For example, the vacuum state, which is the ground state of the free field, and squeezed states, which serve as the primary source for continuous variable entanglement, are both Gaussian. Furthermore, linear and quadratic hamiltonians correspond to Gaussian transformations, which map Gaussian states to Gaussian states [43, 44]. In this section we define Gaussian states and briefly introduce a few paradigmatic examples of them. We also develop a numerical method to simulate time evolution and describe an entanglement criterion, which will be required for the characterization of squeezed states and for the study of squeezed states in a topological photonic lattice.

Gaussian states, by definition, are represented by a Gaussian Wigner function, and are therefore fully characterized by their first and second statistic moments [43]. For an $N$ mode system, we define the $2N$ dimensional vector $\hat{\chi}$ containing the set of all conjugate quadratures,

$$\hat{\chi} = \left( X_1^{(0)}, X_2^{(0)}, \ldots, X_1^{(N-1)}, X_2^{(N-1)} \right) \ . \tag{2.18}$$

The first moment is defined by the mean value of the quadratures $\langle \hat{\chi} \rangle$, and the second moment is the correlation matrix

$$V_{n,m} = \frac{1}{2} \left\langle [\Delta \hat{\chi}_n \Delta \hat{\chi_m}]_+ \right\rangle \ , \tag{2.19}$$

[2]For observables with *normal* or *anti-normal* ordering, meaning all annihilation operators placed to the right or to the left of the creation operators respectively, other quantum distribution functions are defined, namely the $P$- and $Q$-distributions [112].

with $\Delta\hat{\chi_n} = \hat{\chi}_n - \langle\hat{\chi_n}\rangle$. At this point a generalized version of the uncertainty principle may be stated as

$$V - \Lambda \geq 0 \ , \tag{2.20}$$

with $\Lambda_{n,m} = \frac{1}{2}\langle[\hat{\chi}_n, \hat{\chi}_m]\rangle$, meaning that the matrix on the left hand side of Eq. (2.20) must only have non-negative eigenvalues [115]. The Wigner function of a Gaussian state is written as

$$W(\chi) = \frac{|V|^{-1/2}}{(2\pi)^N} \exp\left(-\frac{1}{2}(\chi-\mu)V^{-1}(\chi-\mu)^T\right) \ , \tag{2.21}$$

with $\chi$ the $2N$-dimensional vector containing the eigenvalues of $\hat{\chi}$, and $|V|$ the determinant of $V$.

### 2.2.1 Some examples of Gaussian states

We briefly introduce three elementary types of Gaussian states, which will serve for the discussions in the following sections [43, 113].

The **vacuum state** $|0\rangle$ corresponds to the ground state of the free electromagnetic field. It may be thought of as a Fock state with zero photon number, a coherent state with zero coherent amplitude, or a thermal state at zero temperature. The quadratures have zero expectation value, with variance $\langle(\Delta X)^2\rangle_{\text{vacuum}} = 1/4$ for any rotation angle. The correlation matrix $V = \mathrm{I}/4$ is proportional to the identity matyrix I, thus the quadratures are completely uncorrelated. The Wigner function is symmetric with respect to the phase space origin, as shown in Fig. 2.1-(a).

A **coherent state** $|\alpha\rangle$ is defined as an eigenstate of the annihilation operator with eigenvalue $\alpha \in \mathbb{C}$. The uncertainty in the quadratures, as well as the correlation matrix is identical as those of vacuum, however the expectation value of the quadratures are $\langle X_1\rangle = \mathrm{Re}\,\alpha$ and $\langle X_2\rangle = \mathrm{Im}\,\alpha$. Coherent states correspond to phase space displaced vacuum states, as shown by their Wigner function in Fig. 2.1-(b), defined by the displacement operator $D(\alpha) = \exp(\alpha a^\dagger - \alpha^* a)$ acting on vacuum $|\alpha\rangle = D(\alpha)|0\rangle$. The expectation value of the field is

$$\mathbf{E}(\mathbf{r},t) = \hat{\mathbf{e}}\sqrt{\frac{2\hbar\omega}{\varepsilon_0 V}}\mathrm{Re}\left[\alpha \mathrm{e}^{\mathrm{i}(\mathbf{kr}-\omega t)}\right] \tag{2.22a}$$

$$\mathbf{B}(\mathbf{r},t) = \frac{\mathbf{k}\times\hat{\mathbf{e}}}{c|\mathbf{k}|}\sqrt{\frac{2\hbar\omega}{\varepsilon_0 V}}\mathrm{Re}\left[\alpha \mathrm{e}^{\mathrm{i}(\mathbf{kr}-\omega t-\pi/2)}\right] \ . \tag{2.22b}$$

In the high amplitude limit $|\alpha|^2 \gg 1$ the vacuum-like fluctuations are negligible, thus coherent states correspond to a description of classical light within the quantum optics formalism.

**Thermal states** can describe the radiation emitted by a cavity in thermal equilibrium. Unlike the previously introduced states they are mixed states, given by the density matrix

$$\rho_{\mathrm{th}} = \sum_m \frac{\bar{n}^m}{(\bar{n}+1)^{m+1}} |m\rangle\langle m| \ , \tag{2.23}$$

with $\bar{n} = \left[\exp\left(\hbar\omega/k_{\mathrm{B}}T\right) - 1\right]^{-1}$ the mean photon number. Just as vacuum and coherent states, the correlation matrix is proportional to the identity $V = (2\bar{n}+1)\mathrm{I}/4$, but thermal states are not minimal uncertainty states. The Wigner function is shown in Fig. 2.1-(c).

### 2.2.2 A numerical method for the evolution of Gaussian states

In this section we develop a simple method for the numerical simulation of the evolution of Gaussian states. We consider a set of $N$ bosonic operators $\{a_n\}_{n=0}^{N-1}$, in a setup of coupled waveguide arrays, under the influence of a generic, propagation axis independent, bilinear hamiltonian $\hat{H} = \sum_{n,m} H_{n,m} a_n^\dagger a_m$. Our method relies on the fact that the states are Gaussian, and are therefore completely determined by the mean values of the quadratures $\langle\hat{\chi}\rangle$, and the correlation matrix $V$. These quantities can be obtained from the vector $\mu$, and the two matrices $N$ and $M$, defined by their elements $\mu_n = \langle a_n\rangle$, $N_{n,m} = \langle a_n^\dagger a_m\rangle$, and $M_{n,m} = \langle a_n a_m\rangle$. Thus, a many photon problem in a Hilbert space $N$ times that of a single harmonic mode, which is in turn infinite-dimensional, is reduced to the calculation of one $N$-dimensional vector, and two $N \times N$-dimensional matrices, with no loss of information.

The bosonic operators obey the Heisenberg-like equation

$$-\mathrm{i}\frac{\mathrm{d}a_n}{\mathrm{d}z} = \left[\hat{H}, a_n\right] \ , \tag{2.24}$$

where the propagation axis $z$ acts as an effective time coordinate. The solution to the equation is given by $a_n(z, z_0) = \hat{U}^\dagger(z, z_0) a_n(z_0) \hat{U}(z, z_0)$, with $\hat{U}(z, z_0) = \exp(-\mathrm{i}\hat{H}(z - z_0))$. In the following

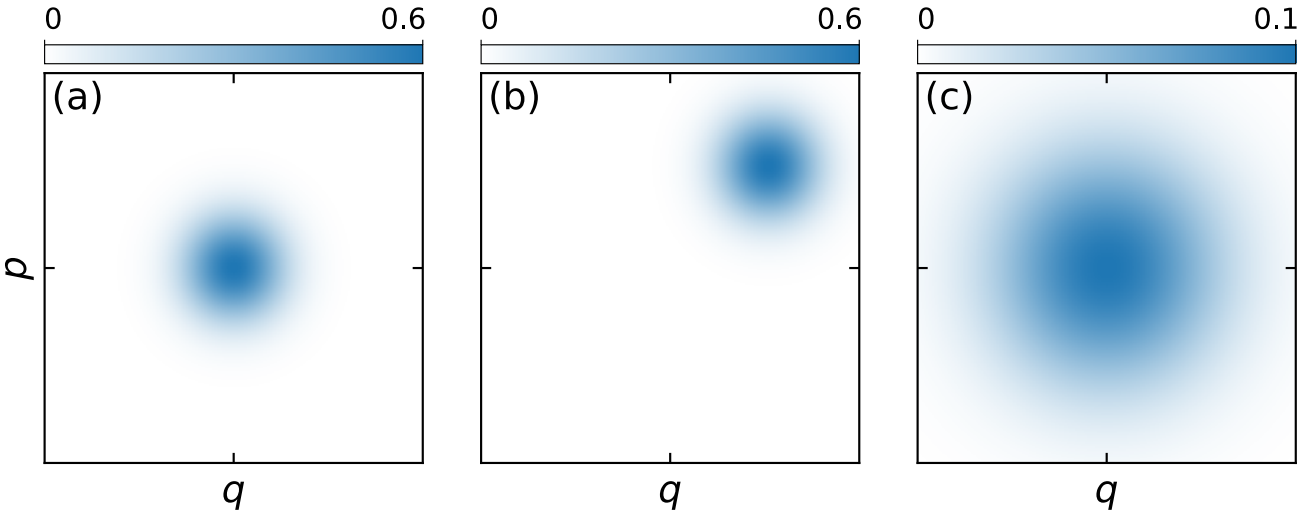


FIGURE 2.1: Wigner function for: **(a)** Vacuum state. **(b)** Coherent state with $\alpha = 2\mathrm{e}^{\mathrm{i}\pi/4}$, which takes the form of the vacuum state displaced in phase space. **(c)** Thermal state with $\bar{n} = 2$, which is not a minimal uncertainty state.

we take $z_0 = 0$ for simplicity. Employing the Baker-Hausdorff lemma[3], we obtain

$$a_n(z) = \sum_k \frac{(\mathrm{i}z)^k}{k!} \underbrace{[\hat{H}, \ldots, [\hat{H}, a_n(0)]]}_{\text{k times}} \ . \tag{2.25}$$

We find that $\left[\hat{H}, \ldots, \left[\hat{H}, a_n\right]\right] = \sum_m (H^k)_{n,m} a_m$ for $k$ nested commutators, and thus the $z$ evolution of the operators is

$$a_n(z) = \sum_m \left(\mathrm{e}^{-\mathrm{i}Hz}\right)_{n,m} a_m(0) \ . \tag{2.26}$$

Note that the $H$ has lost its hat, as it is now only the matrix representation of $\hat{H}$ on the $\{a_n\}_n$ basis. As well, we obtain the matrix representation of the $z$ evolution operator $U = \mathrm{e}^{-\mathrm{i}Hz}$. Eq. (2.26) reduces the $z$ evolution to a matrix multiplication, however, it requires taking the exponential of a matrix at each *time* step. Let $Q$ be the matrix containing the eigenvectors of $H$ in its columns, and $\tilde{H}$ the diagonal form of $H$, namely $\tilde{H} = Q^\dagger H Q$. We now write $U = Q^\dagger \mathrm{e}^{-\mathrm{i}\tilde{H}z} Q$, thus a single diagonalization of the hamiltonian is required, and each *time* step now reduces to the exponential of scalars, and matrix multiplications. The evolution of $\mu$, $N$, and $M$ is given by

$$\mu_n(z) = \sum_m U_{n,m}(z) \mu_n(0) \ , \tag{2.27a}$$

$$N_{n,m}(z) = \sum_{k,l} U^*_{n,k}(z) U_{m,l}(z) N_{k,l}(0) \ , \tag{2.27b}$$

$$M_{n,m}(z) = \sum_{k,l} U_{n,k}(z) U_{m,l}(z) M_{k,l}(0) \ . \tag{2.27c}$$

The presented evolution method is exact, and only numerical errors may limit its precision. Furthermore, the evolution from $z_0$ to an arbitrary final point $z_f$ may be computed in a single calculation, with no need of defining an iteration *time* step. A *time* step can be introduced if knowledge of the field is required at intermediate points between $z_0$ and $z_f$, but the precision of the evolution is not affected by the chosen step. Note that the evolution obtained for the bosonic operators $\{a_n\}_n$, and the defined variables $\mu$, $N$, and $M$ applies to non-Gaussian states as well, however these are not fully determined by the defined variables, and thus the numerical method does not account for the full time evolution of a general state of the field.

### 2.2.3 Entanglement criterion for continuous variable systems

Having introduced Gaussian states, we now describe an entanglement criterion for a bipartite continuous variable system [44, 116], which will later serve to characterize entanglement in squeezed states. Our starting point is Peres's partial transpose criterion [117]: A density matrix $\rho$ of the bipartite system composed by subsystems A and B is separable if and only if it can be written as the sum of direct products

$$\rho = \sum_n p_n \, \rho_n^{(\mathrm{A})} \otimes \rho_n^{(\mathrm{B})} \ , \tag{2.28}$$

[3]The Baker-Hausdorff lemma: $\mathrm{e}^A B \mathrm{e}^{-A} = B + [A, B] + \frac{1}{2}[A, [A, B]] + \cdots + \frac{1}{n!} \underbrace{[A, \ldots, [A, B]]}_{\text{n times}} + \ldots$

with $\rho_n^{(\mathrm{A})}$ and $\rho_n^{(\mathrm{B})}$ density matrices in each subsystem, and $p_n > 0\,\forall n$ satisfying $\sum p_n = 1$. Therefore a necessary criterion for separability is that the partial transposition of one subsystem, e.g. $\rho^{(\mathrm{A})} \to (\rho^{(\mathrm{A})})^{\mathrm{t}}$, yields a physical density matrix $\tilde{\rho} = \sum p_n \, (\rho_n^{(\mathrm{A})})^{\mathrm{t}} \otimes \rho_n^{(\mathrm{B})}$, as $(\rho^{(\mathrm{A})})^{\mathrm{t}}$ is a physical density matrix in subsystem A. Transposition of a hermitian density matrix corresponds to complex conjugation, which in turn corresponds to time-reversal. Thus upon transposition, the *momentum* coordinates $\{p_n\}_n$ change sign, while the *position* coordinates $\{q_n\}_n$ remain invariant. A bipartite quantum state with Wigner function $W(\chi^{(\mathrm{A})}, \chi^{(\mathrm{B})})$ is separable if $\tilde{W} = W(\Gamma_{\mathrm{A}}\chi^{(\mathrm{A})}, \chi^{(\mathrm{B})})$ is a physical Wigner function as well, with $\Gamma_A = \mathrm{diag}(1, -1, \ldots, 1, -1)$. Partial transposition of subsystem A is represented in the correlation matrix as $V \to \tilde{V} = \Gamma V \Gamma$, with $\Gamma = \Gamma_A \oplus \mathrm{I}_B$, and $\mathrm{I}_B$ the identity matrix of subsystem $B$. For $\tilde{W}$ to be a physical Wigner function, $\tilde{V}$ must satisfy the generalized uncertainty principle stated in Eq. (2.20). Finally, for a quantum state with correlation matrix $V$, the Peres-Horodecki criterion for continuous variable systems states that a sufficient criterion for entanglement is

$$\tilde{V} - \Lambda \ngeq 0 \ , \tag{2.29}$$

with $\tilde{V}$ the partially transposed correlation matrix [116]. The minimum eigenvalue of the matrix on the left side of Eq. (2.29) thus serves as an entanglement measure.

## 2.3 Squeezed states

Squeezed states are a particular type of Gaussian states which are of fundamental interest to this work. They are defined as states which present a lower than vacuum uncertainty in one quadrature of the field, at the expense of an increment in the conjugate quadrature. From a quantum information perspective, squeezed states allow for deterministic and unconditional generation of continuous variable entanglement [44]. Thus, they are central to quantum information protocols such as quantum teleportation [44, 118] and quantum computation [37, 119]. Interestingly as well, reduced noise levels have made squeezed light fundamental to important breakthroughs in metrology [120, 121]. The characteristic photon correlations of squeezing may occur within a single mode of the field or between distinct modes, thus defining single- and two-mode squeezed states, on which we will focus in the following sections.

### 2.3.1 Single-mode squeezing

A single-mode squeezed state must satisfy $\langle(\Delta X(\phi))^2\rangle \leq \langle(\Delta X)^2\rangle_{\mathrm{vacuum}}$ for some rotation angle $\phi$. We define the unitary squeezing operator as

$$S(\xi) = \exp\left[\frac{1}{2}\left(\xi^* a^2 - \xi (a^\dagger)^2\right)\right] \ , \tag{2.30}$$

with $\xi = |\xi| \mathrm{e}^{\mathrm{i}\theta}$ the squeezing parameter, which transforms the bosonic operators and the quadratures as

$$S^\dagger a S = a \cosh|\xi| - \mathrm{e}^{\mathrm{i}\theta} a^\dagger \sinh|\xi| \ , \tag{2.31a}$$

$$S^\dagger X(\phi) S = X(\phi)\cosh|\xi| - X(\theta - \phi)\sinh|\xi| \ . \tag{2.31b}$$

Thus, the quadratures $X(\theta/2)$ and $X(\theta/2 + \pi/2)$ are contracted and expanded respectively by a factor $\mathrm{e}^{\mp|\xi|}$ due to the action of $S$. The squeezed vacuum state is obtained applying the

squeezing operator on vacuum, $|\xi\rangle = S(\xi)|0\rangle$, which represents a field with zero mean value $\langle X(\phi)\rangle = 0$, and a phase-dependent variance

$$\left\langle (\Delta X(\phi))^2 \right\rangle = \frac{\cosh 2|\xi| - \sinh 2|\xi| \cos(\theta - 2\phi)}{4} \ . \tag{2.32}$$

Minimal variance is obtained in the maximally squeezed quadrature $X(\theta/2)$, for which $\langle (\Delta X(\theta/2))^2 \rangle = \mathrm{e}^{-2|\xi|}/4$. In the conjugate quadrature $\langle (\Delta X(\theta/2 + \pi/2))^2 \rangle = \mathrm{e}^{+2|\xi|}/4$, thus $|\xi\rangle$ is a minimal uncertainty state in terms of the Heisenberg-like relation in Eq. (2.8). Squeezing with non-zero mean value is obtained operating squeezed vacuum with the displacement operator, which does not modify the uncertainty of the quadratures. We focus on vacuum squeezing during our work.

The off diagonal elements of the correlation matrix, are determined by

$$\frac{1}{2} \left\langle [\Delta X(\phi) \Delta X(\phi + \pi/2)]_+ \right\rangle = -\frac{\sinh 2|\xi| \sin(\theta - 2\phi)}{4} \ , \tag{2.33}$$

while the diagonal ones are represented in Eq. (2.32). The correlation matrix is

$$V = \frac{\cosh 2|\xi|}{4} \begin{pmatrix} 1 & 0 \\ 0 & 1 \end{pmatrix} - \frac{\sinh 2|\xi|}{4} \begin{pmatrix} \cos\theta & \sin\theta \\ \sin\theta & -\cos\theta \end{pmatrix} \ . \tag{2.34}$$

For $\theta = 0$, we obtain a diagonal correlation matrix $V_0 = \mathrm{diag}\left(\mathrm{e}^{-2|\xi|}/4, \mathrm{e}^{+2|\xi|}/4\right)$, therefore the Wigner function is a vertically aligned ellipse, as shown in Fig. 2.2-(a). For an arbitrary $\theta$, Eq. (2.32) and (2.33) show that the diagonal form of $V$ may be recovered upon a rotation of the phase space in $\theta/2$. Thus the Wigner function for an arbitrary $\theta$ corresponds to the $\theta = 0$ ellipse rotated counterclockwise in $\theta/2$, as shown in Fig. 2.2-(b).

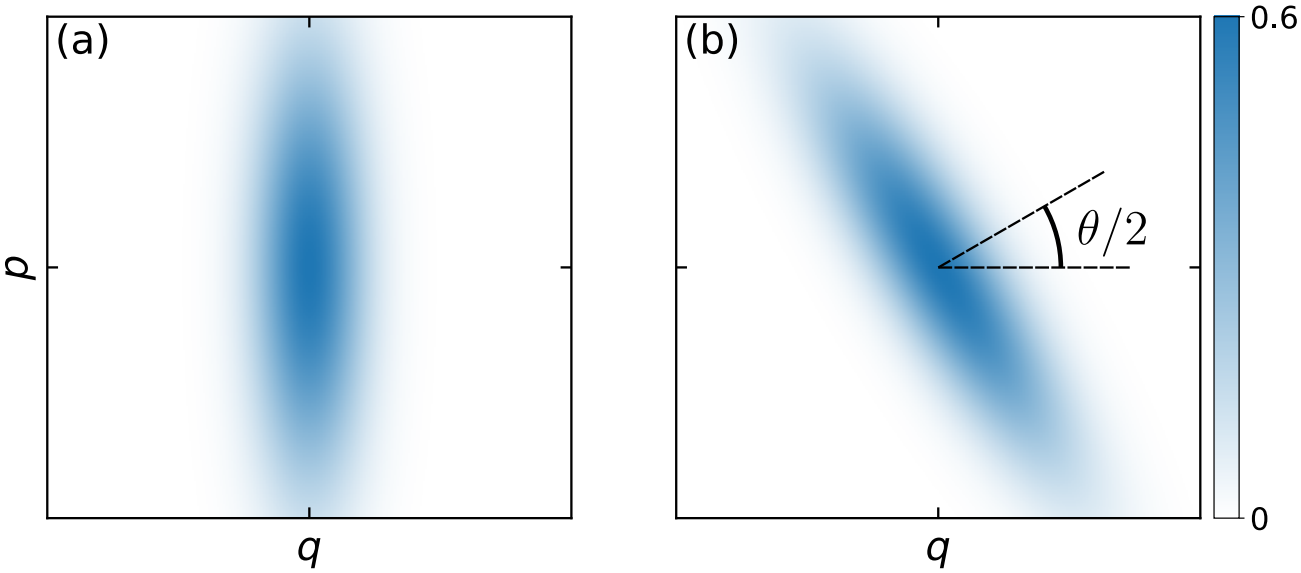


FIGURE 2.2: Wigner function for single-mode squeezed states, with $|\xi| = 0.7$ and **(a)** $\theta = 0$, and **(b)** $\theta = \pi/3$. Squeezed states are represented by a Gaussian distribution with reduced variance along the squeezed quadrature, which is rotated in $\theta/2$ with respect to $X_1$.

The degree of squeezing of a given state is measured comparing the noise in its maximally squeezed quadrature to that of vacuum by means of a standard decibel formula

$$S\left[\mathrm{d}B\right] = \min_{\phi} 10 \log_{10} \left( \frac{\langle (\Delta X(\phi))^2 \rangle}{\langle (\Delta X)^2 \rangle_{\mathrm{vacuum}}} \right) \ . \tag{2.35}$$

Squeezing at a given quadrature is measured in the same way, but evaluating for the corresponding rotation angle $\phi$.

Despite the zero coherent amplitude, squeezed vacuum presents a non-zero mean photon number $\langle \hat{n}a \rangle = \sinh^2 |\xi|$. Expansion of $|\xi\rangle$ in the Fock basis reads [113]

$$|\xi\rangle = \sum_{k=0}^{\infty} (-1)^k \frac{\sqrt{(2k)!}}{2^k k!} \frac{\tanh^k |\xi|}{\sqrt{\cosh |\xi|}} \mathrm{e}^{\mathrm{i}\theta k} |2k\rangle \ , \tag{2.36}$$

where we observe not only that squeezed vacuum is composed by non-zero Fock states, but also that only pair photon numbers take part. This is present in the squeezing operator, which represents pairwise creation and annihilation of photons in the optic mode.

The reduced variance of squeezed states makes them a natural candidate for applications in metrology [122, 123]. Injection of squeezed vaccum states in non utilized ports of interferometers, replacing plain vacuum fluctuations for squeezed vacuum, has proven to enhance sensitivity [120, 124–127]. Probably the most remarkable of such applications is the use of squeezed states of light in the Laser Interferometer Gravitational-Wave Observatory (LIGO) [121, 128]. Other related applications of single-mode squeezed states include quantum sensing [129] and quantum imaging [130].

### 2.3.2 Two-mode squeezing

The squeezing operator in Eq. (2.30) may be extended to generate two-mode squeezing by the pairwise creation and annihilation of photons in two distinct modes of the field $a$ and $b$, via the two-mode squeezing operator

$$S_{a,b} = \exp\left[ \xi^* ab - \xi a^\dagger b^\dagger \right] \ . \tag{2.37}$$

The two-mode squeezed vacuum state $|\xi\rangle_{a,b} = S_{a,b}(\xi)|0\rangle$ is expanded in the Fock basis as [113]

$$|\xi\rangle_{a,b} = \sum_{k=0}^{\infty} (-1)^k \frac{\tanh^k |\xi|}{\cosh |\xi|} \mathrm{e}^{\mathrm{i}\theta k} |k\rangle_a \otimes |k\rangle_b \ , \tag{2.38}$$

where we confirm that only states with identical photon number in both modes are represented. We have claimed that squeezed states are a source of continuous variable entanglement, which now appears evident as $|\xi\rangle_{a,b}$ cannot be written as a simple direct product state.

The action of the two-mode squeezing operator on the bosonic operators is

$$S_{a,b}^\dagger a S_{a,b} = a \cosh |\xi| - \mathrm{e}^{\mathrm{i}\theta} b^\dagger \sinh |\xi| \tag{2.39a}$$

$$S_{a,b}^\dagger b S_{a,b} = b \cosh |\xi| - \mathrm{e}^{\mathrm{i}\theta} a^\dagger \sinh |\xi| \ . \tag{2.39b}$$

These relations are used to obtain the mean value of the quadratures, which is zero just as for vacuum single-mode squeezing, and the correlation matrix, whose elements are represented in the following equations:

$$\left\langle (\Delta X^{(a)}(\phi))^2 \right\rangle = \left\langle (\Delta X^{(b)}(\phi))^2 \right\rangle = \frac{\cosh 2|\xi|}{4} \tag{2.40a}$$

$$\left\langle \Delta X^{(a)}(\phi) \Delta X^{(b)}(\phi) \right\rangle = -\frac{\sinh 2|\xi|}{4} \cos(\theta - 2\phi) \tag{2.40b}$$

$$\frac{1}{2} \left\langle \left[ \Delta X^{(a)}(\phi), \Delta X^{(a)}(\phi + \pi/2) \right]_+ \right\rangle = \frac{1}{2} \left\langle \left[ \Delta X^{(b)}(\phi), \Delta X^{(b)}(\phi + \pi/2) \right]_+ \right\rangle = 0 \tag{2.40c}$$

$$\left\langle \Delta X^{(a)}(\phi) \Delta X^{(b)}(\phi + \pi/2) \right\rangle = \left\langle \Delta X^{(a)}(\phi + \pi/2) \Delta X^{(b)}(\phi) \right\rangle = -\frac{\sinh 2|\xi|}{4} \sin(\theta - 2\phi) \ . \tag{2.40d}$$

For $\theta = 0$ the correlation matrix is

$$V_0 = \frac{1}{4} \begin{pmatrix} \cosh 2|\xi| & 0 & -\sinh 2|\xi| & 0 \\ 0 & \cosh 2|\xi| & 0 & \sinh 2|\xi| \\ -\sinh 2|\xi| & 0 & \cosh 2|\xi| & 0 \\ 0 & \sinh 2|\xi| & 0 & \cosh 2|\xi| \end{pmatrix} \ , \tag{2.41}$$

while for an arbitrary phase $\theta$, the diagonal form of the matrix is obtained rotating the phase space in $\theta/2$. Thus the general expression for the correlation matrix is $V = \mathcal{R}(\theta/2) V_0 \mathcal{R}^\dagger(\theta/2)$ with $\mathcal{R}(\theta/2) = \mathrm{diag}(R(\theta/2), R(\theta/2))$, and $R(\theta/2)$ the $2 \times 2$ rotation matrix.

Squeezed states were defined by their lower than vacuum uncertainty, however it is not evident that two-mode squeezing satisfies this property. The uncertainty in the single-mode quadratures, given by Eq. (2.40a), yields $\left\langle (\Delta X^{(\mu)}(\phi))^2 \right\rangle \geq \langle (\Delta X)^2 \rangle_{\text{vacuum}}$ $\forall \phi$, with $\mu = a, b$. Furthermore, the correlation matrix in each individual mode is $V_\mu = \cosh 2|\xi| \mathrm{I}/4$, which corresponds to that of a thermal state with $\bar{n} = \sinh^2 |\xi|$, known not to be a minimal uncertainty state. We define the two-mode $\phi$ rotated quadrature $X^{(a,b)}(\phi)$ as a superposition of the quadratures of the individual modes

$$X^{(a,b)}(\phi) = \frac{X^{(a)}(\phi) + X^{(b)}(\phi)}{\sqrt{2}} \ , \tag{2.42}$$

obtaining the phase-dependent uncertainty

$$\left\langle (\Delta X^{(a,b)}(\phi))^2 \right\rangle = \frac{\cosh 2|\xi| - \sinh 2|\xi| \cos(\theta - 2\phi)}{4} \ . \tag{2.43}$$

Just as for single-mode squeezing, the maximally squeezed quadrature is $\phi = \theta/2$, for which $\left\langle (\Delta X^{(a,b)}(\theta/2))^2 \right\rangle = \mathrm{e}^{-2|\xi|}/4$. Quantum phenomena emerging from two-mode squeezing occurs due to correlations between the modes, and cannot be observed when only viewing an individual mode.

We now address quantitatively the emergence of entanglement in two-mode squeezing. The Wigner function for $\theta = 0$ reads

$$W_{a,b}(\chi) = \frac{4}{\pi^2} \exp\left[ -\mathrm{e}^{2|\xi|} \left( (q_a + q_b)^2 + (p_a - p_b)^2 \right) - \mathrm{e}^{-2|\xi|} \left( (q_a - q_b)^2 + (p_a + p_b)^2 \right) \right] \ . \tag{2.44}$$

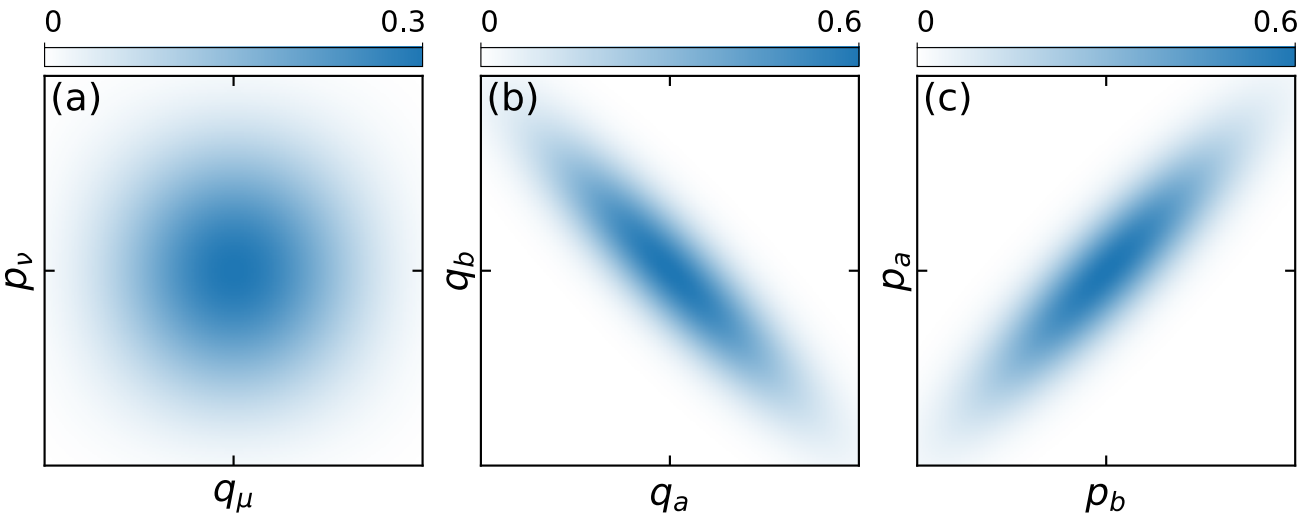


FIGURE 2.3: Marginal Wigner distributions for two-mode squeezed vacuum, with $\xi = 0.7$. **(a)** The marginal distributions for $q_\mu$ and $p_\nu$ (with $\mu, \nu = a, b$) take the form of thermal states, showing no correlations between these variables. **(b)** and **(c)** Correlations are observed in superpositions of the single-mode quadratures, as panel (b) shows squeezing in the two-mode quadrature $X_{a,b}(\phi = 0)$, and panel (c) shows anti-squeezing in the orthogonal two-mode quadrature.

The marginal distributions are shown in Fig. 2.3, from which it is evident that correlations are only observed in the superposition of the single-mode quadratures. Taking the infinite squeezing limit $|\xi| \to \infty$, which is unphysical as such a state would require infinite energy, but represents a perfectly correlated state, the Wigner function approaches $W_{a,b} \propto \delta(q_a + q_b)\delta(p_a - p_b)$. In this limit two-mode squeezed vacuum corresponds to an optic EPR state [131]. Measurement of quadrature $X_0^{(a)}$ ($X_1^{(a)}$) at mode $a$ sets the state of the field at mode $b$ as the eigenstate $|-q_b\rangle$ of $X_0^{(b)}$ (eigenstate $|p_b\rangle$ of $X_1^{(b)}$), revealing the entangled nature of the state. For an arbitrary $\theta$ the Wigner function takes the same form as Eq. (2.44) with the rotation $q_\mu \to q_\mu \cos\theta/2 + p_\mu \sin\theta/2$, and $p_\mu \to p_\mu \cos\theta/2 - q_\mu \sin\theta/2$, with $\mu = a$, $b$. The same analysis can be done in terms of the quadratures $X(\theta/2)$ and $X(\theta/2 + \pi/2)$, thus the phase of the squeezing sets the entangled variables of the system.

In terms of the Peres-Horodecki entanglement criterion, presented in section 2.2.3, the minimum eigenvalue for $\tilde{V} - \Lambda$ is $\lambda_{\min} = (e^{-2|\xi|} - 1)/4$, independent of $\theta$. The magnitude of entanglement is independent of the phase of the squeezing parameter, and monotonically increases with the magnitude of squeezing, converging to $\lambda_{\min} \to -1/4$ in the infinite squeezing limit.

# Chapter 3

# Quadrature protection of squeezed states in a one-dimensional photonic topological insulator

This chapter presents the main research carried on the topic of topological protection of quantum light. We study the propagation of squeezed states in a topological one-dimensional waveguide array, when exciting the topologically protected state with squeezed light. We focus on the behavior of quantum properties such as squeezing and entanglement, concluding on the topological protection of squeezing, where the phase of the squeezed quadrature is robustly preserved as the system evolves. We finally show how this topological protection can be beneficial to quantum information protocols.

What follows is an adapted version of [51], written by the author of this thesis, Gabriel O'Ryan Pérez, Carla Hermann-Avigliano, and Luis E. F. Foa Torres.

## 3.1 Introduction

As a recent, yet promising research area, quantum topological photonics —namely the study and manipulation of quantum light in topological photonic systems— has allowed for topologically robust lasers [132, 133] and amplifiers [134, 135], and is positioned as an alternative for providing robust transport of quantum information [40]. Successful coupling between photons and topological degrees of freedom has been reported, not only in the single-particle level, but also for multi-photon states [48, 49, 136–143]. Remarkable results show topological protection of bi-photon dynamics, granting robustness to quantum correlations against structural disorder [49, 139], and quantum interference of topological states [138]. Topological protection of entanglement has been experimentally reported as well [41, 42, 50, 144], demonstrating the potential of quantum topological photonics for quantum information processing [40].

Research in this area has been focused on Fock-like states, while the interplay between topology and squeezed light [145], which serves as a fundamental building block for continuous variable

quantum information [44, 146, 147], remains less explored. Lower than vacuum noise levels have made squeezed light fundamental to breakthroughs in metrology [120, 121], while from a quantum information perspective, two-mode squeezing stand as a deterministic and unconditional source of entanglement [44]. Several continuous variable quantum information protocols, such as quantum teleportation [118, 148] and quantum computation [37, 119], rely on efficient transmission and manipulation of squeezed states. However, the correlated nature of these states makes them sensitive fabrication imperfections in optic systems, mainly through phase mismatching and phase diffusion processes, as well as optical losses [149–152]. It is therefore of high interest to elucidate the effect of a lattices topology on squeezed light, in the search for topological protection of squeezing.

Here we present a thorough report on the propagation of squeezed light in a topological photonic lattice, and the effects of topology on quantum features of light[1]. We study the behavior of photon statistics, squeezing and entanglement in a one-dimensional SSH waveguide array when exciting its topologically protected edge state with quadrature squeezed light, employing analytic and numerical techniques. Our focus is to determine the role that the lattices topology plays in this phenomena, establishing an interplay between lattice symmetries and quantum correlations. To this goal we benchmark our results with those of an impurity induced, topologically trivial localized state, and study their response to disorder. A first conclusion that we extract is that quantum properties inherit the localization of the edge state and therefore follow its fate when disorder is introduced. But since mere localization may be generated and preserved under topologically trivial circumstances, one may wonder if any other more remarkable consequence of topology or *topological advantage* exists. Interestingly, we find that the phase of the squeezed quadrature is preserved in the topological state, providing an advantage for propagation of squeezed light in photonic lattices that may not be replicated by other topologically trivial localized states.

The structure of this chapter is as follows: In section 3.2 we briefly recall the SSH system and its topological properties, introducing the trivial lattice used for comparison as well. We then study the system when the edge state is excited with single-mode squeezed light under two different scenarios. In section 3.3.1 we apply the squeezing operator on the localized eigenmode, studying the distribution of squeezing across the lattice. In section 3.3.2, pursuing a more feasible method of squeezing the edge state, we inject single-mode squeezed light to the edge waveguide and study its propagation. During section 3.4 we study the propagation of two-mode squeezing along the lattices. Finally, in section 3.5 we present an application of our results in a quantum teleportation protocol, where the entanglement resource is topologically protected, which serves as a proof of concept for the relevance of topological protection of quantum information upon practical implementations. The chapter concludes with final remarks and perspectives in section 3.6.

## 3.2 The lattices

Throughout this work we consider an SSH waveguide array, which is described by a dimerized one-dimensional chain of identical modes with propagation constant $\beta$, and alternating hopping

[1] After submission of [51], a related study was reported [153].

amplitudes $u$ and $v$, given by the hamiltonian

$$\hat{H}_{\text{top}} = \sum_n \beta a_{2n}^\dagger a_{2n} + \beta a_{2n+1}^\dagger a_{2n+1} + \left( u a_{2n}^\dagger a_{2n+1} + v a_{2n+1}^\dagger a_{2n+2} + \text{h.c.} \right) \ , \tag{3.1}$$

where $a_n$ is the bosonic annihilation operator at mode $n$. The system is formed by two sublattices, even and odd modes, with a unit cell containing sites $a_{2n}$ and $a_{2n+1}$. We take $u$ and $v$ of the same sign. This choice is physically motivated as the hoppings are typically determined by the overlap of the evanescent tails of the modes located at each waveguide [101]. As reviewed in section 1.2, the system presents a bulk bandgap of $|u - v|$; however, exponentially localized states with a propagation constant equal to that of the bare waveguides and perfect sublattice polarization appear at the edge of a finite lattice terminated in a weak coupling. These states are topologically protected by chiral symmetry, which is broken by onsite terms differing on each sublattice or couplings between sites of the same sublattice for example. Therefore, introducing disorder to the nearest neighbour hoppings preserves the propagation constant of the edge state and its sublattice polarization. On the other hand, for symmetry breaking onsite disorder the topological phase of the lattice is destroyed and these properties fluctuate. We note as well that perfect sublattice polarization can only arise for a semi-infinite lattice as in the finite case there is always a small coupling between states at opposite edges.

For a semi-infinite SSH lattice, as depicted in Fig. 3.1-(a), with $u < v$, the topological state has annihilation operator

$$A_{\text{top}} = \sqrt{1 - \alpha^2} \sum_{n \geq 0} (-\alpha)^n a_{2n} \ , \tag{3.2}$$

where $\alpha = u/v$ and the absence of odd modes in $A_{\text{top}}$ reflects sublattice polarization. The amplitude of the topological state at each waveguide is shown in Fig. 3.1-(b).

To benchmark our results we need a reference system. Since we are interested in isolating the effect of topology, a natural candidate is a system hosting a topologically trivial edge state. This motivates us to also consider a non-dimerized one-dimensional chain of identical modes with an onsite impurity $\varepsilon_0$, which induces an exponentially localized mode with no topological protection. The hamiltonian of the semi-infinite trivial lattice, with the impurity located at its edge is

$$\hat{H}_{\text{trivial}} = \varepsilon_0 a_0^\dagger a_0 + \sum_{n \geq 0} \beta a_n^\dagger a_n + \left( w a_n^\dagger a_n + \text{h.c.} \right) \ , \tag{3.3}$$

with $w$ the hopping amplitude between neighboring waveguides. The localized state of this system is given by its annihilation operator

$$\begin{aligned} A_{\text{trivial}} &= \sqrt{1 - \left( \frac{w}{\varepsilon_0} \right)^2} \sum_{n \geq 0} \left( \frac{w}{\varepsilon_0} \right)^n a_n \\ &= \sqrt{1 - \alpha^2} \sum_{n \geq 0} (-\alpha)^n a_n \ , \end{aligned} \tag{3.4}$$

where we have chosen $\varepsilon_0 = -w/\alpha$ so both localized states present the same spatial distribution, with exception of sublattice polarization. We also set $w = v\alpha/(1 - \alpha)$ so both states present the same spectral separation to the bulk bands. The semi-infinite topologically trivial lattice

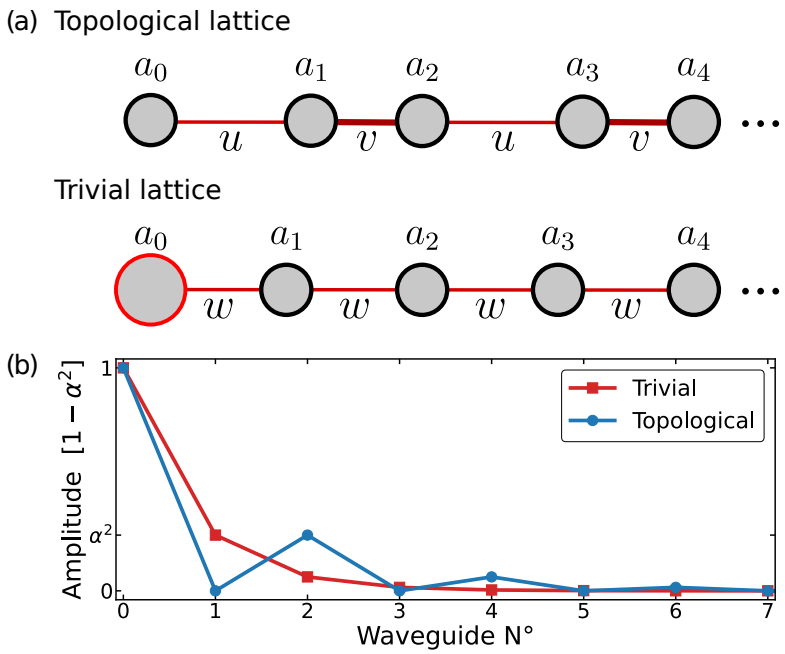


FIGURE 3.1: Topological and topologically trivial systems (without disorder) considered throughout our work. The latter is used to benchmark our results for the topological system. **(a)** Scheme of the lattices. Sites are represented by grey circles and hoppings by connecting lines. **(b)** Probability distribution of the localized eigenstate hosted by each lattice. The states show the same overall exponential decay when adjusting for the different lattice constants, and differ by the sublattice polarization of the topological state.

is depicted in Fig. 3.1-(a), and the amplitude of its edge state in each waveguide is shown in Fig. 3.1-(b). In contrast to the topological state, the trivial one does not present any symmetry protected properties, so its propagation constant and spatial distribution will vary upon any type of disorder present in the lattice.

## 3.3 Single-mode squeezing in a topological state

We now study the behavior of single-mode squeezed light coupled to the topological state under two perspectives: In section 3.3.1 we consider the state of the system $|\psi\rangle$ as single-mode squeezed vacuum of the eigenmode, that is $|\psi\rangle = S_{A_{\text{top}}}(\xi)|0\rangle$, with $S_a(\xi)$ the single-mode squeezing operator of mode $a$. Experimentally it would be very challenging to squeeze a collective mode of the lattice; nevertheless, this scenario provides insight on how quantum properties present themselves when exciting solely the topological state. In section 3.3.2 we turn to a more feasible scenario, where we excite only the edge waveguide with single-mode squeezed light and study its propagation. In both cases we study the distribution of one- and two-mode squeezing across the lattice, and their response to disorder, comparing with the topologically trivial state.

When introducing disorder, we construct a lattice with hopping (onsite) disorder $d$ by sampling each hopping (onsite) term from a uniform distribution centered at the pristine value of the parameter. The results presented for disordered systems correspond to the average over 50 mean values, each of them obtained after averaging the results for six different (a sextet) random

realizations of the disordered systems.

### 3.3.1 Squeezing the eigenstate

We consider semi-infinite lattices, and express their edge states as a linear combination of the operators at each waveguide, $A = \sum c_n a_n$. For the pristine systems the coefficients $c_n$ are given by Eq. (3.2) or (3.4) depending on the situation, while for disordered systems they are obtained numerically. For the state $|\psi\rangle = S_A(\xi)|0\rangle$ we find the following values for squeezing

$$S_n = 10 \log_{10} \left(1 - 2|c_n|^2 \mathrm{e}^{-|\xi|} \sinh |\xi|\right) \ , \tag{3.5a}$$

$$S_{n,m} = 10 \log_{10} \left(1 - |c_n + c_m|^2 \mathrm{e}^{-|\xi| \sinh |\xi|}\right) \ , \tag{3.5b}$$

with $S_n$ ($S_{n,m}$) the one-mode (two-mode) squeezing measurement in decibels at waveguide $a_n$ (between waveguides $a_n$ and $a_m$).

Our results in Eq. (3.5a) and (3.5b), shown in Fig. 3.2 as disorder is introduced, indicate that squeezing decays when distancing from the edge following the exponential decay of the eigenstates. For the pristine lattices, because the topological state at even waveguides shows the same spatial distribution than the impurity induced state, the measured quantities are identical in both systems, but the values obtained at site $a_{2n}$ of the topological lattice are obtained at site $a_n$ of the trivial one. Furthermore, Eq. (3.5b) reveals that two-mode squeezing is sensitive to the phase relation between the individual modes, generating higher squeezing between in-phase modes, being $S_{0,4}$ ($S_{0,2}$) the highest and $S_{0,2}$ ($S_{0,1}$) the lowest for the topological (trivial) state, as shown in Fig. 3.2, bottom row. For the topological lattice, the absence of one-mode squeezing at odd waveguides reflects sublattice polarization of the state, which is broken when introducing onsite disorder, as occurs in Fig. 3.2, top right panel. We observe as well that for high disorder values the states partially delocalize, which is reflected in a decreasing magnitude of one-mode squeezing, while they also show larger statistical fluctuations, represented by wider confidence intervals. Until now, the propagation constant does not seem to take part in the behavior of the systems. In order to observe its effect we must study the propagation of the states.

### 3.3.2 Propagation of single-mode squeezing

Since squeezing a collective mode of the system might be experimentally very challenging, we now consider a more feasible state of the field generated by exciting only the edge waveguide with single-mode squeezed vacuum —that is $|\psi(z=0)\rangle = S_{a_0}|0\rangle$— and study its evolution along the propagation axis $z$. We work in a rotated frame, where the maximally squeezed quadrature of the edge waveguide of the pristine lattices corresponds to $X(\phi = 0)$ along the entire propagation. We report mean photon number at each quadrature, squeezing at the orthogonal quadratures $X_1 = X(0)$ and $X_2 = X(\pi/2)$, and maximal squeezing at any rotated quadrature. To maintain this system as simple as possible, we consider finite lattices of 15 waveguides each.

The propagation of the excitation across the pristine lattices is shown in Fig. 3.3, top row, depicting the mean photon number in each waveguide as both systems evolve. Part of the excitation remains permanently localized near the edge due to coupling with the localized states, generating a distribution of squeezing qualitatively equal to the one presented in section 3.3.1:

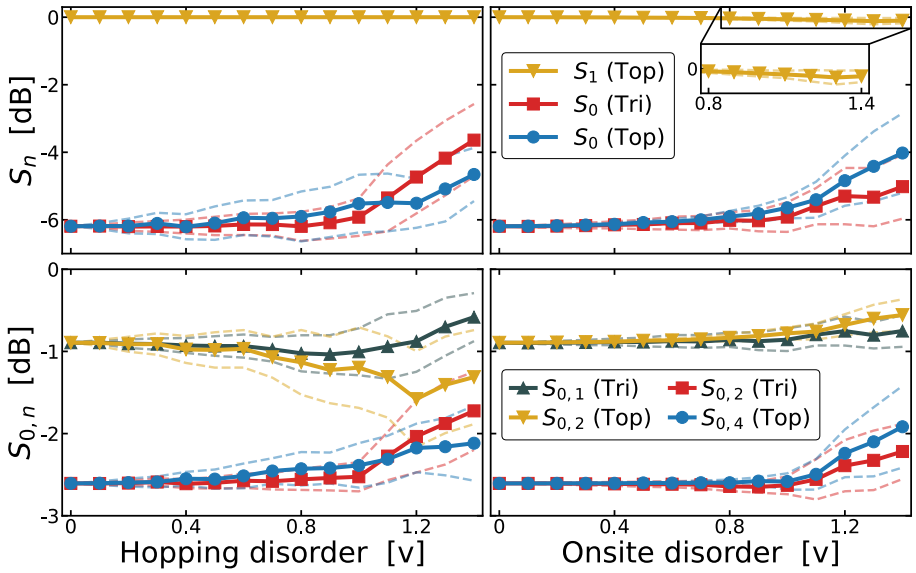


FIGURE 3.2: Distribution of squeezing across the lattice when squeezing the localized eigenstates ($\alpha = 0.3$, $\xi = 0.9$). Solid lines with markers show the statistical average value over disordered systems, and dashed lines represent the confidence interval associated with the standard deviation. Top (bottom) row shows one-mode (two-mode) squeezing. The waveguides at which the observations are made are shown in the legend, with Top (Tri) indicating topological (trivial) state. Zero squeezing at $S_1$ (Top) reflects sublattice polarization of the topological state, which is broken when introducing onsite disorder as shown in the top right panel. The bottom panels show that two-mode squeezing is sensitive to the phase relation between the modes, obtaining higher squeezing between waveguides $a_0$ and $a_4$ ($a_2$) for the topological (trivial) state.

Photon number and one-mode squeezing decay while distancing from the edge, respecting sublattice polarization in the topological lattice. Maximum two-mode squeezing is obtained between waveguides $a_0$ and $a_4$ ($a_2$) in the topological (trivial) state (see also Fig. 3.9 in appendix 3.7.A). These results show that when injecting one-mode squeezing to the edge waveguide, not only does the excitation remain localized, but the quantum properties of the field inherit the shape of the edge state. This is particularly clear when analyzing two-mode squeezing, which proves to be sensitive to the phase relation between the individual modes. We also observe that part of the excitation does not couple to the edge state but transports across the lattice, which is explained by the non-perfect overlap between the edge state and the zero-th waveguide.

When introducing disorder we do not observe a significant change in the mean photon number of the localized portion of the excitation which is coupled to the edge state, for neither type of disorder. On the other hand, as shown in Fig. 3.3, transport of the decoupled excitation is degraded due to Anderson localization of the extended states. In the topological lattice this causes a persistent non-zero photon number at odd waveguides, even for symmetry preserving hopping disorder.

The most remarkable consequences of topological protection, or lack of it, are observed when analyzing one-mode squeezing at the edge waveguide, as shown in Fig. 3.4-(a). We observe that maximal squeezing in the pristine lattices, which is always obtained in quadrature $X_1$, has an

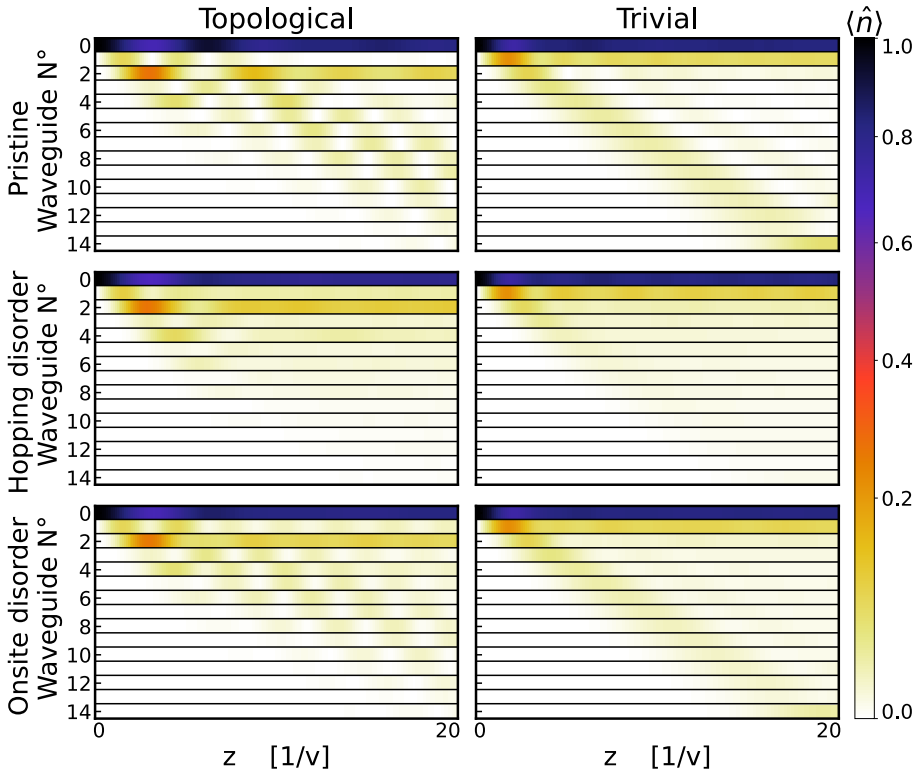


FIGURE 3.3: Photon number $\langle \hat{n} \rangle$ in units relative to the initial state ($\alpha = 0.3$, $\xi = 0.9$). Top, middle and bottom row correspond to pristine, hopping disordered ($\mathrm{d} = 0.6v$) and onsite disordered ($\mathrm{d} = 0.6v$) lattices respectively, while left and right columns correspond to the topological and trivial systems respectively. Part of the excitation couples to the edge state and remains localized, reflected by a persistent high photon number in waveguide zero. The other part of the excitation transports across the pristine lattices towards the opposite border. Disorder induced Anderson localization obstructs transport across the bulk of the lattices.

approximately equal value in the topological and trivial state. The role of topology is revealed when introducing hopping disorder. Maximal squeezing appears to be insensitive to disorder; however, a drastically different behavior is observed for squeezing at quadratures $X_1$ and $X_2$. Because hopping disorder preserves chiral symmetry, the propagation constant of the topological state remains equal to that of the bare waveguides, therefore its maximally squeezed quadrature continues to be $X_1$ along the entire propagation (Fig. 3.4-(b)–(d)). In contrast, random disorder generates fluctuations in the propagation constant of the trivial state, rotating the maximally squeezed quadrature. Even though the behavior of maximal squeezing remains similar to that of the pristine lattice, the rotation angle of the squeezed quadrature differs between different random realizations, thus when averaging over them at a fixed quadrature, coherence of the quantum state is lost and no squeezing is obtained (Fig. 3.4-(e)–(g)).

This discussion is consistent with the results for the onsite disordered lattices. Just as occurred for hopping disorder, the behavior of maximal squeezing is similar to the pristine case. Nevertheless, introduction of onsite disorder breaks chiral symmetry in the SSH lattice, therefore its edge state looses topological protection, and its propagation constant ceases to be topologically

locked. The fluctuations in the propagation constant between different random realizations causes different rotation angles of their maximally squeezed quadratures, obtaining no squeezing when averaging over them at a fixed quadrature. These results show that when propagating squeezed light through a localized state in a photonic lattice, topological protection of the state allows for phase coherence in the squeezed quadrature.

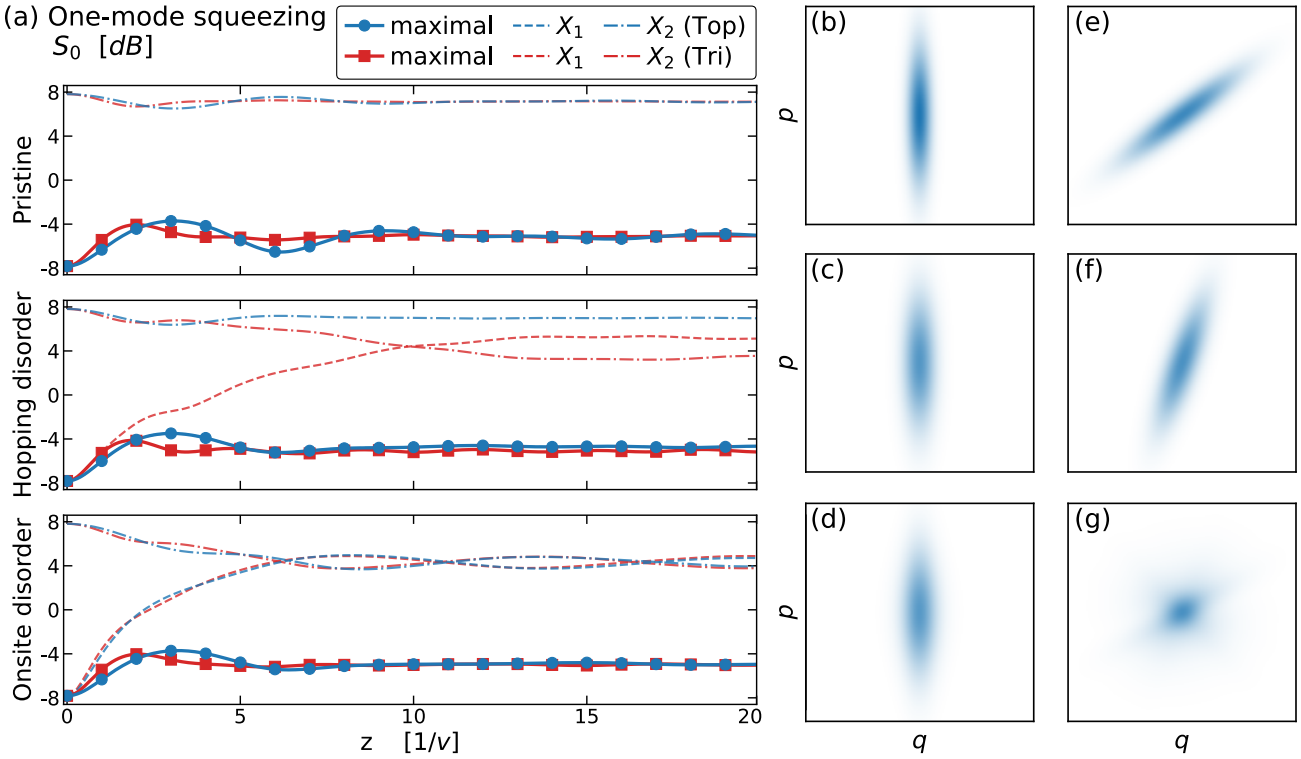


FIGURE 3.4: Single-mode squeezing at waveguide zero ($\alpha = 0.3$, $\xi = 0.9$). **(a)** Solid blue (red) curves with circular (square) marker show squeezing at the maximally squeezed quadrature for the topological (trivial) state. Dashed (dash-dotted) curves show squeezing at quadrature $X_1$ ($X_2$). The maximally squeezed quadrature of the pristine systems is always $X_1$, as the dashed curves overlaps with the solid ones. The maximally squeezed quadrature of the topological state remains $X_1$ if chiral symmetry is preserved (hopping disorder), but rotates if it is broken (onsite disorder), whereas that of the trivial state rotates upon any form of disorder. Fluctuations in the rotation angle of the squeezed quadrature results in no average squeezing at $X_1$ and $X_2$. Panels (b)–(g) show the Wigner function at waveguide zero. **(b)** Input single-mode squeezed state, squeezed in $X_1$. **(c)** One realization of the hopping disordered topological system at $z = 10v^{-1}$, which remains squeezed in $X_1$. **(d)** Average Wigner function of the hopping disordered topological system at $z = 10v^{-1}$, showing non-zero squeezing as all realizations remain squeezed in $X_1$ due to topological protection. **(e)** and **(f)** Two realizations of the hopping disordered trivial system at $z = 10v^{-1}$, which are squeezed at different rotated quadratures. **(g)** Average Wigner function of the hopping disordered trivial state at $z = 10v^{-1}$, showing zero average squeezing as the squeezed quadrature differs between different realizations.

## 3.4 Two-mode squeezing of topological states

Having elucidated the role of topology in the propagation of single-mode squeezed light, we now study two-mode squeezing coupled to respective localized states. In contrast to single-mode squeezing, now the main quantum correlations occur between different modes, giving rise to entanglement. As seen in the previous section, the main consequence of the lattices topology is protection of the squeezed quadrature. We know as well that the phase of the squeezing parameter does not affect the magnitude of entanglement in the system, but does determine the entangled variables. With this in mind, we now study the propagation of two-mode squeezed light in the topological SSH lattice.

We consider two independent SSH lattices of 15 waveguides each —which we label as lattices A and B— each one hosting a topologically protected edge state, and study the propagation of two-mode squeezing along the system. For comparison, we also consider topologically trivial lattices hosting impurity induced edge states. The initial state of the field is given by the two-mode squeezed vacuum state between the edge waveguide of both lattices, that is $|\psi(z=0)\rangle = S_{a_0,b_0}|0\rangle$. We explore the response of the systems to hopping and onsite disorder, while reporting two-mode squeezing and entanglement between both edge waveguides.

Fig. 3.5, left panel, shows the evolution of two-mode squeezing along the lattices, whose results agree with those of section 3.3: Maximal squeezing measured in both systems has an approximately equal value along the propagation direction, which is neither sensitive to topology nor disorder. For the topological system, the maximally squeezed quadrature is $X_1$ as long as chiral symmetry is preserved, because the propagation constant of the edge state is topologically locked. In contrast, if the symmetry is broken by onsite disorder, squeezing measured at quadratures $X_1$ and $X_2$ averages to zero over the random realizations of the system due to fluctuations in the rotation angle of the maximally squeezed quadrature. On the other hand, as the impurity induced edge state does not present any preserved properties, the squeezing values at fixed quadratures are highly fragile against both types of disorder.

The behavior of entanglement in the systems, portrayed in Fig. 3.5, right panel, is qualitatively similar to that of maximal two-mode squeezing: it takes an approximately constant value along the propagation axis, and does not appear to be sensitive to disorder. From this perspective, the results indicate that the total amount of quantum correlations present in the system are independent of the topology of the involved edge states. However, they must be interpreted alongside the information provided by squeezing at the non-rotated quadratures, and the characterization of the entangled variables in a two-mode squeezed state. Despite the fact that the amount of entanglement is independent of the topology of the edge state, its topological protection allows to control the maximally entangled variables, protecting them from any symmetry preserving form of disorder.

## 3.5 Quantum teleportation employing a topological lattice

In this section we demonstrate the previously highlighted consequences of topological protection of squeezing. For this we implement quantum teleportation of a single-photon, where the two-mode squeezed states studied in section 3.4 serve as the shared entanglement resource. As we

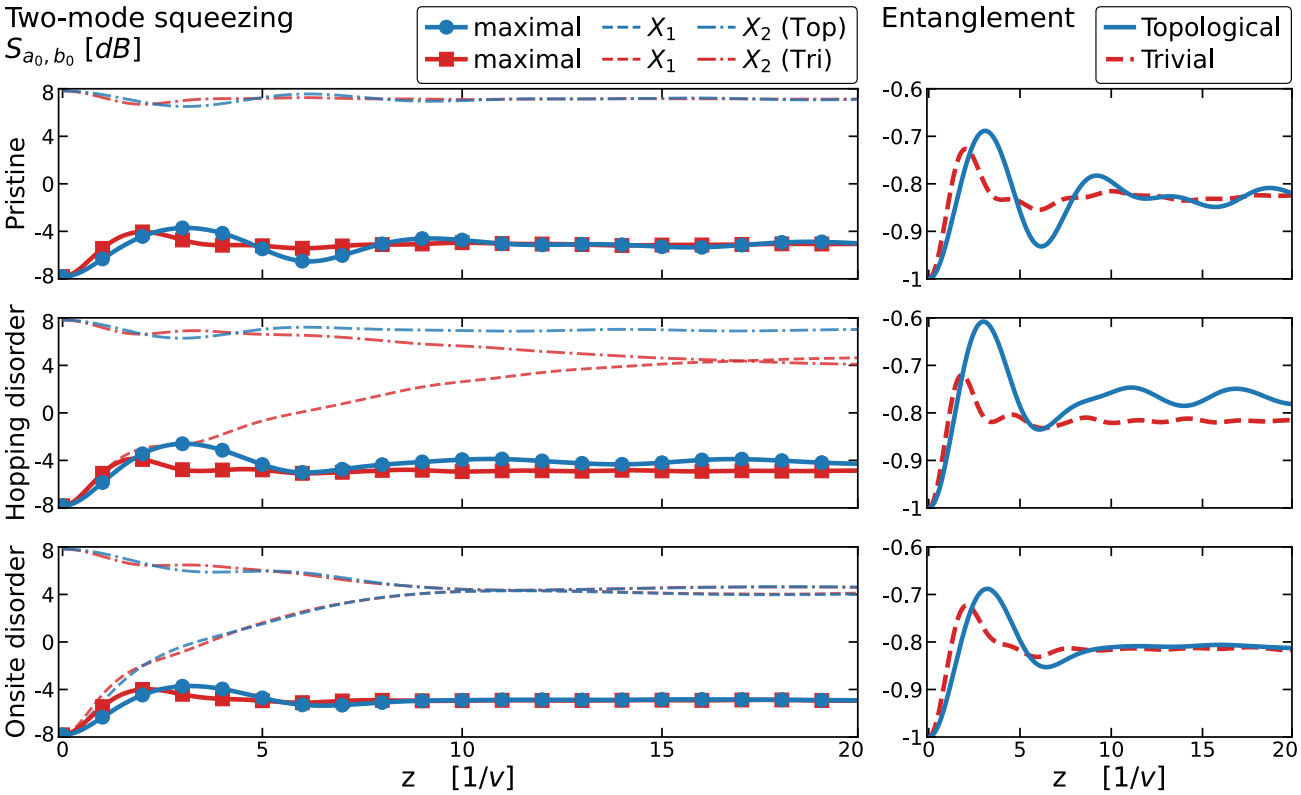


FIGURE 3.5: Two-mode squeezing and entanglement between both edge waveguides ($\alpha = 0.3$, $\xi = 0.9$). Hopping and onsite disorder values used are $d = 0.6v$. Left column: solid blue (red) curves with circular square show squeezing at the maximally squeezed quadrature for the topological (trivial) state. Dashed (dash-dotted) curves show squeezing at quadrature $X_1$ ($X_2$). Right column: solid blue (dashed red) curves show entanglement for the topological (trivial) state, in units relative to the initial state. Similar to maximal squeezing, entanglement is not sensitive topology nor disorder, but squeezing at the non-rotated quadratures reveals topological protection of the maximally entangled variables when chiral symmetry is preserved.

will show later in this section, carrying out the teleportation protocol in a topological lattice turns out to be advantageous compared with a topologically trivial lattice bearing a localized state. This topological advantage is quantified by a robust fidelity in the presence of disorder. In the following we describe the teleportation protocol and expose our main results.

The teleportation protocol has been developed in Ref. [148]. To make the discussion self-contained, in this paragraph we outline the main steps. We wish to transfer an arbitrary quantum state $|\psi_{\text{in}}\rangle$ from Alice's location to Bob's, for which we rely on a shared entanglement resource between both parties, given by the state $|\psi_{a,b}\rangle$. We must consider three modes of the field: $a$ and $b$ corresponding to the entangled modes sent to Alice and Bob respectively, and mode $c$ containing the input state. Defining $\chi_\mu = (q_\mu, p_\mu)$ the phase space basis of the respective modes, with $\mu = a, b, c$, the Wigner function of the system in this initial setup is

$$W_0(\chi_a, \chi_b, \chi_c) = W_{a,b}(\chi_a, \chi_b) W_{\text{in}}(\chi_c) \ , \tag{3.6}$$

where $W_{a,b}$ and $W_{\text{in}}$ represent the Wigner function of $|\psi_{a,b}\rangle$ and $|\psi_{\text{in}}\rangle$ respectively. Alice couples

her entangled mode with the input state at a 50:50 beam splitter, obtaining the Wigner function

$$W_1(\chi_a, \chi_b, \chi_c) = W_0\left(\frac{\chi_a - \chi_c}{\sqrt{2}}, \chi_b, \frac{\chi_c + \chi_a}{\sqrt{2}}\right) . \tag{3.7}$$

Alice then measures the quadratures corresponding to $q_a$ and $p_c$, which become classically determined random variables, following the probability distribution

$$\mathcal{P}(q_a, p_c) = \int \mathrm{d}p_a\, \mathrm{d}q_b\, \mathrm{d}p_b\, \mathrm{d}q_c\, W_1(\chi_a, \chi_b, \chi_c) . \tag{3.8}$$

Given a pair of measured values $q_a$ and $p_c$, the state at Bob's mode collapses to

$$\begin{aligned} W_2(\chi_b \,|\, q_a, p_c) &= \mathcal{N} \int \mathrm{d}p_a\, \mathrm{d}q_c\, W_1(\chi_a, \chi_b, \chi_c) \\ &= 2\mathcal{N} \int \mathrm{d}x\, \mathrm{d}y\, W_{\mathrm{in}}(x, y) W_{a,b}\left(\sqrt{2}q_a - x, y - \sqrt{2}p_c, q_b, p_b\right) , \end{aligned} \tag{3.9}$$

where normalization must be added explicitly as a result of the non-unitary measurement operation, and we defined $\sqrt{2}x = q_a + q_c$ and $\sqrt{2}y = p_a + p_c$ for the last equality. If the entanglement resource is non-rotated two-mode squeezed vacuum, then Bob's output state approaches the exact input state in the infinite squeezing limit, aside from a phase space displacement, that is $W_2(\chi_b \,|\, q_a, p_c) \to W_{\mathrm{in}}(q_b + \sqrt{2}q_a, p_b + \sqrt{2}p_c)$. To correct this, Bob displaces his mode, obtaining the final output state, given by the Wigner function

$$W_{\mathrm{out}}(q, p \,|\, q_a, p_c) = W_2(q - \sqrt{2}q_a, p - \sqrt{2}p_c |\, q_a, p_c) . \tag{3.10}$$

For the implementation of this protocol, we consider that the entangled two-mode squeezed state is sent to each party through a topological or trivial photonic lattice, as presented in section 3.4. Thus, at the output of lattice A, Alice extracts her share of the entangled state from the edge waveguide of the lattice tracing out all other modes, and so does Bob with lattice B. Finally, we take the input state as a single-photon, $|\psi_{\mathrm{in}}\rangle = c^\dagger|0\rangle$. Note however, that the teleportation protocol is valid for any input, which might even be unknown to our protagonists.

We perform the teleportation for pristine and hopping disordered lattices ($d = 0.3v$). The fidelity of a single teleportation event is calculated by $F = \pi \int \mathrm{d}q\, \mathrm{d}p\, W_{\mathrm{in}} W_{\mathrm{out}}$. Since the output state depends on the measured values $q_a$ and $p_c$, and on the random disorder present in the lattice, we report the average fidelity over all measurements and all random realizations, that is

$$\mathcal{F} = \frac{1}{N} \sum_{n=0}^{N-1} \int \mathrm{d}q_a\, \mathrm{d}p_c\, \mathcal{P} F , \tag{3.11}$$

with $N = 300$ the total number of random realizations. We may construct an averaged output Wigner function $\mathcal{W}_{\mathrm{out}}$ defined by

$$\mathcal{W}_{\mathrm{out}} = \frac{1}{N} \sum_{n=0}^{N-1} \int \mathrm{d}q_a\, \mathrm{d}p_c\, \mathcal{P}(q_a, p_c) W_{\mathrm{out}}(q, p \,|\, q_a, p_c) , \tag{3.12}$$

so the average fidelity is $\mathcal{F} = \pi \int \mathrm{d}q\, \mathrm{d}p\, W_{\mathrm{in}} \mathcal{W}_{\mathrm{out}}$. Even though the output state never takes the exact form of $\mathcal{W}_{\mathrm{out}}$, it allows to visualize the proximity of the output state to the input one in the general case.

When teleporting the single photon state employing the pristine lattices, we find practically identical results between the topological and trivial systems, as shown in Fig. 3.6-(b) and (d), characterized by an average fidelity of 0.483 and 0.486 respectively. Comparing with the input Wigner function (Fig. 3.6-(a)), we observe that the fidelity losses are mainly explained by a reduction of the peak values, and a consequent widening of the function. Negativity of the output function serves as a landmark of the preservation of the input state's quantum nature, which can only be achieved by means of quantum teleportation schemes. Quantitatively, the reduction of the negative peak at the origin with respect to the input state is of 13.0% and 14.3% in the topological and trivial systems respectively.

The averaged output state of the topological system remains practically unchanged when introducing hopping disorder, as shown in Fig. 3.6-(c), maintaining the fidelity of the pristine lattice. The output Wigner function continues to take negative values, with a peak reduction of 14.1%,

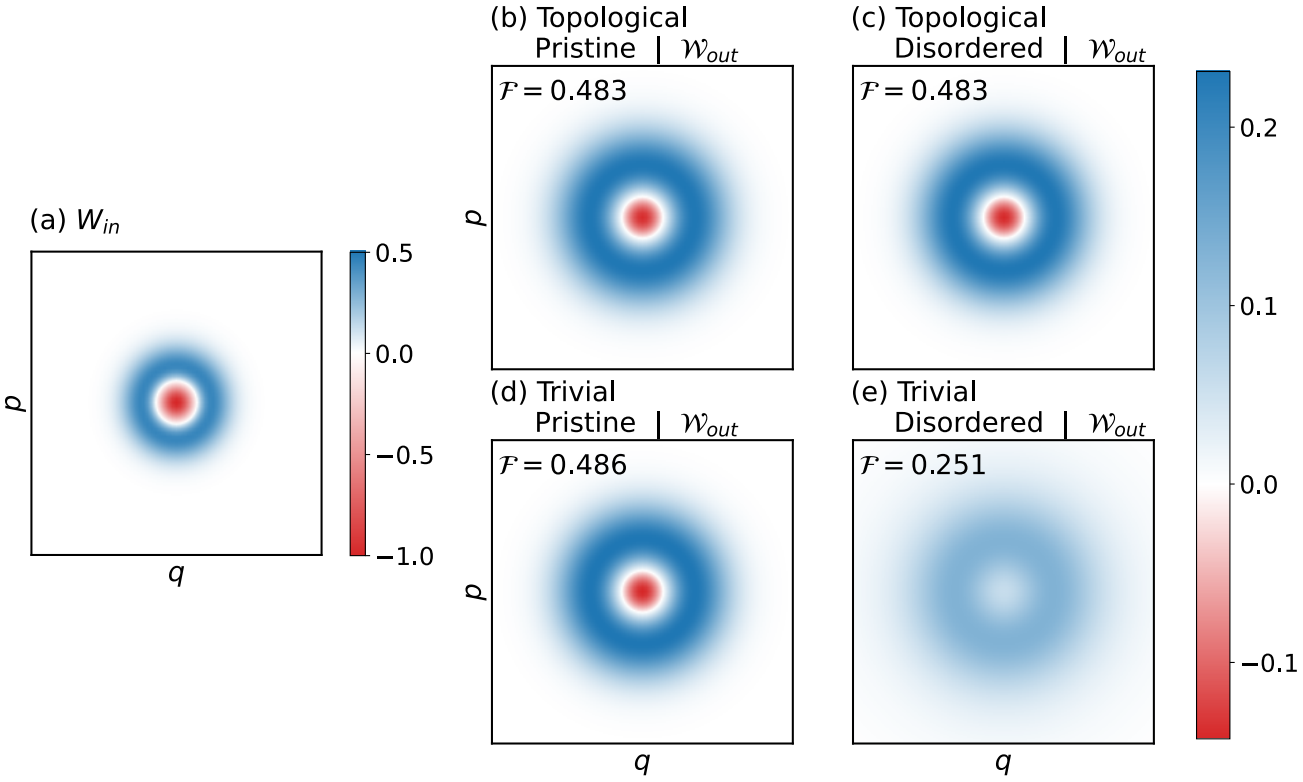


FIGURE 3.6: **(a)** Input Wigner function to be teleported. **(b)** and **(d)** (**(c)** and **(d)**) Averaged output Wigner function $\mathcal{W}_{\mathrm{out}}$ for the pristine and hopping disordered $d = 0.3v$ topological (trivial) systems, in units relative to the peak value of $W_{\mathrm{in}}$. The fidelity of the output states is indicated on each panel, and the colorbar on the right applies to panels (b)-(e). Teleportation in the topological system proves to be robust against hopping disorder, preserving the fidelity of the output state, and preserving the quantum nature of the single-photon input state represented by negative values in the Wigner function.

proving that teleportation in the topological system robustly preserves the quantum coherence of the input state. In contrast, teleportation in the topologically trivial system rapidly deteriorates as disorder is added. Even for low levels of disorder, the average fidelity falls to 0.242 —roughly half of that of the pristine system— and even though the output function presents a local minimum at the origin, it does not take negative values. The drastic difference in the teleportation results between the topological and trivial systems is a consequence of topological protection of the squeezed quadrature. Transmission of the entangled two-mode state to the parties through a topological state ensures that Alice measures the maximally entangled variables, regardless of the magnitude of hopping disorder present in the lattice, resulting in robust preservation of quantum coherence of the teleported state.

## 3.6 Final remarks

We have studied the propagation of squeezing and entanglement in a topological SSH waveguide array, focusing on the effects of the lattices topology in this phenomena. We found that topological ordering of the lattice robustly preserves the phase of the squeezed quadrature when propagating squeezed light through a topologically protected localized state, for both single- and two-mode squeezed light. We also showed that the distribution of squeezing across the lattice inherits the spatial distribution of the localized state to which it is coupled, inheriting its topological protection as well. We discussed the interplay between entanglement, squeezing and the phase of the squeezing, concluding that the topological phase of the lattice fixes the entangled variables. We finally provided a practical implementation of this system in a quantum teleportation protocol, where transmission of the entanglement resource to the parties through a topological lattice grants robustness and preservation of the quantum coherence of the teleported state.

We expect our findings on topological protection of squeezing to be of interest to any development in continuous variable quantum information, mainly as an alternative to protecting quantum coherence in photonic platforms. However, exploitation of topological phenomena in quantum optic systems —in particular continuous variable ones— is only recent, and its full possibilities are yet to be discovered. Our research is based on the SSH lattice, whose topological phase is broken by onsite disorder which is always present to some extent in realistic devices; and being a one-dimensional lattice, this system is particularly sensitive to Anderson localization. Thus, a natural interest arises in studying the behavior of quantum light in two-dimensional lattices, with propagating edge states which enjoy better topological protection.

## Acknowledgments

We thank P. Solano for useful comments and suggestions. J. M. D. is supported by CONICYT grant CONICYT-PFCHA/MagísterNacional/2019-22200526. C. H-A. acknowledges support by CONICYT-PAI grant N°77180003, FONDECYT grant N°11190078, and ANID - Millenium Science Initiative Program . ICN17_012. L. E. F. F. T. Acknowledges the support of FONDECYT grant N° 1211038, the Abdus Salam International Centre for Theoretical Physics and the Simons Foundation.

## 3.7 Appendixes

### 3.7.A Extended results of section 3.3.2

In this section we present a more complete report of the results discussed in section 3.3.2, that could help the reader follow the corresponding discussions. For all figures we have used $\alpha = 0.3$ and $\xi = 0.9$.

In Fig. 3.7 we show one-mode squeezing along the propagation axis at waveguides $a_1$, $a_2$ and $a_4$ of the topological lattice, and waveguides $a_1$ and $a_2$ of the trivial one. These results allow to envision the spatial distribution of one-mode squeezing across the lattices.

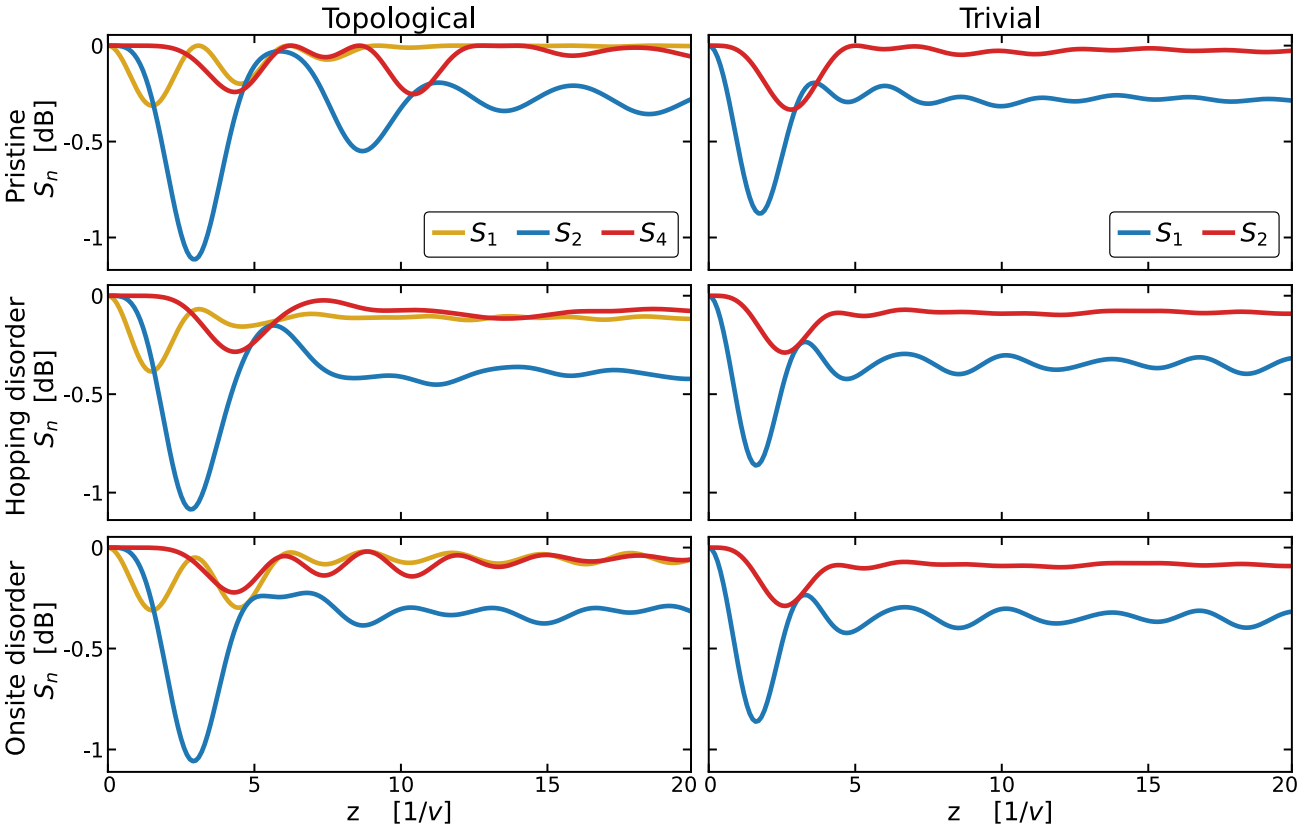


FIGURE 3.7: One-mode squeezing along the propagation axis ($\alpha = 0.3$, $\xi = 0.9$). Hopping and onsite disorder values used are $d = 0.6v$. The site at which the measurement is taken is indicated in the legend, which is valid for the whole column.

In Fig. 3.8 we show two-mode squeezing along the propagation axis, measured between the edge waveguide and the first two waveguides that take part in the localized eigenmode, namely, waveguides $a_2$ and $a_4$ of the topological lattice, and waveguides $a_1$ and $a_2$ of the trivial one. This shows the effect of the phase relation between the modes on two-mode squeezing.

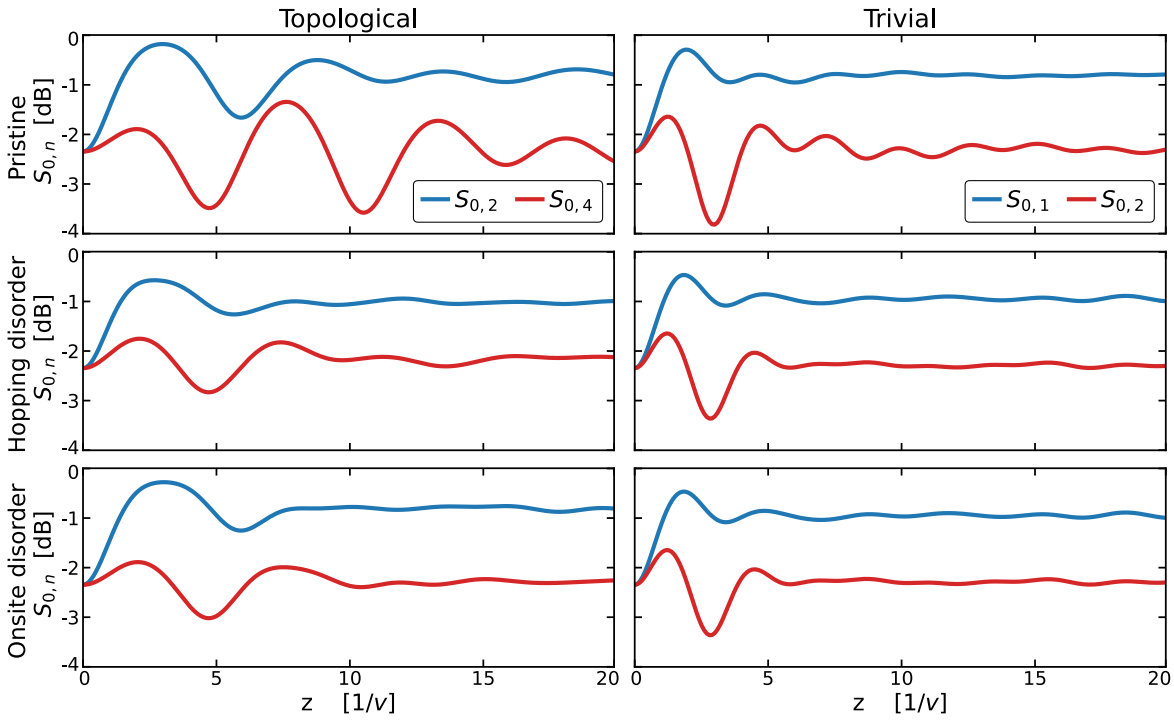


FIGURE 3.8: Two-mode squeezing along the propagation axis ($\alpha = 0.3$, $\xi = 0.9$). Hopping and onsite disorder values used are $d = 0.6v$. The site at which the measurement is taken is indicated in the legend, which is valid for the whole column.

## 3.7.B On the statistical fluctuations for Fig. 3.4 and 3.5

In this section we refer to the statistical fluctuations for the data presented in Fig. 3.4 and 3.5. In Fig. 3.9 we show maximal one-mode squeezing corresponding to the data presented in Fig. 3.4, and maximal two-mode squeezing and entanglement corresponding to the data in Fig. 3.5, along with the confidence intervals for the corresponding quantities. We observe that after the transient response of the system when the initial state is injected at the edge waveguide, the curves of the topological and trivial state take approximately equal values, falling within the confidence interval of each other. We also observe that hopping disorder induced fluctuations are considerably larger than those generated by onsite disorder in both systems. Furthermore, fluctuations in the hopping disordered topological state are larger than those of the trivial one. However, the magnitude of the fluctuations is consistently lower than the magnitude of the physical quantities themselves in all cases. We have checked as well that increasing the number of realizations yields narrower confidence intervals, and that higher disorder values yield larger confidence intervals, in tune with the behavior observed in Fig. 3.2.

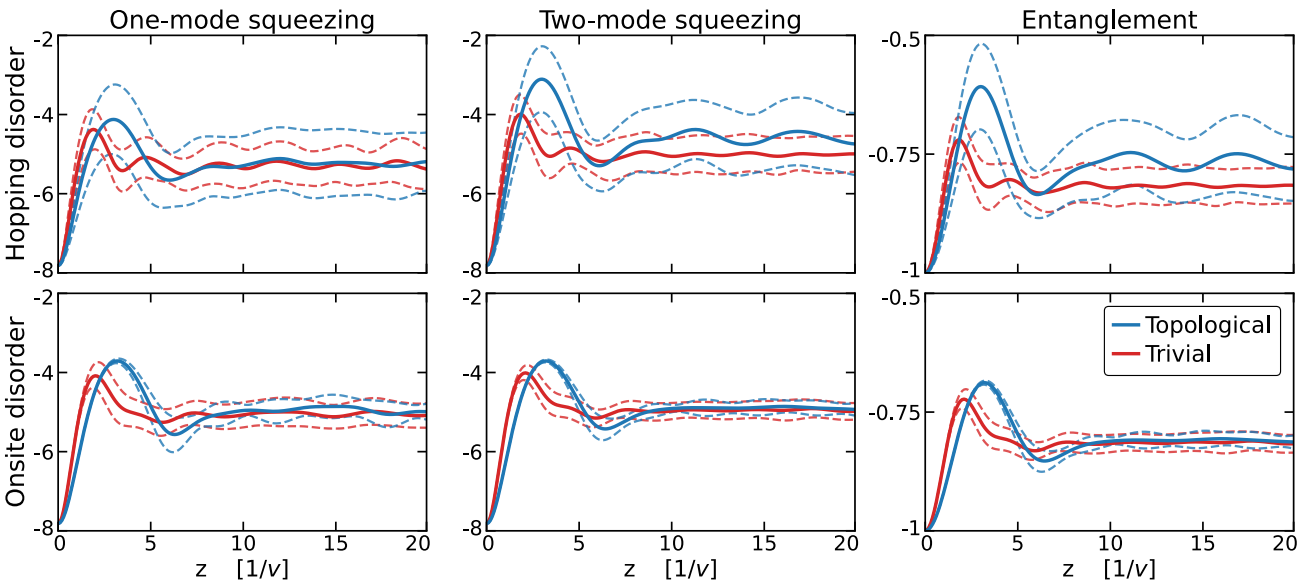


FIGURE 3.9: Maximal one-mode squeezing corresponding to the data in Fig. 3.4, and maximal two-mode squeezing and entanglement corresponding to the data un Fig. 3.5. Statistical average values are represented by solid lines, while dashed lines represent the confidence interval associated with the standard deviation, with blue (red) lines referring to the topological (trivial) system.

# Part II

# Interaction between electrons and chiral phonons in two-dimensional materials

Unlike the chirality of electrons, a surge for understanding and exploiting the intrinsic chirality of phonons has only surfaced in recent years. Here we report on the effects of electron with chiral phonon interaction in two-dimensional materials using a non-perturbative Fock space solution. The phonon chirality breaks time reversal symmetry and generates inelastic processes which open a valley selective gap bridged by copropagating edge states, which coexist with a continuum of extended states. Our transport simulations reveal a strong directional asymmetry, and test the robustness of the edge states. These results provide a first step in the zoology of possible effects derived from the interaction with chiral phonons and their hybrid electron-phonon states of matter.

This part contains an adapted version of [58], written by the author of this thesis, Hernán L. Calvo, and Luis E. F. Foa Torres, presented in chapter 4.

# Chapter 4

# Copropagating edge states produced by the interaction between electrons and chiral phonons in two-dimensional materials

## 4.1 Introduction

Since the very beginning of the quantum theory of solids [154, 155], the interaction between electrons and lattice vibrations has provided a long list of exciting discoveries and its effects have proven to be ubiquitous in condensed matter physics. Hallmarks of this interaction pervade in three dimensional materials [156], as well as in low dimensional systems [157–161]. Prominent examples include the role played by electron-phonon (e-ph) interaction in the development of the theory of superconductivity [59, 61, 162] and conducting polymers [20], where charge doping is used to circumvent the Peierls transition [82, 163]. More recently, different studies have pointed the possibility of electron-phonon-induced bandgaps [164, 165], robust edge states [62], and phonon-induced topological phases [63, 64].

In 2015 a new twist in this field was triggered by the prediction of phonons with *intrinsic* chirality in monolayer materials [65]. Further theoretical studies [67–70] and the experimental observation of circular phonons in monolayer tungsten diselenide [66] brought a focus to this overlooked property. Thanks to the breaking of inversion symmetry, the degeneracy between clockwise and counterclockwise modes can be lifted at high symmetry points of the Brillouin zone (BZ), leading to the intrinsic chirality of the modes. Today, chiral phonons are at a focal point in the context of the pseudogap of the cuprates [166, 167], where phonons have been proposed to become chiral in the pseudogap phase of these materials [166]. Recent experiments have shown the possibility of achieving electrostatic control over the angular momentum of phonons [168]. A proposal for chiral phonons with non-vanishing group velocity [71] also adds interest to this blooming area. But, notably, the effects of e-ph interaction with chiral phonons remains mostly unexplored. Therefore, it is of interest to address this issue. One may wonder whether the

chirality of phonons could give rise to any unusual effects on the electronic structure through their mutual interaction, or whether new hybrid e-ph states could be controlled by tuning either the electronic or phononic degrees of freedom.

Here we explore the effects of e-ph interaction with chiral phonons in two-dimensional materials with broken inversion symmetry, looking for novel hybrid e-ph states of matter. Aided by a non-perturbative and non-adiabatic Fock-space solution, we isolate the effect of a single of such modes. A first finding is that the chirality of the phonons gets imprinted in the e-ph interaction term, which breaks time-reversal symmetry while introducing inelastic *Umklapp* processes[1]. We show that this interaction opens a gap in one of the two inequivalent valleys which is bridged by two hybrid e-ph edge states. Interestingly, these edge states turn out to propagate in the same direction and coexist with a continuum of states in the ungapped valley. Further quantum transport simulations demonstrate that the copropagating edge states are robust, as they can withstand even moderate amounts of short-range disorder.

## 4.2 Hamiltonian model

We consider a honeycomb lattice including the interaction between electrons and a single phonon mode. The Hamiltonian is written as:

$$\mathcal{H} = \mathcal{H}_{\text{e}} + \mathcal{H}_{\text{ph}} + \mathcal{H}_{\text{e-ph}} \ , \tag{4.1}$$

where $\mathcal{H}_{\text{e}}$ and $\mathcal{H}_{\text{ph}}$ are the independent electronic and phonon contributions, while $\mathcal{H}_{\text{e-ph}}$ is the interaction term. The electronic contribution is modeled as a simple nearest neighbors Hamiltonian for a honeycomb lattice with a single orbital per atom and a staggered onsite term accounting for the inversion symmetry breaking:

$$\mathcal{H}_{\text{e}} = \sum_n \Delta_n c_n^\dagger c_n + \gamma_0 \sum_{\langle n,m \rangle} c_n^\dagger c_m \ , \tag{4.2}$$

where $c_n$ stands for the electronic annihilation operator at site $n$. The second sum on the right hand side runs over nearest neighbors, $\gamma_0$ is the nearest-neighbors hopping parameter. The on-site energy $\Delta_n$ models a staggering potential and is equal to $\Delta$ if the site belongs to sublattice A and -$\Delta$ if it belongs to sublattice B. For the phonons we consider a single mode, which we choose as a chiral mode with momentum $\mathbf{G}$ and frequency $\omega$, described by:

$$\mathcal{H}_{\text{ph}} = \hbar\omega a^\dagger a \ , \tag{4.3}$$

with $a$ the phonon annihilation operator.

The e-ph interaction term is of the Su-Schrieffer-Heeger form [52]. It follows from quantizing the linear correction to the hopping amplitudes due to the atomic displacements from equilibrium. We consider that the phonon mode generates lattice vibrations where the motion of site $n$ respect to its equilibrium position is

$$\delta\mathbf{r}_n(t) = \text{Re}\left[A\text{e}^{-\text{i}(\omega t - \mathbf{G}\cdot\mathbf{R}_n)}\mathbf{u}_\nu\right] \ , \tag{4.4}$$

[1] *Umklapp* processes refer to scattering processes where the initial and final momentum are related by a non-zero reciprocal lattice vector [104]

with $\mathbf{R}_n$ the lattice vector of the corresponding unit cell, $A$ the amplitude of the motion, $\nu$ indicating the sublattice of site $n$ ($\nu$ = A, B), and $\mathbf{u}_\nu$ the eigenvector of the phonon mode on sublattice $\nu$. Phonon chirality is given by a circular motion of the sites, represented in the phonon eigenvector $\mathbf{u}$, which constitutes an intra-cell contribution to the chirality, as well as by an inter-cell term given by the phase $\mathrm{e}^{\mathrm{i}\mathbf{G}\cdot\mathbf{R}_n}$ acquired by the motion in the different unit cells [65]. We incorporate the lattice vibrations to the tight-binding hamiltonian as a renormalization of the electronic hopping amplitude between sites $n$ and $m$ [62],

$$\gamma_{n,m} = \gamma_0 \exp\left[-b\left(\frac{|\mathbf{r}_n - \mathbf{r}_m|}{a_0} - 1\right)\right] , \tag{4.5}$$

with $a_0$ the equilibrium nearest neighbor distance, $b$ the decay rate, and $\mathbf{r}_n = \mathbf{r}_n^0 + \delta\mathbf{r}_n$, with $\mathbf{r}_n^0$ the equilibrium position of site $n$. We assume small vibration amplitudes, $|A| \ll a_0$, where the zero-th order term resulting from Eq. (4.5) accounts for the bare hoppings represented in $\mathcal{H}_\mathrm{e}$. The first order terms couple electronic degrees of freedom with lattice vibrations, obtaining the e-ph hopping amplitudes

$$\gamma_{n,m} = -\gamma_1 \hat{\mathbf{r}}_{n,m} \cdot \left[\left(\mathrm{e}^{\mathrm{i}\mathbf{G}\cdot\mathbf{R}_n}\mathbf{u}_\nu - \mathrm{e}^{\mathrm{i}\mathbf{G}\cdot\mathbf{R}_m}\mathbf{u}_\mu\right)\mathrm{e}^{-\mathrm{i}\omega t} + \mathrm{c.c.}\right] , \tag{4.6}$$

where $\gamma_1 \ll \gamma_0$ sets the strength of e-ph interactions, $\hat{\mathbf{r}}_{n,m} = \left(\mathbf{r}_n^0 - \mathbf{r}_m^0\right)/a_0$, and $\nu$ ($\mu$) indicates the sublattice of site $n$ ($m$). We impose phonon quantization replacing the harmonic time dependence by bosonic phonon operators, $\mathrm{e}^{-\mathrm{i}\omega t} \to a^\dagger$ and $\mathrm{e}^{\mathrm{i}\omega t} \to a$. The interaction hamiltonian thus reads

$$\mathcal{H}_\text{e-ph} = -\gamma_1 a^\dagger \Big[\sum_{\langle n,m\rangle} c_n^\dagger c_m \mathrm{e}^{\mathrm{i}\mathbf{G}\cdot\mathbf{R}_n}\hat{\mathbf{r}}_{n,m}\cdot\left(\mathbf{u}_\nu - \mathrm{e}^{-\mathrm{i}\mathbf{G}\cdot\mathbf{R}_{n,m}}\mathbf{u}_\mu\right)\Big] + \mathrm{h.c.} , \tag{4.7}$$

with $\mathbf{R}_{n,m} = \mathbf{R}_n - \mathbf{R}_m$. The e-ph hoppings contain a spatial dependence due to momentum interchange between both particles. Defining the Fourier transform

$$c_n = \int_\mathrm{BZ} \mathrm{d}^2\mathbf{k}\, \mathrm{e}^{\mathrm{i}\mathbf{k}\cdot\mathbf{R}_n} c_{\nu,\mathbf{k}} , \tag{4.8}$$

the interaction Hamiltonian reads

$$\mathcal{H}_\text{e-ph} = -\gamma_1 a^\dagger \Big[\int_\mathrm{BZ} \mathrm{d}^2\mathbf{k} \sum_{\nu\neq\mu} c_{\nu,\mathbf{k}}^\dagger c_{\mu,\mathbf{k}+\mathbf{G}} \sum_m \mathrm{e}^{-\mathrm{i}(\mathbf{k}+\mathbf{G})\cdot\mathbf{R}_{n,m}}\hat{\mathbf{r}}_{n,m}\cdot\left(\mathbf{u}_\nu - \mathrm{e}^{-\mathrm{i}\mathbf{G}R_{n,m}}\mathbf{u}_\mu\right)\Big] + \mathrm{h.c.} , \tag{4.9}$$

where the first sum runs over the sublattices, and the second sum runs over all sites $m$ of sublattice $\mu$, which are nearest neighbors of a given site $n$ of sublattice $\nu$. The term explicitly written in Eq. (4.9) accounts for momentum conserving phonon emission processes, where an electron with momentum $\mathbf{k}+\mathbf{G}$ is annihilated, while an electron with momentum $\mathbf{k}$ and a phonon with momentum $\mathbf{G}$ are created. The hermitian conjugate term corresponds to phonon absorption.

For what follows we consider the phonon momentum $\mathbf{G}$ corresponding to valley $K^+$, where atoms of sublattice A and B exhibit clockwise and counter-clockwise motion respectively, as depicted in Fig. 4.1. The motion of the sites acquires a phase $\mathrm{e}^{\pm\mathrm{i}2\pi/3}$ between neighboring unit cells, thus, the non-zero phonon momentum effectively modifies the periodicity of the lattice. We may however retain the original unit cell, as was done in Eq. (4.8), where the phonon

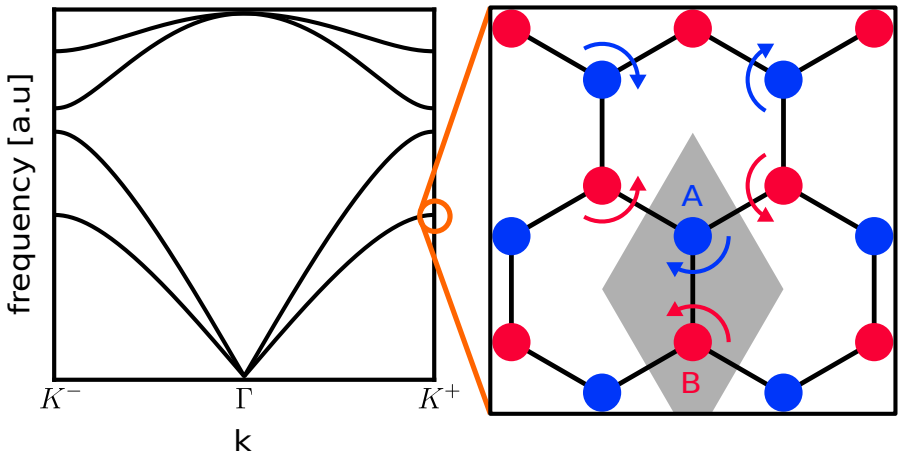


FIGURE 4.1: Scheme depicting the chiral phonon mode considered during this work. The left panel shows the phonon band structure of a honeycomb lattice, in arbitrary units, with chiral phonons at high symmetry points. Breaking inversion symmetry lifts the degeneracy between the two middle bands at the valleys, and generates circular motion of the sublattices with different amplitudes, allowing for phonon modes with net chirality. We focus on the mode represented in the right panel, where sublattice A (B), depicted by blue (red) circles, exhibits counter-clockwise (clockwise) circular motion, as indicated by the corresponding arrows. Due to the non-zero phonon momentum, the movement acquires a phase $e^{\pm i2\pi/3}$ between neighboring unit cells, represented by the arrows.

momentum generates non-vertical transitions in the original BZ. A zone-folding scheme may be developed in this case so the system presents vertical transitions in a reduced BZ (rBZ), folding areas B and C of the BZ into area A, as depicted in Fig. 4.2, taking advantage of the threefold periodicity of the inter-cell phonon term (see appendix 4.6.A).

## 4.3 Band structure: Gaps and edge states

Instead of treating the e-ph interaction perturbatively as it is most usual, here we will use the non-perturbative and non-adiabatic approach introduced in [169, 170]. The main idea is the exact mapping of the many body problem onto a one-particle problem in a higher-dimensional space, where each phonon mode introduces an additional dimension to the original electronic problem. This can be visualized after writing the problem in a Fock space basis: The full hamiltonian can be viewed as a semi-infinite series of *replicas* of the original purely electronic problem centered at energies $n_{\rm ph}\hbar\omega$, with $n_{\rm ph} \in \mathbb{N}_0$, coupled by the interaction hamiltonian. The phonon induced non-vertical transitions couple valley $K^-$ in $n_{\rm ph} = 0$ with valley $K^+$ in $n_{\rm ph} = 1$, generating an indirect valley selective gap at the replica crossing, as shown in Fig. 4.2-(b). The other valleys, namely $K^+$ in $n_{\rm ph} = 0$ and $K^-$ in $n_{\rm ph} = 1$, are not connected by the phonon mode and are therefore not gapped. As a consequence, the system does not present a global gap at the replica crossing, but rather a valley selective pseudogap. For $\hbar\omega \ll \gamma_0$ the valleys may be described by massive Dirac Hamiltonians. Within this regime we estimate the magnitude of the pseudogap, which is $3\sqrt{2}\gamma_1|\mathbf{L}^\dagger\mathbf{u}_{\rm A} + \mathbf{R}^\dagger\mathbf{u}_{\rm B}|$, with $\mathbf{L} = (1, -i)^t/\sqrt{2}$ ($\mathbf{R} = (1, i)^t/\sqrt{2}$) representing the counter-clockwise (clockwise) circular motion of the atoms. Interestingly, the magnitude of the gap is sensitive to the chirality of each sublattice.

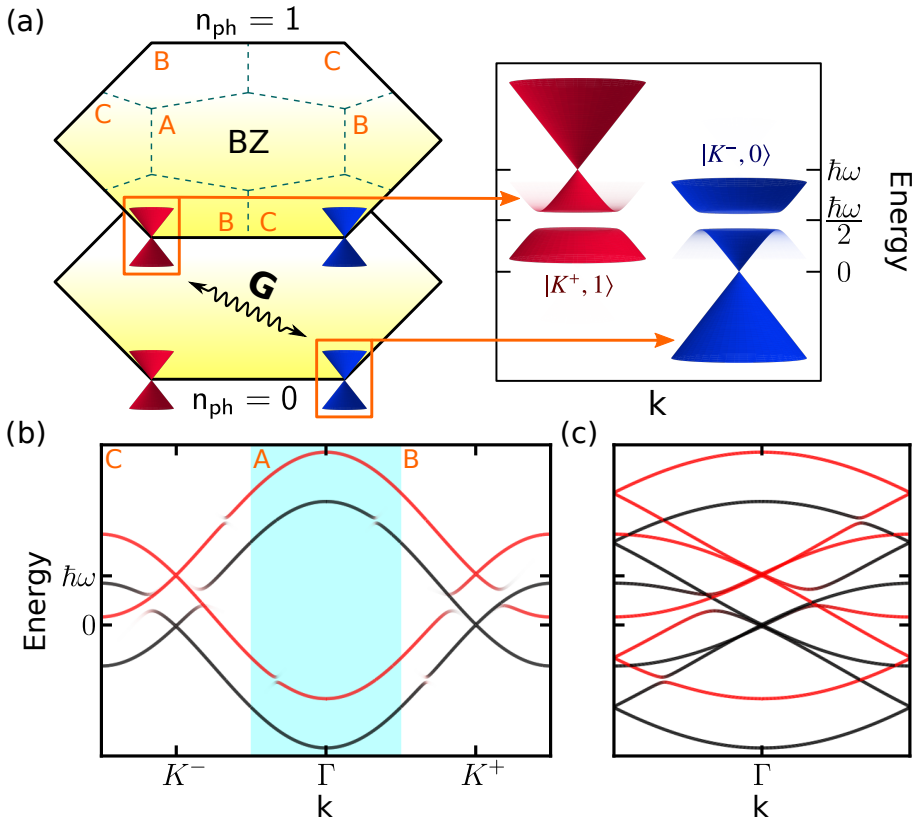


FIGURE 4.2: **(a)** Considering the phonon Fock space, the system can be viewed as a semi-infinite series of pure electronic Hamiltonian replicas centered at energies $n_{\text{ph}}\hbar\omega$, with $n_{\text{ph}} \in \mathbb{N}_0$ the corresponding phonon population. e-ph interactions generate non-vertical transitions in the BZ, between momentum $\mathbf{k}$ in replica $n_{\text{ph}} = 0$ to momentum $\mathbf{k} - \mathbf{G}$ in replica $n_{\text{ph}} = 1$, with $\mathbf{G} = K^+$ the phonon momentum. A pseudogap opens in the non-vertical intersection between the Dirac cones at valleys $K^-$ and $K^+$ in replicas $n_{\text{ph}} = 0$ and $n_{\text{ph}} = 1$ respectively. **(b)** Band structure of the bulk system where the valley selective gap is seen at the replica crossing. The color scale indicates the weight of the bands on $n_{\text{ph}} = 0$ (black) and $n_{\text{ph}} = 1$ (red). **(c)** A zone-folding scheme may be developed, where areas B and C of the BZ of the hexagonal lattice are folded into area A (as indicated in panels (a) and (b)), forming the rBZ where the system presents vertical transitions. The band structure in the rBZ is represented in panel (c), where the $k$-path plotted corresponds to that of the cyan shaded area in panel (b).

For a ribbon geometry, we expect to observe the effects of e-ph interaction in any geometry that allows to distinguish processes occurring at the distinct valleys. We focus on the energy dispersion projected to replicas $n_{\text{ph}} = 0$ and $n_{\text{ph}} = 1$. For a zigzag ribbon we observe two edge states in the replica crossing energy region, which correspond to a hybridization of the flat bands of each replica, as shown in Fig. 4.3. Projection of the states to the different momentum and phonon subspaces, as shown in Fig. 4.3-(c) and (d) proves that they correspond to localized edge states which bridge the valley selective bulk band gap, and one may wonder whether they could have a topological origin (see appendix 4.6.C). Remarkably, we find that the edge states propagate in the same direction at the opposite borders of the ribbon, as we further clarify in the next section. The remaining states that coexist at the same energy $\hbar\omega/2$ do not hybridize

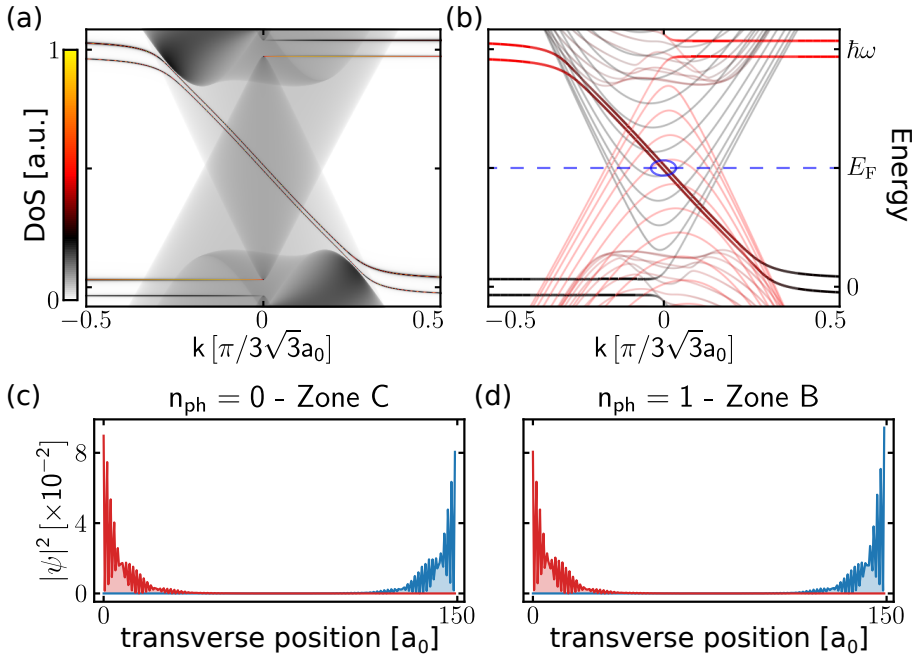


FIGURE 4.3: **(a)** Density of States (DoS) near the edges of a semi-infinite zigzag ribbon, in arbitrary units. A valley selective gap opens in the replica crossing, bridged by two edge states with parallel velocities. These states coexist with a continuum of extended states of the ungapped valleys. **(b)** Band structure of a zigzag ribbon (of width $150a_0$). The color scale indicates the weight of the bands on $n_{\rm ph} = 0$ (black) and $n_{\rm ph} = 1$ (red), while the transparency of the curves is related to the localization of the states (ranging from light curves for extended states, to opaque curves for states with an inverse participation ratio larger than 0.1) The edge states described in (a), at energy $E_{\rm F} = \hbar\omega/2$, are indicated with a blue circle. The horizontal axis in (a) and (b) corresponds to the rBZ projected to the periodicity direction. **(c)** and **(d)** Projection of the edge states in (b) to zone C of the BZ in $n_{\rm ph} = 0$, and zone B in $n_{\rm ph} = 1$, showing that they are localized at opposite borders of the ribbon. Other parameters used are $\gamma_1 = 0.025\gamma_0$, $\hbar\omega = 0.3\gamma_0$, and $\Delta = 0.01\gamma_0$.

with their replicas, and correspond to the continuum of bulk states from the ungapped valleys.

For the case of ribbons with Klein edges we find edge states of the same nature, which bridge the valley selective gap and coexist with a continuum of extended states, however their propagation direction is reversed with respect to the zigzag case (see appendix 4.6.D). We interpret this behavior as stemming from the physics of the flat bands in honeycomb lattices with different terminations: ribbons with Klein-edges develop flat bands in a $k$-space region complementary to those with zigzag edges [171]. A different scenario is presented for an armchair geometry, where processes occurring at both valleys are not distinguishable, thus the consequences of the valley selective bulk gap are not observed (see appendix 4.6.D).

## 4.4 Quantum transport fingerprints of copropagating electron-phonon states

One may wonder about possible hallmarks of the electron-chiral-phonon interaction that might be imprinted on the transport properties. To address this question we consider a zigzag ribbon with e-ph interaction in the entire system, and compute the total transmittance (including elastic and inelastic processes) between two local probes weakly coupled to a single site located in different transverse layers of the ribbon (labeled as L and R), as depicted in the insets of Fig. 4.4. We choose the input site at each edge of one layer (marked with a red dot in Fig. 4.4) and compute the transmittance to a site on the opposite layer with transverse position $x$.

Fig. 4.4-(a)–(d) shows the transmittance for a pristine ribbon, while panels (e)–(h) show the results for ribbons with random vacancies with a density of 0.1%, averaged over 100 random realizations. A first feature revealed by our simulations is a strong directional asymmetry, transport is strongly suppressed in one direction (from L to R as shown in panels (a) and (b)) irrespective of the source being at one edge or the opposite, while in the reverse direction it is strongly focused near the same edge as the source (as shown in panels (c) and (d)). The small non-vanishing transmittance in panels (a) and (b) can be attributed to a contribution stemming from bulk states. This behavior is consistent with the nature of the copropagating edge states

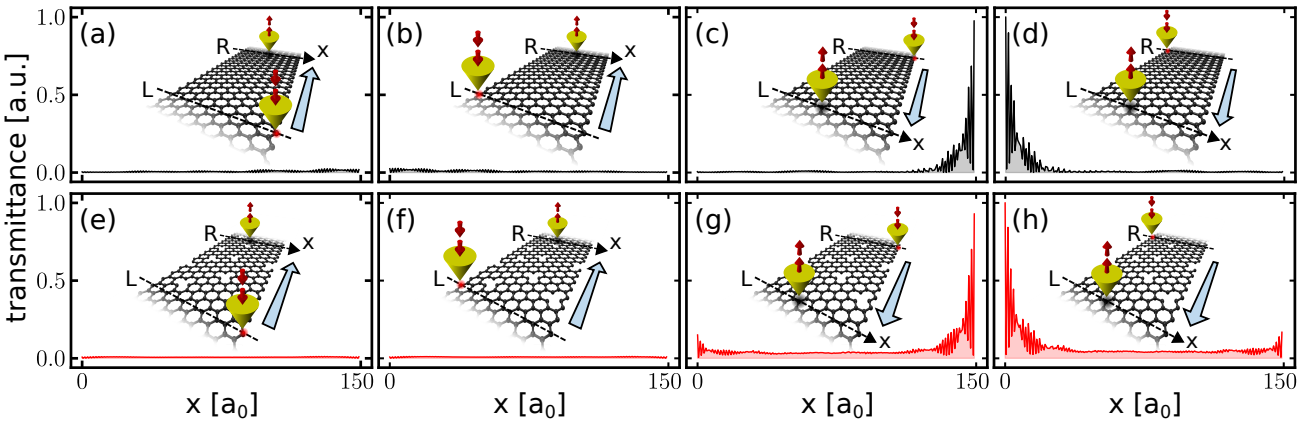


FIGURE 4.4: Transmittance, in arbitrary units, between non-invasive probes located on different transverse layers of a zigzag ribbon (of width $150a_0$) separated by a distance $300\sqrt{3}a_0$. The input site is taken at the edge of the corresponding layer, while the output site runs over the entire output layer, with transverse position $x$. For easier visualization, the situation for each panel is represented as an inset, where the input sites are marked in red and signaled by downwards red arrows. The transmittance includes both the elastic and inelastic contributions and the energy of the incoming electrons is set to $\hbar\omega/2$. Panels on the top row ((a)–(d)) correspond to the pristine system while those on the lower row ((e)–(h)) include disorder (random vacancies at 0.1%), where each of set of plots is normalized separately to its maximum value. Computing the transmittance from one layer to the other, and vice versa, allows to unveil the copropagating nature of the edge states and their robustness: transport is suppressed in the L to R direction (panels (a), (b), (e) and (f)) regardless of the edge of the input, while transport in the R to L direction (panels (c), (d), (g) and (h)) remains peaked at the input edge even in presence of disorder.

signaled earlier close to $\hbar\omega/2$.

Panels (e)–(h) show that the behavior obtained for the pristine system is able to withstand a moderate amount of disorder. Disorder in the lattice generates some edge to edge scattering in the R to L direction, represented by an increased bulk contribution and a small peak at the opposite edge of the input site. However, the spatial distribution remains strongly peaked at the input edge. Importantly as well, the directional asymmetry in the transmittance persists entirely, even against this worst-case scenario of short range disorder.

## 4.5 Final remarks

Our results show a first glimpse of the effects of electron-chiral-phonon-interaction in two-dimensional materials. The interaction with chiral phonons provides for a novel effective time-reversal symmetry breaking term. Unlike other known symmetry breaking terms, such as a magnetic field [172], a Haldane term [9], or laser-assisted processes [173], the phenomenology turns out to be different, resulting in copropagating hybrid electron-phonon edge states coexisting with a gapless bulk. This new phenomenology stems from the rich interplay between *Umklapp* processes and inelastic effects allowed by the interaction with chiral phonons.

A potential caveat of our study so far is the fact that a single phonon mode is considered. However, the mode is taken into account non-perturbatively and, in the spirit of the Peierls transition, given a mechanism that selects this peculiar high-symmetry phonon mode, the effect of the remaining modes should remain perturbative, thereby lessening their importance [60, 174]. Furthermore, experiments may specifically target chiral phonons by enhancing the electron-phonon interaction through optical pumping of the selected mode [175, 176]. The predicted hallmarks in the transport properties could be accessed through scanning gate microscopy [177]. We hope that our results could foster new experiments in this promising *terra incognita*.

# Acknowledgments

We thank the support of the EU Horizon 2020 research and innovation program under the Marie-Sklodowska-Curie Grant Agreement No. 873028 (HYDROTRONICS Project). L. E. F. F. T. also acknowledges the support of The Abdus Salam International Centre for Theoretical Physics and the Simons Foundation. H. L. C. acknowledges financial support by Secretaría de Ciencia y Tecnología de la Universidad Nacional de Córdoba (SECYT-UNC); and Agencia Nacional de Promoción Científica y Tecnológica (ANPCyT, PICT-2018-03587). H. L. C. is member of CONICET. J.M.D. is supported by CONICYT Grant CONICYT-PFCHA/MagísterNacional/2019-22200526

## 4.6 Appendixes

### 4.6.A The interaction hamiltonian: Detailed calculation and zone-folding scheme

In this appendix we describe with further detail the hamiltonian of the system. Starting from Eq. (4.9), we define

$$t_{\text{e-ph}}(\mathbf{k}) = -\gamma_1 \sum_m \mathrm{e}^{-\mathrm{i}\mathbf{k}\cdot\mathbf{R}_{n,m}} \hat{\mathbf{r}}_{n,m} \cdot \left(\mathbf{u}_{\mathrm{A}} - \mathrm{e}^{-\mathrm{i}\mathbf{G}\cdot\mathbf{R}_{n,m}} \mathbf{u}_{\mathrm{B}}\right) \ , \tag{4.10}$$

where the sum runs over all sites $m$ of sublattice B which are nearest neighbor of a given site $n$ of sublattice A. We note as well that the inverse term where site $m$ is of sublattice A and site $n$ is of sublattice B is equal to $t_{\text{e-ph}}(-\mathbf{k}-\mathbf{G})$. Defining $\psi_{\mathbf{k}} = (c_{\mathrm{A},\mathbf{k}}, c_{\mathrm{B},\mathbf{k}})^{\mathrm{t}}$, we obtain a matrix representation of the interaction hamiltonian $\mathcal{H}_{\text{e-ph}} = a^\dagger \int_{BZ} \psi^\dagger_{\mathbf{k}} h_{\text{e-ph}}(\mathbf{k}) \psi_{\mathbf{k}-\mathbf{G}} + \text{h.c.}$, with

$$h_{\text{e-ph}}(\mathbf{k}) = \begin{pmatrix} 0 & t_{\text{e-ph}}(-\mathbf{k}-\mathbf{G}) \\ t_{\text{e-ph}}(\mathbf{k}) & 0 \end{pmatrix} \ . \tag{4.11}$$

The hamiltonian considers non-vertical electronic transitions in the full BZ, however, we may develop a zone folding scheme where the system presents only vertical transitions in a reduced BZ (rBZ) as follows: We partition the BZ into zones A, B and C as depicted in Fig. 4.2, corresponding to the Voronoi decomposition with respect to points $\Gamma$, $\mathbf{G} = K^+$ and $-\mathbf{G} = K^-$, where all Voronoi cells present the same geometry. We fold zones B and C into zone A, which correspond to the rBZ, expressing the BZ zone integration as

$$\begin{aligned} \int_{\mathrm{BZ}} \mathrm{d}^2k f(\mathbf{k}) &= \left( \int_{\mathrm{A}} \mathrm{d}^2k + \int_{\mathrm{B}} \mathrm{d}^2k \int_{\mathrm{C}} \mathrm{d}^2k \right) f(\mathbf{k}) \\ &= \int_{\mathrm{rBZ}} f(\mathbf{k}) + f(\mathbf{k}+\mathbf{G}) + f(\mathbf{k}-\mathbf{G}) \ . \end{aligned} \tag{4.12}$$

We now define $\Psi_{\mathbf{k}} = (\psi^{\mathrm{t}}_{\mathbf{k}}, \psi^{\mathrm{t}}_{\mathbf{k}+\mathbf{G}}, \psi^{\mathrm{t}}_{\mathbf{k}-\mathbf{G}})^{\mathrm{t}}$, obtaining a matrix hamiltonian with vertical transitions in the rBZ, $\mathcal{H}_{\text{e-ph}} = a^\dagger \int_{\mathrm{rBZ}} \Psi^\dagger_{\mathbf{k}} H_{\text{e-ph}}(\mathbf{k}) \Psi_{\mathbf{k}} + \text{h.c.}$, with

$$H_{\text{e-ph}} = \begin{pmatrix} 0 & h_{\text{e-ph}}(\mathbf{k}) & 0 \\ 0 & 0 & h_{\text{e-ph}}(\mathbf{k}+\mathbf{G}) \\ h_{\text{e-ph}}(\mathbf{k}-\mathbf{G}) & 0 & 0 \end{pmatrix} \ . \tag{4.13}$$

In this basis the electronic hamiltonian is $\mathcal{H}_{\mathrm{e}} = \int_{\mathrm{rBZ}} \Psi^\dagger_{\mathbf{k}} H_{\mathrm{e}}(\mathbf{k}) \Psi_{\mathbf{k}}$, with

$$H_{\mathrm{e}}(\mathbf{k}) = \begin{pmatrix} h_{\mathrm{e}}(\mathbf{k}) & 0 & 0 \\ 0 & h_{\mathrm{e}}(\mathbf{k}+\mathbf{G}) & 0 \\ 0 & 0 & h_{\mathrm{e}}(\mathbf{k}-\mathbf{G}) \end{pmatrix} \ , \tag{4.14}$$

$$h_{\mathrm{e}}(\mathbf{k}) = \begin{pmatrix} \Delta & t^*_{\mathrm{e}}(\mathbf{k}) \\ t_{\mathrm{e}}(\mathbf{k}) & -\Delta \end{pmatrix} \ , \tag{4.15}$$

and $t_{\rm e}(\mathbf{k}) = \gamma_0 \sum_m \mathrm{e}^{-\mathrm{i}\mathbf{k}\cdot\mathbf{R}_{n,m}}$, where the sum runs over all sites $m$ of sublattice B which are nearest neighbor of a given site $n$ of sublattice A. The phonon hamiltonian is proportional to the identity in the electronic subspace.

We represent the phonon subspace in its Fock basis, obtaining a matrix representation for the full Hamiltonian

$$H = \begin{pmatrix} H_{\rm e} & H_{\text{e-ph}}^{\dagger} & 0 & \\ H_{\text{e-ph}} & H_{\rm e} + \hbar\omega & \sqrt{2}H_{\text{e-ph}}^{\dagger} & \\ 0 & \sqrt{2}H_{\text{e-ph}} & H_{\rm e} + 2\hbar\omega & \\ & & & \ddots \end{pmatrix} . \tag{4.16}$$

The diagonal terms in Eq. (4.16) constitute a semi-infinite series of pure electronic Hamiltonian replicas, centered at energies $n_{\rm ph}\hbar\omega$. The off-diagonal elements couple the different replcias.

## 4.6.B The low-energy approximation

The replica crossing at energy $\hbar\omega/2$ may be described truncating the full hamiltonian to both valleys in replicas $n_{\rm ph} = 0$ and $n_{\rm ph} = 1$, where only valleys $K^-$ and $K^+$ in replicas 0 and 1 respectively are coupled by the e-ph interaction. The coupling is described by the effective hamiltonian

$$\mathcal{H}_{\rm eff} = \begin{pmatrix} h_{\rm e}(\mathbf{k}-\mathbf{G}) & h_{\text{e-ph}}^{\dagger}(\mathbf{k}+\mathbf{G}) \\ h_{\text{e-ph}}(\mathbf{k}+\mathbf{G}) & h_{\rm e}(\mathbf{k}+\mathbf{G}) + \hbar\omega \end{pmatrix} . \tag{4.17}$$

For $\hbar\omega \ll \gamma_0$ we approximate the hamiltonian about the $K^{\pm}$ points, obtaining

$$h_{\rm e}(\mathbf{k}\pm\mathbf{G}) \approx \begin{pmatrix} \Delta & \mp\hbar v_{\rm F} k \mathrm{e}^{\pm\mathrm{i}\theta} \\ \mp\hbar v_{\rm F} k \mathrm{e}^{\mp\mathrm{i}\theta} & -\Delta \end{pmatrix} , \tag{4.18a}$$

$$h_{\text{e-ph}}(\mathbf{k}+\mathbf{G}) \approx \begin{pmatrix} 0 & t_1 - \mathrm{i}\mathbf{k}\cdot\mathbf{t}_2 \\ t_1 + \mathrm{i}\mathbf{k}\cdot\mathbf{t}_2 & 0 \end{pmatrix} \tag{4.18b}$$

with $\hbar v_{\rm F} = 3a_0\gamma_0/2$, $\mathbf{k} = k(\cos\theta\hat{\mathbf{x}} + \sin\theta\hat{\mathbf{y}})$, $t_1 = t_{\text{e-ph}}(\mathbf{G})$, and $\mathbf{t}_2 = -\gamma_1 \sum_m \mathrm{e}^{-\mathrm{i}\mathbf{G}\cdot\mathbf{R}_{n,m}}[\hat{\mathbf{r}}_{n,m} \cdot (\mathbf{u}_{\rm A} - \mathrm{e}^{-\mathrm{i}\mathbf{G}\cdot\mathbf{R}_{n,m}}\mathbf{u}_{\rm B})]\mathbf{R}_{n,m}$, where the sum runs over all sites $m$ of sublattice B which are nearest neighbor of a given site $n$ of sublattice A.

We rotate the basis of the hamiltonian matrix representation to the one that diagonalizes the blocks $h_{\rm e}(\mathbf{k}\pm\mathbf{G})$. The rotated hamiltonian is $\tilde{\mathcal{H}}_{\rm eff} = U^{\dagger}\mathcal{H}_{\rm eff}U$, with $U = \mathrm{diag}(U_-, U_+)$, and $U_{\pm}$ the transformation that diagonalizes $h_{\rm e}(\mathbf{k}\pm\mathbf{G})$. We truncate the space to the upper band of $n_{\rm ph} = 0$ and the lower band of $n_{\rm ph} = 1$, obtaining an effective two band model for the avoided crossing

$$\tilde{h}_{\rm eff} = \begin{pmatrix} \sqrt{\Delta^2 + (\hbar v_{\rm F} k)^2} & -\mathrm{e}^{\mathrm{i}\theta}(t_1^* - \mathrm{i}\mathbf{k}\cdot\mathbf{t}_2^*) \\ -\mathrm{e}^{-\mathrm{i}\theta}(t_1 + \mathrm{i}\mathbf{k}\cdot\mathbf{t}_2) & \hbar\omega - \sqrt{\Delta^2 + (\hbar v_{\rm F} k)^2} \end{pmatrix} . \tag{4.19}$$

Within a first approximation we may disregard the term $\mathbf{k}\cdot\mathbf{t}_2$, concluding that the coupling is uniquely determined by $t_1 = -3\mathrm{i}[\mathbf{L}^{\dagger}\mathbf{u}_{\rm A} + \mathbf{R}^{\dagger}\mathbf{u}_{\rm B}]/\sqrt{2}$. The magnitude of the gap is $2|t_1|$, which occurs for $(\hbar v_{\rm F} k)^2 = (\hbar\omega/2)^2 - \Delta^2$, and depends on the particular circular motion of each sublattice. For $\mathbf{u}_{\rm A} = \mathbf{L}$ and $\mathbf{u}_{\rm B} = \mathbf{R}$ we obtain $\mathbf{t}_2 = t_1\hat{\mathbf{y}}$, which generates a dependence of the avoided crossing on the direction of the momentum. The magnitude of the gap continues to be $2|t_1|$, which now occurs at $\theta = 0$.

## 4.6.C Berry phase

In this appendix we discuss a possible topological origin of the edge states. For this we compute the Berry phase of the pseudogap at the replica crossing. We must first have in mind that the phonon induced edge states encountered in this system are highly anomalous: They correspond to non-equilibrium, hybrid e-ph states. They propagate in the same direction at opposite borders of a ribbon, as long as the ribbon has the same geometry at both edges, while their propagation direction can be reversed when changing the ribbon geometry. They coexist with a continuum of extended states, in a system which does not present a global gap. Because of these reasons, the topological origin of the phonon induced edge states, if there is any, cannot belong to a known family of topological phases.

We pretend to give a kick-off to this discussion by computing the Berry phase of the valleys. These calculations are only meaningful for a system where processes occurring at each valley are distinguishable, allowing to truncate the system to the gapped valleys forming an effective gapped system. Let $\tilde{\chi}_\pm$ be the eigenvectors of $\tilde{h}_{\text{eff}}$ corresponding to the upper and lower band of the effective two band model. The Berry phase of each band is $\phi_\pm = \mathrm{i}\oint \chi_\pm^\dagger \nabla_{\mathbf{k}} \chi_\pm$, where the integration path is taken around the valleys, with $\nabla_{\mathbf{k}}$ the nabla operator in $\mathbf{k}$-space, and $\chi_\pm$ a representation of the corresponding eigenstates in a $\mathbf{k}$-independent basis. Note that the Berry phase is not a gauge invariant quantity, and thus can only be defined modulo $2\pi$. We have $\chi_\pm = UP\tilde{\chi}_\pm$, with $P$ such that $\tilde{h}_{\text{eff}} = P^\dagger \tilde{\mathcal{H}}_{\text{eff}} P$. We thus separate the Berry phase into two contributions, $\phi_\pm = \phi_\pm^U + \tilde{\phi}_\pm$, with $\phi_\pm^U = \mathrm{i}\oint \tilde{\chi}_\pm^\dagger P^\dagger U^\dagger \nabla_{\mathbf{k}}(UP)\tilde{\chi}_\pm$ the contribution corresponding to the basis transformation, and $\tilde{\phi}_\pm = \mathrm{i}\oint \tilde{\chi}_\pm^\dagger \tilde{\nabla}_{\mathbf{k}} \tilde{\chi}_\pm$ the contribution corresponding to bands $\tilde{\chi}_\pm$ within the rotated basis, with $\tilde{\nabla}_{\mathbf{k}}$ acting only on the elements of $\tilde{\chi}_\pm$, not on the basis.

In the case $\gamma_1 = 0$, with no e-ph interaction, the eigenvectors are $\tilde{\chi}_+ = (0,1)^{\mathrm{t}}$ and $\tilde{\chi}_- = (1,0)^{\mathrm{t}}$, for which it is evident that $\tilde{\phi}_\pm = 0$. For the basis transformation contribution we have $\phi_\pm^U = \mp\pi[1 \mp \Delta/\sqrt{\Delta^2 + (v_{\mathrm{F}}k)^2}]$, for which we have taken a circular integration path at radius $k$. In the limit $k \to \infty$ we obtain $\phi_\pm = \mp\pi$.

For $\gamma_1 \neq 0$ the eigenstates are $\tilde{\chi}_\pm = (\pm \mathrm{e}^{\mathrm{i}\delta}\sqrt{1 \pm \varepsilon}, \sqrt{1 \mp \varepsilon})/\sqrt{2}$, with $\delta = \arg[-\mathrm{e}^{\mathrm{i}\theta} t_1 (1 + \mathrm{i}k_y a_0)]$, and

$$\varepsilon = \left[1 + \left| \frac{t_1 + \mathrm{i}\mathbf{k}\cdot\mathbf{t}_2}{\sqrt{\Delta^2 + (\hbar v_{\mathrm{F}} k)^2} - \hbar\omega/2} \right|^2 \right]^{-1/2} . \tag{4.20}$$

The Berry phase is $\phi_\pm = -\pi[1 - \Delta/\sqrt{\Delta^2 + (\hbar v_{\mathrm{F}} k)^2}]$, where we conclude that the sign of the upper band has been reversed in comparison to the case with no e-ph interaction.

## 4.6.D Klein and armchair ribbons

In this appendix we include the band structure for a Klein and an armchair ribbon, shown in Fig. 4.5-(a) and (b) respectively. The Klein ribbon presents two copropagating edge states that coexist with a continuum of extended states. However, the Klein states propagate in a direction contrary to those of the zigzag ribbon. In contrast, the armchair ribbon presents no edge states at the replica crossing.

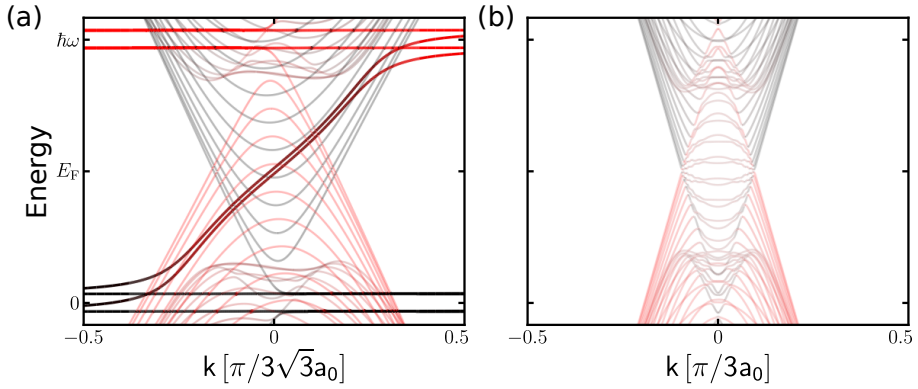


FIGURE 4.5: **(a)** Band structure of a Klein ribbon (of width $149a_0$), showing two edge states with propagation direction contrary to those of a zigzag ribbon. **(b)** Band structure of an armchair ribbon (of width $100\sqrt{3}a_0$). No edge states exist at the replica crossing. Color scale indicates the weight of the bands on $n_{\mathrm{ph}} = 0$ (black) and $n_{\mathrm{ph}} = 1$ (red), and transparency is relative to the localization.

# Conclusion

In this thesis we studied the interplay between topological phases, robust edge states, and bosonic excitations in two different investigations. The work developed here addresses the universality of topological physics, which is fundamental to wave phenomena within periodic media, the behavior of quantum features of light when coupled to a topological edge state, and the emergence of robust edge states in a phonon-driven system.

In part I we studied the propagation of squeezed states of light in a one-dimensional topological waveguide array. Chapters 1 and 2 provided to the reader a solid background on the two main areas involved, topological systems and quantum optics. In chapter 1 we developed topological band theory, at first from a solid state physics framework, and later adapted to photonic systems. In chapter 2 we developed a framework for quantum optics, focusing on squeezed states of light. In chapter 3 we presented the developed research, published in [51]. We focused on the behavior of photon statistics, one-mode and two-mode squeezing, and entanglement generation when exciting the topological edge state of a Su-Schrieffer-Heeger waveguide array, concluding that the topological phase of the lattice robustly preserves the phase of the squeezed quadrature. We performed a quantum teleportation protocol where the entangled resource is topologically protected, which serves as a proof of concept for the relevance of topological protection of quantum light.

In part II we studied the emergence of copropagating edge states in a two-dimensional material due to electron-phonon interactions with chiral phonons. The research developed in this topic, published in [58], was entirely presented in chapter 4. Chiral phonons break time reversal symmetry and introduce inelastic processes, which give rise to a phenomenology essentially different from other known broken symmetry phases, such as the quantum Hall effect. Electron-phonon interactions generate a valley selective gap, bridged by robust copropagating edge states with coexist with a continuum of the ungapped valleys. These results provide a first step in the study of the rich phenomenology derived from electron-chiral-phonon interactions.

A guiding motif of this thesis was to relate areas of physics that at first may seem unrelated. We hope that the work developed here opens more questions than it answers. Can the topology of a photonic lattice protect quantum light against other loss and decoherence processes, such as backscattering and optical losses? How does quantum light couple to more robust two-dimensional topological phases, and can a potential topological protection be harnessed for quantum information applications? What is the topological origin of the copropagating edge states encountered in part II? How does phonon chirality relate to other quantum phases?

# Bibliography


[1] Klaus von Klitzing. The quantized Hall effect. *Reviews of Modern Physics*, 58(3):519–531, 1986. doi: 10.1103/RevModPhys.58.519.

[2] Klaus von Klitzing, G. Dorda, and M. Pepper. New Method for High-Accuracy Determination of the Fine-Structure Constant Based on Quantized Hall Resistance. *Physical Review Letters*, 45(6):494–497, 1980. doi: 10.1103/PhysRevLett.45.494.

[3] Jainendra K. Jain. *Composite Fermions*. Cambridge University Press, 2007.

[4] David Tong. The quantum Hall effect, 2016. URL `https://www.damtp.cam.ac.uk/user/tong/qhe.html`. Lecture notes at Tata Institute of fundamental Research, Mumbai.

[5] D. J. Thouless, M. Kohmoto, M. P. Nightingale, and M. den Nijs. Quantized Hall Conductance in a Two-Dimensional Periodic Potential. *Physical Review Letters*, 49(6):405–408, 1982. doi: 10.1103/PhysRevLett.49.405.

[6] M. Z. Hasan and C. L. Kane. Colloquium: Topological insulators. *Reviews of Modern Physics*, 82(4):3045–3067, 2010. doi: 10.1103/RevModPhys.82.3045.

[7] Xiao-Liang Qi and Shou-Cheng Zhang. Topological insulators and superconductors. *Reviews of Modern Physics*, 83(4):1057–1110, 2011. doi: 10.1103/RevModPhys.83.1057.

[8] Ching-Kai Chiu, Jeffrey C. Y. Teo, Andreas P. Schnyder, and Shinsei Ryu. Classification of topological quantum matter with symmetries. *Reviews of Modern Physics*, 88(3):035005, 2016. doi: 10.1103/RevModPhys.88.035005.

[9] F. D. M. Haldane. Model for a Quantum Hall Effect without Landau Levels: Condensed-Matter Realization of the "Parity Anomaly". *Physical Review Letters*, 61(18):2015–2018, 1988. doi: 10.1103/PhysRevLett.61.2015.

[10] Gregor Jotzu, Michael Messer, Rémi Desbuquois, Martin Lebrat, Thomas Uehlinger, Daniel Greif, and Tilman Esslinger. Experimental realization of the topological Haldane model with ultracold fermions. *Nature*, 515(7526):237–240, November 2014. ISSN 1476-4687. doi: 10.1038/nature13915. URL `https://doi.org/10.1038/nature13915`.

[11] D. C. Tsui, H. L. Stormer, and A. C. Gossard. Two-Dimensional Magnetotransport in the Extreme Quantum Limit. *Physical Review Letters*, 48(22):1559–1562, 1982. doi:

10.1103/PhysRevLett.48.1559.

[12] R. B. Laughlin. Anomalous Quantum Hall Effect: An Incompressible Quantum Fluid with Fractionally Charged Excitations. *Physical Review Letters*, 50(18):1395–1398, 1983. doi: 10.1103/PhysRevLett.50.1395.

[13] C. L. Kane and E. J. Mele. Z2 Topological Order and the Quantum Spin Hall Effect. *Physical Review Letters*, 95(14):146802, 2005. doi: 10.1103/PhysRevLett.95.146802.

[14] B. Andrei Bernevig and Shou-Cheng Zhang. Quantum Spin Hall Effect. *Phys. Rev. Lett.*, 96(10):106802, 2006. doi: 10.1103/PhysRevLett.96.106802.

[15] Liang Fu, C. L. Kane, and E. J. Mele. Topological Insulators in Three Dimensions. *Physical Review Letters*, 98(10):106803, 2007. doi: 10.1103/PhysRevLett.98.106803.

[16] J. E. Moore and L. Balents. Topological invariants of time-reversal-invariant band structures. *Physical Review B*, 75(12):121306, 2007. doi: 10.1103/PhysRevB.75.121306.

[17] Liang Fu and C. L. Kane. Topological insulators with inversion symmetry. *Physical Review B*, 76(4):045302, 2007. doi: 10.1103/PhysRevB.76.045302.

[18] Liang Fu. Topological Crystalline Insulators. *Physical Review Letters*, 106(10):106802, 2011. doi: 10.1103/PhysRevLett.106.106802.

[19] Jianpeng Liu and David Vanderbilt. Weyl semimetals from noncentrosymmetric topological insulators. *Physical Review B*, 90(15):155316, 2014. doi: 10.1103/PhysRevB.90.155316.

[20] A. J. Heeger, S. Kivelson, J. R. Schrieffer, and W. P. Su. Solitons in conducting polymers. *Reviews of Modern Physics*, 60(3):781–850, 1988. doi: 10.1103/RevModPhys.60.781.

[21] Marcos Atala, Monika Aidelsburger, Julio T. Barreiro, Dmitry Abanin, Takuya Kitagawa, Eugene Demler, and Immanuel Bloch. Direct measurement of the Zak phase in topological Bloch bands. *Nature Physics*, 9(12):795–800, 2013. doi: 10.1038/nphys2790.

[22] C. L. Kane and E. J. Mele. Quantum Spin Hall Effect in Graphene. *Physical Review Letters*, 95(22):226801, 2005. doi: 10.1103/PhysRevLett.95.226801.

[23] B. Andrei Bernevig, Taylor L. Hughes, and Shou-Cheng Zhang. Quantum Spin Hall Effect and Topological Phase Transition in HgTe Quantum Wells. *Science*, 314(5806):1757–1761, 2006. doi: 10.1126/science.1133734.

[24] D. Hsieh, D. Qian, L. Wray, Y. Xia, Y. S. Hor, R. J. Cava, and M. Z. Hasan. A topological Dirac insulator in a quantum spin Hall phase. *Nature*, 452(7190):970–974, 2008. doi: 10.1038/nature06843.

[25] Su-Yang Xu, Ilya Belopolski, Nasser Alidoust, Madhab Neupane, Guang Bian, Chenglong Zhang, Raman Sankar, Guoqing Chang, Zhujun Yuan, Chi-Cheng Lee, Shin-Ming Huang, Hao Zheng, Jie Ma, Daniel S. Sanchez, BaoKai Wang, Arun Bansil, Fangcheng Chou,

Pavel P. Shibayev, Hsin Lin, Shuang Jia, and M. Zahid Hasan. Discovery of a Weyl fermion semimetal and topological Fermi arcs. *Science*, 349(6248):613–617, 2015. doi: 10.1126/science.aaa9297.

[26] Yaacov E. Kraus, Yoav Lahini, Zohar Ringel, Mor Verbin, and Oded Zilberberg. Topological States and Adiabatic Pumping in Quasicrystals. *Phys. Rev. Lett.*, 109(10):106402, 2012. doi: 10.1103/PhysRevLett.109.106402.

[27] V. M. Martinez Alvarez, J. E. Barrios Vargas, M. Berdakin, and L. E. F. Foa Torres. Topological states of non-Hermitian systems. *The European Physical Journal Special Topics*, 227(12):1295–1308, 2018. doi: 10.1140/epjst/e2018-800091-5.

[28] Pablo M. Pérez Piskunow. *Efectos de la radiacion en las propiedades electricas del grafeno*. PhD thesis, Universidad Nacional de Córdoba, 2015. URL `https://rdu.unc.edu.ar/handle/11086/3563`.

[29] Tomoki Ozawa, Hannah M. Price, Alberto Amo, Nathan Goldman, Mohammad Hafezi, Ling Lu, Mikael C. Rechtsman, David Schuster, Jonathan Simon, Oded Zilberberg, and Iacopo Carusotto. Topological photonics. *Reviews of Modern Physics*, 91(1):015006, 2019. doi: 10.1103/RevModPhys.91.015006.

[30] Bi-Ye Xie, Hong-Fei Wang, Xue-Yi Zhu, Ming-Hui Lu, Z. D. Wang, and Yan-Feng Chen. Photonics meets topology. *Optics Express*, 26(19):24531–24550, 2018. doi: 10.1364/OE.26.024531.

[31] Ling Lu, John D. Joannopoulos, and Marin Soljačić. Topological photonics. *Nature Photonics*, 8(11):821–829, 2014. doi: 10.1038/nphoton.2014.248.

[32] X. S. Wang, H. W. Zhang, and X. R. Wang. Topological Magnonics: A Paradigm for Spin-Wave Manipulation and Device Design. *Physical Review Applied*, 9(2):024029, 2018. doi: 10.1103/PhysRevApplied.9.024029.

[33] Sebastian D. Huber. Topological mechanics. *Nature Physics*, 12(7):621–623, 2016. doi: 10.1038/nphys3801.

[34] Ching Hua Lee, Stefan Imhof, Christian Berger, Florian Bayer, Johannes Brehm, Laurens W. Molenkamp, Tobias Kiessling, and Ronny Thomale. Topolectrical Circuits. *Communications Physics*, 1(1):39, 2018. doi: 10.1038/s42005-018-0035-2.

[35] Alexander B. Khanikaev, Romain Fleury, S. Hossein Mousavi, and Andrea Alù. Topologically robust sound propagation in an angular-momentum-biased graphene-like resonator lattice. *Nature Communications*, 6(1):8260, 2015. doi: 10.1038/ncomms9260.

[36] V. Peano, C. Brendel, M. Schmidt, and F. Marquardt. Topological Phases of Sound and Light. *Physical Review X*, 5(3):031011, 2015. doi: 10.1103/PhysRevX.5.031011.

[37] J. Eli Bourassa, Rafael N. Alexander, Michael Vasmer, Ashlesha Patil, Ilan Tzitrin, Takaya Matsuura, Daiqin Su, Ben Q. Baragiola, Saikat Guha, Guillaume Dauphinais, Krishna K.

Sabapathy, Nicolas C. Menicucci, and Ish Dhand. Blueprint for a Scalable Photonic Fault-Tolerant Quantum Computer. *Quantum*, 5:392, 2021. doi: 10.22331/q-2021-02-04-392.

[38] Mikkel V. Larsen, Xueshi Guo, Casper R. Breum, Jonas S. Neergaard-Nielsen, and Ulrik L. Andersen. Deterministic generation of a two-dimensional cluster state. *Science*, 366(6463): 369–372, 2019. doi: 10.1126/science.aay4354.

[39] Terry Rudolph. Why I am optimistic about the silicon-photonic route to quantum computing. *APL Photonics*, 2(3):030901, 2017. doi: 10.1063/1.4976737.

[40] Andrea Blanco-Redondo. Topological Nanophotonics: Toward Robust Quantum Circuits. *Proceedings of the IEEE*, 108(5):837–849, 2020. doi: 10.1109/JPROC.2019.2939987.

[41] Sunil Mittal, Venkata Vikram Orre, and Mohammad Hafezi. Topologically robust transport of entangled photons in a 2D photonic system. *Optics Express*, 24(14):15631–15641, 2016. doi: 10.1364/OE.24.015631.

[42] Mikael C. Rechtsman, Yaakov Lumer, Yonatan Plotnik, Armando Perez-Leija, Alexander Szameit, and Mordechai Segev. Topological protection of photonic path entanglement. *Optica*, 3(9):925–930, 2016. doi: 10.1364/OPTICA.3.000925.

[43] Christian Weedbrook, Stefano Pirandola, Raúl García-Patrón, Nicolas J. Cerf, Timothy C. Ralph, Jeffrey H. Shapiro, and Seth Lloyd. Gaussian quantum information. *Reviews of Modern Physics*, 84(2):621–669, 2012. doi: 10.1103/RevModPhys.84.621.

[44] Samuel L. Braunstein and Peter van Loock. Quantum information with continuous variables. *Reviews of Modern Physics*, 77(2):513–577, 2005. doi: 10.1103/RevModPhys.77.513.

[45] Jeremy L. O'Brien, Akira Furusawa, and Jelena Vučković. Photonic quantum technologies. *Nature Photonics*, 3(12):687–695, 2009. doi: 10.1038/nphoton.2009.229.

[46] Fulvio Flamini, Nicolò Spagnolo, and Fabio Sciarrino. Photonic quantum information processing: a review. *Reports on Progress in Physics*, 82(1):016001, 2018. doi: 10.1088/1361-6633/aad5b2.

[47] Sergei Slussarenko and Geoff J. Pryde. Photonic quantum information processing: A concise review. *Applied Physics Reviews*, 6(4):041303, 2019. doi: 10.1063/1.5115814.

[48] Sunil Mittal, Elizabeth A. Goldschmidt, and Mohammad Hafezi. A topological source of quantum light. *Nature*, 561(7724):502–506, 2018. doi: 10.1038/s41586-018-0478-3.

[49] Andrea Blanco-Redondo, Bryn Bell, Dikla Oren, Benjamin J. Eggleton, and Mordechai Segev. Topological protection of biphoton states. *Science*, 362(6414):568–571, 2018. doi: 10.1126/science.aau4296.

[50] Michelle Wang, Cooper Doyle, Bryn Bell, Matthew J. Collins, Eric Magi, Benjamin J. Eggleton, Mordechai Segev, and Andrea Blanco-Redondo. Topologically protected en-

tangled photonic states. *Nanophotonics*, 8(8):1327–1335, 2019. doi: doi:10.1515/nanoph-2019-0058.

[51] Joaquin Medina Dueñas, Gabriel O'Ryan Pérez, Carla Hermann-Avigliano, and Luis E. F. Foa Torres. Quadrature protection of squeezed states in a one-dimensional photonic topological insulator. *Quantum*, 5:526, 2021. doi: 10.22331/q-2021-08-17-526.

[52] W. P. Su, J. R. Schrieffer, and A. J. Heeger. Solitons in Polyacetylene. *Physical Review Letters*, 42(25):1698–1701, 1979. doi: 10.1103/PhysRevLett.42.1698.

[53] W. P. Su, J. R. Schrieffer, and A. J. Heeger. Soliton excitations in polyacetylene. *Physical Review B*, 22(4):2099–2111, 1980. doi: 10.1103/PhysRevB.22.2099.

[54] Natalia Malkova, Ivan Hromada, Xiaosheng Wang, Garnett Bryant, and Zhigang Chen. Observation of optical Shockley-like surface states in photonic superlattices. *Optics Letters*, 34(11):1633–1635, 2009. doi: 10.1364/OL.34.001633.

[55] Netanel H. Lindner, Gil Refael, and Victor Galitski. Floquet topological insulator in semiconductor quantum wells. *Nature Physics*, 7(6):490–495, 2011. doi: 10.1038/nphys1926.

[56] Gonzalo Usaj, P. M. Perez-Piskunow, L. E. F. Foa Torres, and C. A. Balseiro. Irradiated graphene as a tunable Floquet topological insulator. *Physical Review B*, 90(11):115423, 2014. doi: 10.1103/PhysRevB.90.115423.

[57] Jin-Yu Zou and Bang-Gui Liu. Floquet Weyl fermions in three-dimensional stacked graphene systems irradiated by circularly polarized light. *Physical Review B*, 93(20): 205435, 2016. doi: 10.1103/PhysRevB.93.205435.

[58] Joaquín Medina Dueñas, Hernán L. Calvo, and Luis E. F. Foa Torres. To be published.

[59] J. Bardeen. Electron-Vibration Interactions and Superconductivity. *Reviews of Modern Physics*, 23(3):261–270, 1951. doi: 10.1103/RevModPhys.23.261.

[60] Herbert Fröhlich. On the theory of superconductivity: the one-dimensional case. *Proceedings of the Royal Society of London. Series A. Mathematical and Physical Sciences*, 223 (1154):296–305, 1954. doi: 10.1098/rspa.1954.0116. Publisher: Royal Society.

[61] Michael Tinkham. *Introduction to Superconductivity*. Dover Publications, second edition edition, 2004.

[62] Hernán L. Calvo, Javier S. Luna, Virginia Dal Lago, and Luis E. F. Foa Torres. Robust edge states induced by electron-phonon interaction in graphene nanoribbons. *Physical Review B*, 98(3):035423, 2018. doi: 10.1103/PhysRevB.98.035423.

[63] Hannes Hübener, Umberto De Giovannini, and Angel Rubio. Phonon Driven Floquet Matter. *Nano Letters*, 18(2):1535–1542, 2018. doi: 10.1021/acs.nanolett.7b05391.

[64] Swati Chaudhary, Arbel Haim, Yang Peng, and Gil Refael. Phonon-induced Floquet

topological phases protected by space-time symmetries. *Physical Review Research*, 2(4): 043431, 2020. doi: 10.1103/PhysRevResearch.2.043431.

[65] Lifa Zhang and Qian Niu. Chiral Phonons at High-Symmetry Points in Monolayer Hexagonal Lattices. *Physical Review Letters*, 115(11):115502, 2015. doi: 10.1103/PhysRevLett.115.115502.

[66] Hanyu Zhu, Jun Yi, Ming-Yang Li, Jun Xiao, Lifa Zhang, Chih-Wen Yang, Robert A. Kaindl, Lain-Jong Li, Yuan Wang, and Xiang Zhang. Observation of chiral phonons. *Science*, 359(6375):579–582, 2018. doi: 10.1126/science.aar2711.

[67] Yizhou Liu, Chao-Sheng Lian, Yang Li, Yong Xu, and Wenhui Duan. Pseudospins and Topological Effects of Phonons in a Kekulé Lattice. *Physical Review Letters*, 119(25): 255901, 2017. doi: 10.1103/PhysRevLett.119.255901.

[68] Mengnan Gao, Wei Zhang, and Lifa Zhang. Nondegenerate Chiral Phonons in Graphene/Hexagonal Boron Nitride Heterostructure from First-Principles Calculations. *Nano Letters*, 18(7):4424–4430, 2018. doi: 10.1021/acs.nanolett.8b01487.

[69] Xifang Xu, Hao Chen, and Lifa Zhang. Nondegenerate chiral phonons in the Brillouin-zone center of $\sqrt{3}\ifmmode\times\else\textimes\fi\sqrt{3}$ honeycomb superlattices. *Phys. Rev. B*, 98(13):134304, 2018. doi: 10.1103/PhysRevB.98.134304.

[70] Hao Chen, Weikang Wu, Shengyuan A. Yang, Xiao Li, and Lifa Zhang. Chiral phonons in kagome lattices. *Physical Review B*, 100(9):094303, 2019. doi: 10.1103/PhysRevB.100.094303.

[71] Hao Chen, Weikang Wu, Jiaojiao Zhu, Shengyuan A. Yang, and Lifa Zhang. Propagating Chiral Phonons in Three-Dimensional Materials. *Nano Letters*, 21(7):3060–3065, 2021. doi: 10.1021/acs.nanolett.1c00236.

[72] Klaus von Klitzing. Developments in the quantum Hall effect. *Philosophical Transactions of the Royal Society A*, 363(1834):2203–2219, 2005. doi: 10.1098/rsta.2005.1640.

[73] Jose Chesta Lopez. *Transport properties of Weyl semimetals*. PhD thesis, Universidad de Chile, 2019. URL `http://repositorio.uchile.cl/handle/2250/173793`.

[74] Michel Fruchart and David Carpentier. An introduction to topological insulators. *Comptes Rendus Physique*, 14(9):779–815, 2013. doi: https://doi.org/10.1016/j.crhy.2013.09.013.

[75] M. Nakahara. *Geometry, Topology and Physics*. Graduate student series in physics. Institute of Physics Publishing, second edition edition, 2003.

[76] Chen Fang, Hongming Weng, Xi Dai, and Zhong Fang. Topological nodal line semimetals. *Chinese Physics B*, 25(11):117106, 2016. doi: 10.1088/1674-1056/25/11/117106.

[77] Shunji Matsuura, Po-Yao Chang, Andreas P. Schnyder, and Shinsei Ryu. Protected boundary states in gapless topological phases. *New Journal of Physics*, 15(6):065001,

2013. doi: 10.1088/1367-2630/15/6/065001.

[78] Oskar Vafek and Ashvin Vishwanath. Dirac Fermions in Solids: From High-Tc Cuprates and Graphene to Topological Insulators and Weyl Semimetals. *Annual Review of Condensed Matter Physics*, 5(1):83–112, 2014. doi: 10.1146/annurev-conmatphys-031113-133841.

[79] Xiao-Liang Qi, Yong-Shi Wu, and Shou-Cheng Zhang. General theorem relating the bulk topological number to edge states in two-dimensional insulators. *Physical Review B*, 74 (4):045125, 2006. doi: 10.1103/PhysRevB.74.045125.

[80] Congjun Wu, B. Andrei Bernevig, and Shou-Cheng Zhang. Helical Liquid and the Edge of Quantum Spin Hall Systems. *Physical Review Letters*, 96(10):106401, 2006. doi: 10.1103/PhysRevLett.96.106401.

[81] Markus König, Steffen Wiedmann, Christoph Brüne, Andreas Roth, Hartmut Buhmann, Laurens W. Molenkamp, Xiao-Liang Qi, and Shou-Cheng Zhang. Quantum Spin Hall Insulator State in HgTe Quantum Wells. *Science*, 318(5851):766–770, 2007. doi: 10.1126/science.1148047.

[82] Rudolph Peierls. *Quantum Theory of Solids*. Oxford classical texts in the physical sciences. Oxford University Press, 1955.

[83] J. Zak. Berry's phase for energy bands in solids. *Physical Review Letters*, 62(23):2747–2750, 1989. doi: 10.1103/PhysRevLett.62.2747.

[84] Marcos Atala. *Measuring topological invariants and chiral Meissner currents with ultracold bosonic atoms*. PhD thesis, Ludwig-Maximilians-Universität München, 2014. URL `https://edoc.ub.uni-muenchen.de/17735/`.

[85] M. J. Rice and E. J. Mele. Elementary Excitations of a Linearly Conjugated Diatomic Polymer. *Physical Review Letters*, 49(19):1455–1459, 1982. doi: 10.1103/PhysRevLett.49.1455.

[86] János K. Asbóth, Lázló Oroszlány, and András P. Pályi. *A Short Course on Topological Insulators: Band Structure and Edge States in One and Two Dimensions*. Lecture Notes in Physics. Springer International Publishing, 2016.

[87] J.D. Joannopoulos, S.G. Johnson, J.N. Winn, and R.D. Meade. *Photonic Crystals: Molding the Flow of Light*. Princeton University Press, 2008.

[88] Mikael C. Rechtsman, Julia M. Zeuner, Yonatan Plotnik, Yaakov Lumer, Daniel Podolsky, Felix Dreisow, Stefan Nolte, Mordechai Segev, and Alexander Szameit. Photonic Floquet topological insulators. *Nature*, 496(7444):196–200, 2013. doi: 10.1038/nature12066.

[89] Mário G. Silveirinha. Chern invariants for continuous media. *Physical Review B*, 92(12):125153, 2015. doi: 10.1103/PhysRevB.92.125153.

[90] Mohammad Hafezi, Eugene A. Demler, Mikhail D. Lukin, and Jacob M. Taylor. Robust optical delay lines with topological protection. *Nature Physics*, 7(11):907–912, 2011. doi: 10.1038/nphys2063.

[91] K. G. Makris, R. El-Ganainy, D. N. Christodoulides, and Z. H. Musslimani. Beam Dynamics in $\mathcalP\mathcalT$ Symmetric Optical Lattices. *Physical Review Letters*, 100(10):103904, 2008. doi: 10.1103/PhysRevLett.100.103904.

[92] Z. H. Musslimani, K. G. Makris, R. El-Ganainy, and D. N. Christodoulides. Optical Solitons in PT Periodic Potentials. *Physical Review Letters*, 100(3):030402, 2008. doi: 10.1103/PhysRevLett.100.030402.

[93] Aaswath Raman and Shanhui Fan. Photonic Band Structure of Dispersive Metamaterials Formulated as a Hermitian Eigenvalue Problem. *Physical Review Letters*, 104(8):087401, 2010. doi: 10.1103/PhysRevLett.104.087401.

[94] S. Weimann, M. Kremer, Y. Plotnik, Y. Lumer, S. Nolte, K. G. Makris, M. Segev, M. C. Rechtsman, and A. Szameit. Topologically protected bound states in photonic parity–time-symmetric crystals. *Nature Materials*, 16(4):433–438, 2017. doi: 10.1038/nmat4811.

[95] Zheng Wang, Yidong Chong, J. D. Joannopoulos, and Marin Soljačić. Observation of unidirectional backscattering-immune topological electromagnetic states. *Nature*, 461(7265): 772–775, 2009. doi: 10.1038/nature08293.

[96] Zhuoyuan Wang, Linfang Shen, Xianmin Zhang, Yigang Wang, Zaihe Yu, and Xiaodong Zheng. Photonic crystal cavity with one-way rotating state and its coupling with photonic crystal waveguide. *Journal of Applied Physics*, 110(4):043106, 2011. doi: 10.1063/1.3622676.

[97] Jin-Xin Fu, Rong-Juan Liu, and Zhi-Yuan Li. Robust one-way modes in gyromagnetic photonic crystal waveguides with different interfaces. *Applied Physics Letters*, 97(4):041112, 2010. doi: 10.1063/1.3470873.

[98] Mohammad Hafezi, Sunil Mittal, J. Fan, A. Migdall, and J. M. Taylor. Imaging topological edge states in silicon photonics. *Nature Photonics*, 7(12):1001–1005, 2013. doi: 10.1038/nphoton.2013.274.

[99] Meng Xiao, Z. Q. Zhang, and C. T. Chan. Surface Impedance and Bulk Band Geometric Phases in One-Dimensional Systems. *Physical Review X*, 4(2):021017, 2014. doi: 10.1103/PhysRevX.4.021017.

[100] Andrea Blanco-Redondo, Imanol Andonegui, Matthew J. Collins, Gal Harari, Yaakov Lumer, Mikael C. Rechtsman, Benjamin J. Eggleton, and Mordechai Segev. Topological Optical Waveguiding in Silicon and the Transition between Topological and Trivial Defect States. *Physical Review Letters*, 116(16):163901, 2016. doi: 10.1103/PhysRevLett.116.163901.

[101] H.A. Haus and W. Huang. Coupled-mode theory. *Proceedings of the IEEE*, 79(10):1505–1518, 1991. doi: 10.1109/5.104225.

[102] Mehmet Bayindir, B. Temelkuran, and E. Ozbay. Tight-Binding Description of the Coupled Defect Modes in Three-Dimensional Photonic Crystals. *Physical Review Letters*, 84 (10):2140–2143, 2000. doi: 10.1103/PhysRevLett.84.2140.

[103] Amnon Yariv, Yong Xu, Reginald K. Lee, and Axel Scherer. Coupled-resonator optical waveguide:?a proposal and analysis. *Optics Letters*, 24(11):711–713, 1999. doi: 10.1364/OL.24.000711.

[104] Neil W. Ashcroft and N. David Mermin. *Solid State Physics*. Harcourt College Publishers, 1976.

[105] Jeremy L. O'Brien. Optical Quantum Computing. *Science*, 318(5856):1567–1570, 2007. doi: 10.1126/science.1142892.

[106] Gerardo Adesso and Fabrizio Illuminati. Entanglement in continuous-variable systems: recent advances and current perspectives. *Journal of Physics A*, 40(28):7821–7880, 2007. doi: 10.1088/1751-8113/40/28/s01.

[107] A. Ferraro, S. Olivares, and Matteo G. A. Paris. *Gaussian States in Quantum Information*. Napoli Series on physics and Astrophysics. Bibliopolis, 2005.

[108] M. Uria, P. Solano, and C. Hermann-Avigliano. Deterministic Generation of Large Fock States. *Physical Review Letters*, 125(9):093603, 2020. doi: 10.1103/PhysRevLett.125.093603.

[109] Caspar Groiseau, Alexander E. J. Elliott, Stuart J. Masson, and Scott Parkins. Proposal for a Deterministic Single-Atom Source of Quasisuperradiant $N$-Photon Pulses. *Physical Review Letters*, 127(3):033602, 2021. doi: 10.1103/PhysRevLett.127.033602.

[110] Clément Sayrin, Igor Dotsenko, Xingxing Zhou, Bruno Peaudecerf, Théo Rybarczyk, Sébastien Gleyzes, Pierre Rouchon, Mazyar Mirrahimi, Hadis Amini, Michel Brune, Jean-Michel Raimond, and Serge Haroche. Real-time quantum feedback prepares and stabilizes photon number states. *Nature*, 477(7362):73–77, 2011. doi: 10.1038/nature10376.

[111] Samuel Deléglise, Igor Dotsenko, Clément Sayrin, Julien Bernu, Michel Brune, Jean-Michel Raimond, and Serge Haroche. Reconstruction of non-classical cavity field states with snapshots of their decoherence. *Nature*, 455(7212):510–514, 2008. doi: 10.1038/nature07288.

[112] M.O. Scully and M.S. Zubairy. *Quantum Optics*. Cambridge University Press, 1997.

[113] Christopher Gerry and Peter Knight. *Introductory Quantum Optics*. Cambridge University Press, 2004.

[114] Carla Hermann Hermann Avigliano. *Towards deterministic preparation of single Ry-*

*dberg atoms and applications to quantum information processing*. PhD thesis, Université Pierre et Marie Curie - Paris VI ; Universidad de Concepción, 2014. URL `https://tel.archives-ouvertes.fr/tel-01165050`.

[115] R. Simon, N. Mukunda, and Biswadeb Dutta. Quantum-noise matrix for multimode systems: U(n) invariance, squeezing, and normal forms. *Physical Review A*, 49(3):1567–1583, 1994. doi: 10.1103/PhysRevA.49.1567.

[116] R. Simon. Peres-Horodecki Separability Criterion for Continuous Variable Systems. *Physical Review Letters*, 84(12):2726–2729, 2000. doi: 10.1103/PhysRevLett.84.2726.

[117] Asher Peres. Separability Criterion for Density Matrices. *Physical Review Letters*, 77(8): 1413–1415, 1996. doi: 10.1103/PhysRevLett.77.1413.

[118] Mitsuyoshi Yukawa, Hugo Benichi, and Akira Furusawa. High-fidelity continuous-variable quantum teleportation toward multistep quantum operations. *Physical Review A*, 77(2): 022314, 2008. doi: 10.1103/PhysRevA.77.022314.

[119] Mikkel V. Larsen, Christopher Chamberland, Kyungjoo Noh, Jonas S. Neergaard-Nielsen, and Ulrik L. Andersen. A fault-tolerant continuous-variable measurement-based quantum computation architecture, 2021. arXiv preprint arxiv:2101.03014.

[120] Carlton M. Caves. Quantum-mechanical noise in an interferometer. *Physical Review D*, 23(8):1693–1708, 1981. doi: 10.1103/PhysRevD.23.1693.

[121] J. Aasi and the LIGO Scientific Collaboration. Enhanced sensitivity of the LIGO gravitational wave detector by using squeezed states of light. *Nature Photonics*, 7(8):613–619, August 2013. doi: 10.1038/nphoton.2013.177.

[122] Vittorio Giovannetti, Seth Lloyd, and Lorenzo Maccone. Quantum-Enhanced Measurements: Beating the Standard Quantum Limit. *Science*, 306(5700):1330–1336, 2004. doi: 10.1126/science.1104149.

[123] S.M. Barnett, C. Fabre, and A. Maıtre. Ultimate quantum limits for resolution of beam displacements. *The European Physical Journal D*, 22(3):513–519, 2003. doi: 10.1140/epjd/e2003-00003-3.

[124] Roy S. Bondurant and Jeffrey H. Shapiro. Squeezed states in phase-sensing interferometers. *Physical Review D*, 30(12):2548–2556, 1984. doi: 10.1103/PhysRevD.30.2548.

[125] Min Xiao, Ling-An Wu, and H. J. Kimble. Precision measurement beyond the shot-noise limit. *Physical Review Letters*, 59(3):278–281, 1987. doi: 10.1103/PhysRevLett.59.278.

[126] A. F. Pace, M. J. Collett, and D. F. Walls. Quantum limits in interferometric detection of gravitational radiation. *Physical Review A*, 47(4):3173–3189, 1993. doi: 10.1103/PhysRevA.47.3173.

[127] P. Grangier, R. E. Slusher, B. Yurke, and A. LaPorta. Squeezed-light–enhanced polar-

ization interferometer. *Physical Review Letters*, 59(19):2153–2156, 1987. doi: 10.1103/PhysRevLett.59.2153.

[128] J. Aasi and the LIGO Scientific Collaboration. Advanced LIGO. *Classical and Quantum Gravity*, 32(7):074001, 2015. doi: 10.1088/0264-9381/32/7/074001.

[129] B. J. Lawrie, P. D. Lett, A. M. Marino, and R. C. Pooser. Quantum Sensing with Squeezed Light. *ACS Photonics*, 6(6):1307–1318, 2019. doi: 10.1021/acsphotonics.9b00250.

[130] Mikhail I. Kolobov and Claude Fabre. Quantum Limits on Optical Resolution. *Physical Review Letters*, 85(18):3789–3792, 2000. doi: 10.1103/PhysRevLett.85.3789.

[131] A. Einstein, B. Podolsky, and N. Rosen. Can Quantum-Mechanical Description of Physical Reality Be Considered Complete? *Physical Review*, 47(10):777–780, 1935. doi: 10.1103/PhysRev.47.777.

[132] Han Zhao, Pei Miao, Mohammad H. Teimourpour, Simon Malzard, Ramy El-Ganainy, Henning Schomerus, and Liang Feng. Topological hybrid silicon microlasers. *Nature Communications*, 9(1):981, 2018. doi: 10.1038/s41467-018-03434-2. URL `https://doi.org/10.1038/s41467-018-03434-2`.

[133] P. St-Jean, V. Goblot, E. Galopin, A. Lemaître, T. Ozawa, L. Le Gratiet, I. Sagnes, J. Bloch, and A. Amo. Lasing in topological edge states of a one-dimensionallattice. *Nature Photonics*, 11(10):651–656, 2017. doi: 10.1038/s41566-017-0006-2.

[134] Vittorio Peano, Martin Houde, Florian Marquardt, and Aashish A. Clerk. Topological Quantum Fluctuations and Traveling Wave Amplifiers. *Physical Review X*, 6(4):041026, 2016. doi: 10.1103/PhysRevX.6.041026.

[135] Clara C. Wanjura, Matteo Brunelli, and Andreas Nunnenkamp. Topological framework for directional amplification in driven-dissipative cavity arrays. *Nature Communications*, 11(1):3149, 2020. doi: 10.1038/s41467-020-16863-9.

[136] Takuya Kitagawa, Matthew A. Broome, Alessandro Fedrizzi, Mark S. Rudner, Erez Berg, Ivan Kassal, Alán Aspuru-Guzik, Eugene Demler, and Andrew G. White. Observation of topologically protected bound states in photonic quantum walks. *Nature Communications*, 3(1):882, 2012. doi: 10.1038/ncomms1872.

[137] Sabyasachi Barik, Aziz Karasahin, Christopher Flower, Tao Cai, Hirokazu Miyake, Wade DeGottardi, Mohammad Hafezi, and Edo Waks. A topological quantum optics interface. *Science*, 359(6376):666–668, 2018. doi: 10.1126/science.aaq0327.

[138] Jean-Luc Tambasco, Giacomo Corrielli, Robert J. Chapman, Andrea Crespi, Oded Zilberberg, Roberto Osellame, and Alberto Peruzzo. Quantum interference of topological states of light. *Science Advances*, 4(9), 2018. doi: 10.1126/sciadv.aat3187.

[139] Yao Wang, Xiao-Ling Pang, Yong-Heng Lu, Jun Gao, Yi-Jun Chang, Lu-Feng Qiao, Zhi-Qiang Jiao, Hao Tang, and Xian-Min Jin. Topological protection of two-photon quantum

correlation on a photonic chip. *Optica*, 6(8):955–960, 2019. doi: 10.1364/OPTICA.6.000955.

[140] L. Xiao, X. Zhan, Z. H. Bian, K. K. Wang, X. Zhang, X. P. Wang, J. Li, K. Mochizuki, D. Kim, N. Kawakami, W. Yi, H. Obuse, B. C. Sanders, and P. Xue. Observation of topological edge states in parity–time-symmetric quantum walks. *Nature Physics*, 13(11):1117–1123, 2017. doi: 10.1038/nphys4204.

[141] Filippo Cardano, Maria Maffei, Francesco Massa, Bruno Piccirillo, Corrado de Lisio, Giulio De Filippis, Vittorio Cataudella, Enrico Santamato, and Lorenzo Marrucci. Statistical moments of quantum-walk dynamics reveal topological quantum transitions. *Nature Communications*, 7(1):11439, 2016. doi: 10.1038/ncomms11439.

[142] Chao Chen, Xing Ding, Jian Qin, Yu He, Yi-Han Luo, Ming-Cheng Chen, Chang Liu, Xi-Lin Wang, Wei-Jun Zhang, Hao Li, Li-Xing You, Zhen Wang, Da-Wei Wang, Barry C. Sanders, Chao-Yang Lu, and Jian-Wei Pan. Observation of Topologically Protected Edge States in a Photonic Two-Dimensional Quantum Walk. *Physical Review Letters*, 121(10):100502, 2018. doi: 10.1103/PhysRevLett.121.100502.

[143] Yao Wang, Yong-Heng Lu, Feng Mei, Jun Gao, Zhan-Ming Li, Hao Tang, Shi-Liang Zhu, Suotang Jia, and Xian-Min Jin. Direct Observation of Topology from Single-Photon Dynamics. *Physical Review Letters*, 122(19):193903, 2019. doi: 10.1103/PhysRevLett.122.193903.

[144] Yao Wang, Yong-Heng Lu, Jun Gao, Ruo-Jing Ren, Yi-Jun Chang, Zhi-Qiang Jiao, Zhe-Yong Zhang, and Xian-Min Jin. Topologically Protected Quantum Entanglement, 2019. arXiv preprint arXiv:1903.03015.

[145] Vittorio Peano, Martin Houde, Christian Brendel, Florian Marquardt, and Aashish A. Clerk. Topological phase transitions and chiral inelastic transport induced by the squeezing of light. *Nature Communications*, 7(1):10779, 2016. doi: 10.1038/ncomms10779.

[146] Daniel Gottesman, Alexei Kitaev, and John Preskill. Encoding a qubit in an oscillator. *Phys. Rev. A*, 64(1):012310, 2001. doi: 10.1103/PhysRevA.64.012310.

[147] Nicolas C. Menicucci, Peter van Loock, Mile Gu, Christian Weedbrook, Timothy C. Ralph, and Michael A. Nielsen. Universal Quantum Computation with Continuous-Variable Cluster States. *Physical Review Letters*, 97(11):110501, 2006. doi: 10.1103/PhysRevLett.97.110501.

[148] Samuel L. Braunstein and H. J. Kimble. Teleportation of Continuous Quantum Variables. *Physical Review Letters*, 80(4):869–872, 1998. doi: 10.1103/PhysRevLett.80.869.

[149] Alexander Franzen, Boris Hage, James DiGuglielmo, Jaromír Fiurášek, and Roman Schnabel. Experimental Demonstration of Continuous Variable Purification of Squeezed States. *Physical Review Letters*, 97(15):150505, 2006. doi: 10.1103/PhysRevLett.97.150505.

[150] Yuishi Takeno, Mitsuyoshi Yukawa, Hidehiro Yonezawa, and Akira Furusawa. Observa-

tion of -9 dB quadrature squeezing with improvement of phase stability in homodyne measurement. *Optics Express*, 15(7):4321–4327, 2007. doi: 10.1364/OE.15.004321.

[151] Henning Vahlbruch, Moritz Mehmet, Simon Chelkowski, Boris Hage, Alexander Franzen, Nico Lastzka, Stefan Goßler, Karsten Danzmann, and Roman Schnabel. Observation of Squeezed Light with 10-dB Quantum-Noise Reduction. *Physical Review Letters*, 100(3): 033602, 2008. doi: 10.1103/PhysRevLett.100.033602.

[152] Fu Li, Tian Li, and Girish S. Agarwal. Experimental study of decoherence of the two-mode squeezed vacuum state via second harmonic generation, 2020. arxiv preprint arxiv:2012.11839.

[153] Ruo-Jing Ren, Yong-Heng Lu, Ze-Kun Jiang, Jun Gao, Wen-Hao Zhou, Yao Wang, Zhi-Qiang Jiao, Xiao-Wei Wang, Alexander S. Solntsev, and Xian-Min Jin. Topologically Protecting Squeezed Light on a Photonic Chip, 2021. arXiv preprint arxiv:2106.07425.

[154] P. W. Bridgman. The Electrical Resistance of Metals. *Physical Review*, 17(2):161–194, 1921. doi: 10.1103/PhysRev.17.161.

[155] R. Peierls. Zur Theorie der elektrischen und thermischen Leitfähigkeit von Metallen. *Annalen der Physik*, 396(2):121–148, 1930. doi: https://doi.org/10.1002/andp.19303960202.

[156] J. M. Ziman. *Electrons and phonons: the theory of transport phenomena in solids*. Oxford University Press, 2001.

[157] Lawrence Challis. *Electron-phonon interactions in low-dimensional structures*. Oxford University Press, 2003.

[158] Ge. G. Samsonidze, E. B. Barros, R. Saito, J. Jiang, G. Dresselhaus, and M. S. Dresselhaus. Electron-phonon coupling mechanism in two-dimensional graphite and single-wall carbon nanotubes. *Physical Review B*, 75(15):155420, 2007. doi: 10.1103/PhysRevB.75.155420.

[159] Jia-An Yan, Ryan Stein, David M. Schaefer, Xiao-Qian Wang, and M. Y. Chou. Electron-phonon coupling in two-dimensional silicene and germanene. *Physical Review B*, 88(12): 121403, 2013. doi: 10.1103/PhysRevB.88.121403.

[160] Tue Gunst, Troels Markussen, Kurt Stokbro, and Mads Brandbyge. First-principles method for electron-phonon coupling and electron mobility: Applications to two-dimensional materials. *Physical Review B*, 93(3):035414, January 2016. doi: 10.1103/PhysRevB.93.035414.

[161] Manfred Ersfeld, Frank Volmer, Pedro Miguel M. C. de Melo, Robin de Winter, Maximilian Heithoff, Zeila Zanolli, Christoph Stampfer, Matthieu J. Verstraete, and Bernd Beschoten. Spin States Protected from Intrinsic Electron–Phonon Coupling Reaching 100 ns Lifetime at Room Temperature in MoSe2. *Nano Letters*, 19(6):4083–4090, 2019. doi: 10.1021/acs.nanolett.9b01485.

[162] H. Fröhlich. Theory of the Superconducting State. I. The Ground State at the Absolute Zero of Temperature. *Physical Review*, 79(5):845–856, 1950. doi: 10.1103/PhysRev.79.845.

[163] Rudolph Peierls. *More surprises in theoretical physics*. Princeton Series in Physics. Princeton University Press, 1992.

[164] Luis E. F. Foa Torres and Stephan Roche. Inelastic Quantum Transport and Peierls-Like Mechanism in Carbon Nanotubes. *Physical Review Letters*, 97(7):076804, 2006. doi: 10.1103/PhysRevLett.97.076804.

[165] Luis E. F. Foa Torres, Rémi Avriller, and Stephan Roche. Nonequilibrium energy gaps in carbon nanotubes: Role of phonon symmetries. *Physical Review B*, 78(3):035412, 2008. doi: 10.1103/PhysRevB.78.035412.

[166] G. Grissonnanche, S. Thériault, A. Gourgout, M.-E. Boulanger, E. Lefrançois, A. Ataei, F. Laliberté, M. Dion, J.-S. Zhou, S. Pyon, T. Takayama, H. Takagi, N. Doiron-Leyraud, and L. Taillefer. Chiral phonons in the pseudogap phase of cuprates. *Nature Physics*, 16 (11):1108–1111, 2020. doi: 10.1038/s41567-020-0965-y.

[167] A. de la Torre, K. L. Seyler, L. Zhao, S. Di Matteo, M. S. Scheurer, Y. Li, B. Yu, M. Greven, S. Sachdev, M. R. Norman, and D. Hsieh. Mirror symmetry breaking in a model insulating cuprate. *Nature Physics*, 17(7):777–781, 2021. doi: 10.1038/s41567-021-01210-6.

[168] Jens Sonntag, Sven Reichardt, Bernd Beschoten, and Christoph Stampfer. Electrical Control over Phonon Polarization in Strained Graphene. *Nano Letters*, 21(7):2898–2904, 2021. doi: 10.1021/acs.nanolett.0c05043.

[169] A. V. Anda, S. S. Makler, R. G. Barrera, and H. M. Pastawski. Electron - phonon effects on transport in mesoscopic heterostructures. *Brazilian journal of physics*, 24(1):330–336, 1994.

[170] Janez Bonca and S. A. Trugman. Effect of Inelastic Processes on Tunneling. *Physical Review Letters*, 75(13):2566–2569, 1995. doi: 10.1103/PhysRevLett.75.2566.

[171] Wang Yao, Shengyuan A. Yang, and Qian Niu. Edge States in Graphene: From Gapped Flat-Band to Gapless Chiral Modes. *Physical Review Letters*, 102(9):096801, 2009. doi: 10.1103/PhysRevLett.102.096801.

[172] M. O. Goerbig. Electronic properties of graphene in a strong magnetic field. *Reviews of Modern Physics*, 83(4):1193–1243, 2011. doi: 10.1103/RevModPhys.83.1193.

[173] Mark S. Rudner and Netanel H. Lindner. Band structure engineering and non-equilibrium dynamics in Floquet topological insulators. *Nature Reviews Physics*, 2(5):229–244, 2020. doi: 10.1038/s42254-020-0170-z.

[174] J. V. Pulé, A. Verbeure, and V. A. Zagrebnov. Peierls-Fröhlich instability and Kohn anomaly. *Journal of Statistical Physics*, 76(1):159–182, 1994. doi: 10.1007/BF02188659.

[175] A. Gambetta, C. Manzoni, E. Menna, M. Meneghetti, G. Cerullo, G. Lanzani, S. Tretiak, A. Piryatinski, A. Saxena, R. L. Martin, and A. R. Bishop. Real-time observation of nonlinear coherent phonon dynamics in single-walled carbon nanotubes. *Nature Physics*, 2(8):515–520, 2006. doi: 10.1038/nphys345.

[176] J.-H. Kim, A.R.T. Nugraha, L.G. Booshehri, E.H. Hároz, K. Sato, G.D. Sanders, K.-J. Yee, Y.-S. Lim, C.J. Stanton, R. Saito, and J. Kono. Coherent phonons in carbon nanotubes and graphene. *Chemical Physics*, 413:55–80, 2013. doi: 10.1016/j.chemphys.2012.09.017.

[177] N. Moreau, B. Brun, S. Somanchi, K. Watanabe, T. Taniguchi, C. Stampfer, and B. Hackens. Upstream modes and antidots poison graphene quantum Hall effect. *Nature Communications*, 12(1):4265, 2021. doi: 10.1038/s41467-021-24481-2.